Stony Brook University

Statistical Methods for Optimizing Task Performance in Nuclear Medicine Imaging and in X-ray Breast Imaging

A Dissertation Presented

by

Lin Chen

to

The Graduate School

in Partial Fulfillment of the

Requirements

for the Degree of

Doctor of Philosophy

in

Applied Mathematics and Statistics

Stony Brook University

May 2015

Stony Brook University

The Graduate School

Lin Chen

We, the dissertation committee for the above candidate for the

Doctor of Philosophy degree, hereby recommend

acceptance of this dissertation.

Dr. Gene Gindi – Dissertation Advisor
Associate Professor of Electrical and Computer Engineering and Radiology

Dr. Wei Zhu – Co-Advisor
Professor of Applied Mathematics and Statistics

Xiangmin Jiao - Chairperson of Defense
Associate Professor of Applied Mathematics and Statistics

Song Wu
Assistant Professor of Applied Mathematics and Statistics

Jerome Liang
Professor of Radiology and Computer Science

This dissertation is accepted by the Graduate School

Charles Taber
Dean of the Graduate School

Abstract of the Dissertation

Statistical Methods for Optimizing Task Performance in Nuclear Medicine Imaging and in X-ray Breast Imaging

by

Lin Chen

Doctor of Philosophy

in

Applied Mathematics and Statistics

Stony Brook University

2015

In many medical imaging systems used in radiology, the hardware delivers raw data to a sensor and a computer is used to convert the sensor data to a viewable image by implementing tomographic reconstruction algorithms. The radiologist views the image and performs a task, such as detecting a lesion. Engineers and applied mathematicians seek to improve medical imaging systems by making hardware changes and changes in the reconstruction algorithm. Improvement in this thesis is measured by scalar figures of merit, FOM, for task performance. We consider two modalities: SPECT (Single Photon Emission Computed Tomography) and Contrast-Enhanced DBT (Digital Breast Tomosynthesis). For SPECT, the tasks are detection of a signal and detection plus localization of a signal. We seek to improve the collimator (hardware) and regularizer of the reconstruction algorithm to improve SPECT task performance. We use the tools of statistical decision theory. The FOMs are area under the ROC curve for detection and area under the LROC curve for detection plus localization. We find that lower resolution collimators improve performance when coupled with an appropriate regularizer. For Contrast-Enhanced DBT, we alter the sequence of acquisitions by the X-ray tube by interleaving high and low energy acquisitions, and we alter the standard Filtered Backprojection (FBP) algorithm and use OS-SART (Ordered Subset Simultaneous Algebraic Reconstruction Technique). This

improves SDNR (Signal-Difference-to-Noise-Ratio), a FOM that is correlated with lesion detection performance. Key to the SPECT work is the use of mathematical observers, essentially feature extraction plus decision algorithms, that effectively emulate human performance in the detection and detection-localization tasks. Without these, the amount of labor involved in human observer studies is unrealistic.

Table of Contents

List of Figures

List of Tables

Acknowledgments

I would like to express my deep thanks to my dissertation advisor, Gene Gindi, for his guidance and encouragement over last 4 years. The dissertation truly would not have been possible without his effort. I would also thank my co-advisor, Wei Zhu, for her support from AMS department. Moreover, I would like to thank my committee members, Xiangmin Jiao, Song Wu and Jerome Liang. At last, I would thank our collaborator, Wei Zhao, for the support to the breast tomosynthesis project.

I would also thank to my colleagues of the Medical Imaging Processing Laboratory at Stony Brook University. I would thank to Lili Zhou for helping me a lot to get familiar with various software packages from the beginning when I just became a member of the lab. I would like to thank my lab-mate, Yihuan Lu, for helping me in many ways for this dissertation: especially building up the hardware and software for the GPU programming environment and for providing a lot of useful suggestions on model observers. For the breast tomosynthesis project, I would like to thank students of our collaborator, Dr. Zhao, who helped me. Yue-Hong Hu helped me to collect data from the Siemens prototype machine and explained a lot of details of breast imaging and the machine acquisition. David Scaduto helped in machine calibration and data acquisition. Also, I would like to thank Chintu Pandya for various hardware support effort in our lab.

Finally, I would like to thank my parents, Fukang Chen and Song Zhen for their support and encouragement in all my educational endeavors while I was pursuing my Ph.D. degree at Stony Brook University. Also, I would like to thank my friends, also undergraduate alumni, for making my daily life in Stony Brook interesting and enjoyable.

Chapter 1

Introduction

Medical imaging has undergone a revolution in recent decades with the introduction of tomographic imaging. Conventional imaging, as in a chest X-ray, typically gives a projection view, in which a 3D object like a chest is collapsed to into a 2D view. The thing being measured is the attenuation coefficient of the X-ray as a function of position. A 2D chest X-ray displays the line integral of attenuation coefficients, not the 3D map of coefficients. A line integral image is called projection image.

A breakthrough happened in 1960's with the introduction of tomography [1] in which 2D projection images taken at different angles could be mathematically combined into a 3D image. In subsequent years, this same tomographic principle was applied to nuclear medicine [2], in which the spatial distribution of a radiotracer in the body is mapped.

Engineers constantly try to improve tomographic imaging systems by improving the hardware (e.g. detector) or software (reconstruction algorithm). In this thesis, I try to improve two tomographic imaging modalities, SPECT (Single Photon Emission Computed Tomographic) and contrast enhanced digital breast tomosynthesis, an X-ray modality.

In SPECT, projection images of a radionuclide distribution in the body are combined to obtain a 3D map of the radioactivity. In contrast enhanced digital breast tomosynthesis, X-ray views of the breast are taken from several angles to get a 3D view of the breast.

For each modality, I propose a change in the hardware design or acquisition details that lead to a better image and propose better ways to do the tomographic reconstruction. "Better" must be measured in an objective way. For SPECT, I use performance on detection and detection and localization tasks as measured by ROC curves [3, 4] and use mathematical observers that emulate human behavior in detection performance. For breast imaging, I use a measure called Signal-Difference-to-Noise-Ratio.

The thesis is organized as follows: Chapter 2 gives an overview of mammography (breast imaging) and Chapter 3 gives a general background in the physics of X-ray imaging. Chapter 4

discusses digital breast tomosynthesis which is the application of tomography to mammography. Chapter 5 reviews tomographic reconstruction for digital breast tomosynthesis. In Chapter 6, I show my results in improving one form digital breast tomosynthesis called Contrast Enhanced Dual Energy Digital Breast Tomosynthesis. Thus Chapters 2-6 present the X-ray aspect of my work. In chapter 7, I give an introduction to another modality, emission imaging, involving the imaging of radioactive tracers. In chapter 8, I extend this material to SPECT, discussing image formation and reconstruction.

To evaluate task performance, we will use so called mathematical observers which are mathematical algorithms that implement decisions (e.g. is signal present or absent?) in a way that emulates human behavior in detecting signals in a noisy environment. In Chapter 9, we discuss the related task of detection and localization (detecting and finding the signal) and give mathematical, or "model" observers, along with Figures of Merit based on the Localization Receiver Operating Characteristic (LROC) curve.

The material in Chapters 7,8,9 come together in Chapter 10. Here, I use the tools developed in Chapters 7-9 to optimize both the collimator - an important piece of SPECT imaging hardware - and the regularization (smoothing) of the reconstruction in a way to optimize task performance.

In Chapter 11, we present a summary and discuss future work.

Chapter 2

Introduction to Mammography

Breast cancer is becoming a significant health concern in the United States. It is the most commonly diagnosed cancer in women, the second leading cause of cancer death in women and the leading cause of death in women ages 40-55 [5]. Almost one in eight women might develop a breast cancer during their life and about 20% of these women will die of the disease . Breast cancer diagnosis and cure can put a lot physical, emotional and financial impacts on patients, their families, and their friends. Screening breast cancer plays an important role in breast cancer detection in its early stage. Regular screening examinations can result in the detection and removal of precancerous growths, as well as the diagnosis of cancers at an early stage, when they are possibly curable.

Mammography has served as the pillar of breast cancer screening for about 3 decades and still the most effective method of detecting early stage breast cancer [6]. Clinically, screening mammography primarily helps radiologists, 1) to find suspicious lesions while they are still small; and 2) to localize suspicious lesions for a subsequent diagnosis. The American Cancer Society (ACS) recommends women of age 40 or older in the United States go for an annual screening mammography [7]. Many studies show that such wide application of the mammography has reduced mortality from breast cancer by approximately 24% [8]. If a suspicious cancer is found by pathology, or an area cannot be clearly seen, the woman will have additional views taken on the breast. This series of follow-up imaging modalities happens perhaps 10% of the time [5].

Traditionally, mammography is a 2D X-ray imaging system from a projection of 3D real breast to a 2D detector plane. The breast is stabilized with the proper compression and exposed to very low-energy X-rays, which pass throughout breast tissue onto the detector, while part of photons are absorbed to form a latent image. The breast compression means the breast is pulled away from the chest wall and squeezed a little between two plastic plates. Usually, two images are taken from different exposure directions: top-to-bottom/cranial-caudal (CC) view and side-to-side/mediolateral-oblique (MLO) view. Traditional mammography contains two modalities,

film-mammography and digital-mammography. Film-mammography can provide very good spatial resolution and contrast, thus is useful for identifying subtle differences among the various types of soft tissues in the breast. Film cassette storage is a problem, however, if the film is damaged or inadequate, such scanning must be repeated. Figure 2.1 (a) shows a film mammography taken from a CC view. In digital mammography (also known as Full-Field Digital Mammography), images are recorded on a high-resolution digital detector whose size is about the same as film-screen cassette**.** Figure 2.2 (b) shows a digital mammography taken at the same view as the film-screen mammogram. A digital breast image can be created when the X-rays pass through the breast, converted into a digital signals which will be saved easily on a computer and are not easily degraded. Also, Digital mammography can be processed and displayed on a soft copy or hard copy device.

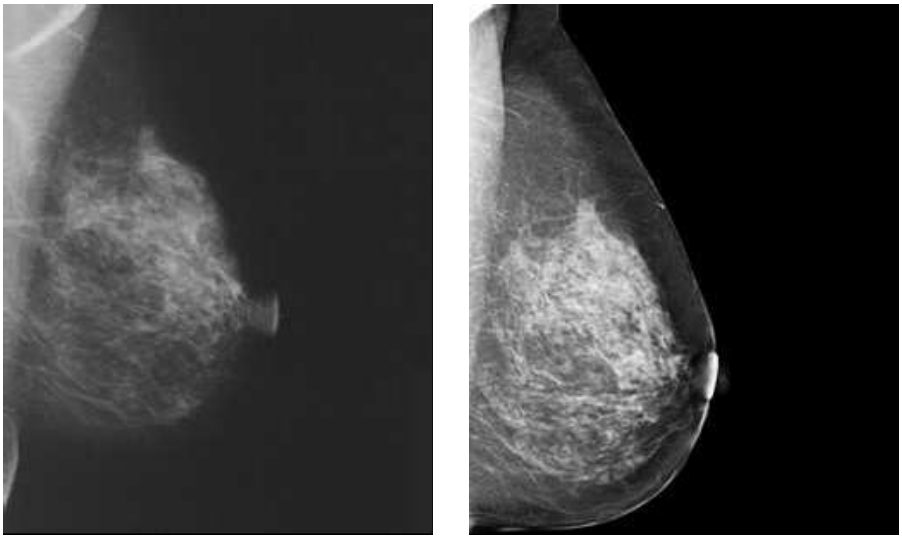

(a) Screen-film mammogram (b) Digital mammogram

Figure 2.1: Two conventional mammograms of the same breast at MLO view

One advantage of digital mammography is that the image, stored electronically, can be transmitted over long distances, allowing radiologists to consult their peers for opinions in geographically remote area. Another one is that digital mammography can be processed by Computer Aided Detection (CAD) systems to improve the sensitivity and reduce the variability from different readers in breast cancer detection. It is used after the radiologist has already made an initial assessment, thereby serving as a radiologist "re-review" of suspicious areas to reduce the risk of missing any abnormalities. Screening digital mammography, through early tumor

detection, has reduced breast cancer mortality rate by 20% in the last decades. Studies estimate that the sensitivity (true positive detection rate) of mammography is between 36% and 70% [6], depending on the density of a women's breast.

Mammographic characteristic features of breast cancer are masses, clusters of micro-calcifications, and architectural distortions of breast. More and more people have questioned the value of traditional mammography as a screening test because the 2D mammography involves a heavy superposition of breast tissues. In 2D mammography, the cancer lesions present in one plane of the 3-D breast are sometimes difficult to visualize since the contrasts between lesions, like masses, and their surrounding overlapped tissues are quite low. Thus, even with other sources of radiation or instrumentation noise, such superimposed normal breast tissues generate a "structural noise" that might obscure a suspicious tumor like a low contrast masses [9]. Studies show that 30% of breast cancer may be missed by conventional mammography. It is clear that mammography is less sensitive and results in less mortality reduction in younger women, usually with dense breast [10]. Furthermore, the overlapping tissues may look like a suspicious cancer on the mammogram and be mistaken for abnormalities, which will increase the probability for a false positive callbacks for further diagnosis. This requires additional imaging, radiation, exposure, expense and anxiety for patients without added health benefit. The National Cancer Institute reported that up to 12% normal breasts were mistakenly read for unnecessary diagnostic review.

There has been a development of screening and diagnostic strategies for breast specialists that allow us to find some of the smallest nonpalpable lesions deep in breast tissue, and have the potential ability to dramatically improve our ability to make an accurate diagnosis. These strategies can provide both preoperative counseling and planning, and effectively decrease the need for aggressive biopsies. Some of these strategies are updated versions of old standards, like Digital Breast Tomosynthesis (DBT) system and Contrast-Enhanced mammography. Although breast tomosynthesis is relatively new, the original theoretical concept of tomosynthesis was first introduced almost eight decades ago, and the term "*tomosynthesis"* was first used in a journal article almost 40 years ago [11].

DBT uses conventional X-rays and a digital detector, similar to the digital mammography, to create three-dimensional mammographic images that make it possible to search through the

interior of a breast in tomographic cross-sectional images with minimal overlapping tissues. Each slice of a DBT image are typically thin, around 1mm. This alleviates the confusing tissue superimposition and can enhance the conspicuity of breast lesions, reducing the chance of misdiagnosis of a tumor from groups of tissues. In contrast to digital mammography, the X-ray source of DBT is engineered to move in a limited arc range over the breast (10 degree-50 degree). Several 2D projection images (11-15) are obtained at different angles during the scan. In the next step of DBT, a reconstruction algorithm is applied on the set of projection data to produce a 3D image of the breast, which is ready for radiologists to review. Early clinical trials of DBT show the potential for both the improved cancer detection and the reduction in the need for additional diagnostic imaging for women who are subsequently found to be cancer free [12]. Figure 2.2(b) shows a tomosynthesis slice where we can see a cancer. However, comparing with Figure 2.2(a), it is hard for us to see the tumor in digital mammogram, where the cancer is hidden in the overlapping tissues. Also, DBT has been shown to contribute to a 30% reduction in recall rate when combined with digital mammography [13]. The specification of many parameters of a DBT system are still under research investigation, including the exact number of projections, the angle range, algorithms and so on. The efficacy of DBT needs further study from clinical trials. Recently, the US Food and Drug Administration (FDA) approved the first commercially available DBT system, Dimensions 3D, from the Hologic company, for cancer screening and diagnosis. This delivers a promising future for the 3D breast imaging technology.

Contrast-enhanced (CE) mammography involves injecting an iodine contrast agent intravenously to a patient while the breast is imaged with a sequence of digital mammograms that show the distribution of contrast iodine over time. These images are evaluated in two ways, 1) to look for the image where the iodine concentration peaks, 2) to analyze the flow of iodine into and out of a tissue area. Clinical studies have shown that region having high uptake of contrast agent means more possibility of malignant tissues, which often exhibit a rapid wash-in and wash-out of iodine, while benign tissues will have a slow uptake of iodine. CE mammography is of more interest in diagnosis of cancers clinically rather than screening because of its a invasive injection into the human body. Although CE mammography can improve the detection of breast cancer, it is still a 2D breast image modality and the overlapping tissue limitation is still unsolved [14]. Combining the CE mammography and tomosynthesis can

provide a potentially powerful new modality of breast cancer identifying and improve people's quality of life.

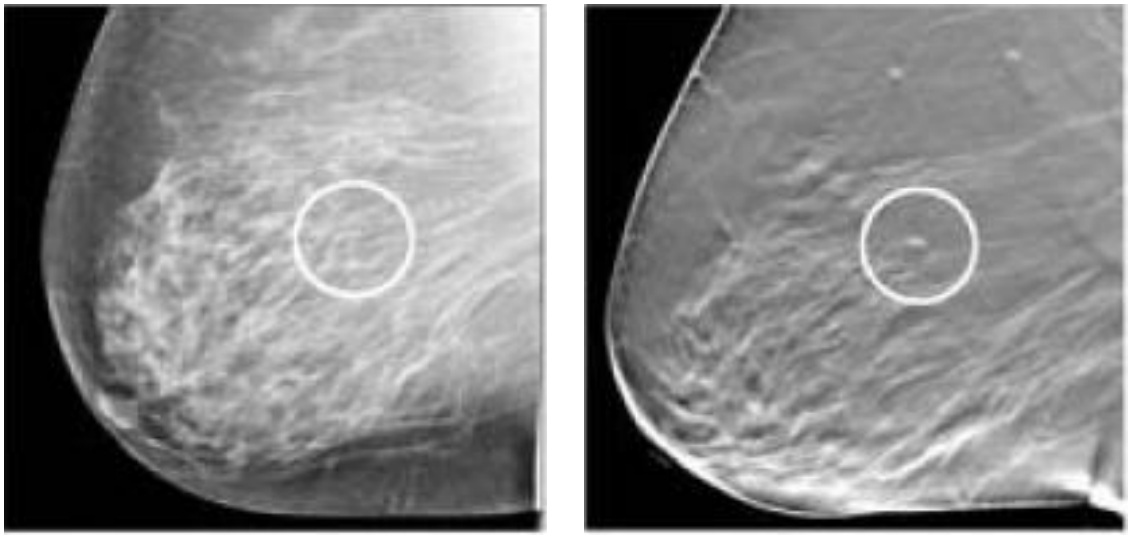

(a) Digital mammography (b) Digital tomosynthesis slice

Figure 2.2: (a) Mammography with an invisible lesion. (b) Tomosynthesis slice that shows improved lesion visibility. The circles indicate the lesion area from the same breast.

In this thesis, we investigate different possible protocols for CE-DBT. Detection of masses in breast imaging is unique in radiography due to the small amount of subject contrast in the surrounding tissues. In mammography, contrast between the mass and the background structure is fairly small because of the tissue-overlapping, which presents a big challenge in lesion detection. Even in DBT image, sometimes the mass is still difficult to see. In our study, a physical anthropomorphic phantom (CIRS) was applied to mimic the real compressed women's breast structure and shape. Sets of raw projection data are collected from the Simens Inspiration prototype DBT unit. Several tomosynthetic methods are used to reconstruct 3D breast estimates.

One limitation of our work is that we do not consider micro-calcifications, a small size (0.1mm-1mm) and high contrast calcium deposit associated with breast cancer. They can be any tiny spot or a cluster of several spots. Three dimensional DBT image may help in viewing such clusters [15, 16], but ordinary mammography may be better for viewing calcification clusters. Also, there are other medical image modalities that can present 3-D breast images, like breast computed tomography (BCT), breast magnetic resonance imaging (MRI) and breast ultrasound.

Discussion of these modalities is beyond the scope of this thesis. But, DBT system has its own advantages, and is fast and cheap compared to other systems.

The dissertation involves two modalities mammography and SPECT. For the mammography research, the dissertation is organized as follows. Chapter 3 provides an overview of background information including X-ray medical imaging physics, breast anatomy, and conventional mammography. It is useful to review the practice of mammography, because it offers clues as to where tomosynthesis can improve. Chapter 4 addresses details of the digital breast tomosynthesis system and lists some important factors that may affect 3D breast image quality. The possible combination of CE mammography and DBT are discussed. In chapter 5, I shall review various reconstruction methods used in transmission tomography. In chapter 5, I introduce a mathematical model for transmission image formation, which is a basic for image data processing. In chapter 6, we show how the projection data is acquired for CE-DBT method and discuss different data processing used in our project followed by the discussion of our experimental results.

Chapter 3

Background for Medical Physics for X-ray Imaging

Here, we give a basic background introduction to the medical physics of X-ray imaging. The whole process of X-ray production, interaction and detection that can be described as an imaging chain

3.1 Basic physics of x rays

X-rays were discovered in 1895 by Wilhelm Conrad Roentgen (1845-1923) who was a Professor in Germany. In his laboratory, working with the most primitive cathode-ray tube, Roentgen observed a new type of rays emitted from the tube, which was later named as X-rays. X-rays are one waveform of the electromagnetic spectrum [17], like light rays or microwaves as Figure 3.1 shows. The wavelength of the X-ray ranges from a few pico-meter to a few

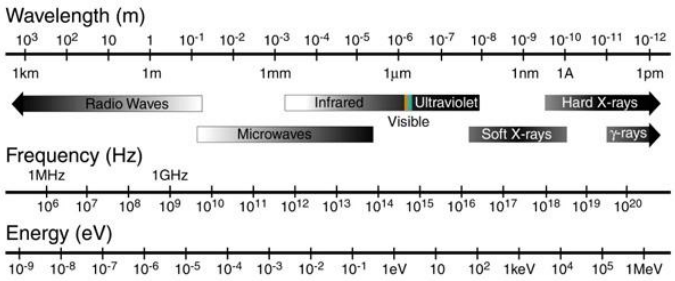

Figure 3.1: Illustration of the electromagnetic spectrum.

nanometers. Although X-rays can be characterized by wavelength, they act like particles at energies used in medicine and are referred to as "photons", a massless particle, travelling at the speed of light. The energy of each X-ray photon is proportional to its frequency [18], υ, and is described by the following expression:

$$E = h\upsilon = \frac{hc}{\lambda} \tag{3.1}$$

where h is Planck's constant and equals to 6.63×10^{-34} j s, c is the speed of light (3×10^{8} m/s), and λ is the wavelength of the X-ray photon. For convenience, the X-ray energy is usually expressed in units of eV ($1eV=1.602\times10^{-19}$ j). They possess no charge, therefore, are not influenced by electrical and magnetic fields and will generally travel straight lines except for scatter [19].

3.1.1 X-ray production

The most common X-ray production technology used in medical imaging is the standard X-ray tube, where a substance is bombarded by high speed electrons [20]. Usually the substance is a material with high atomic number, like tungsten (Z=74). A glass envelop seals the vacuum environment inside the tube. The vacuum will increase the efficiency of X-ray production, otherwise, energetic photons would collide with air molecules instead of the target substance [21]. As Figure 3.2 shows, there is a circuit with high voltage in the tube. The applied potential is expressed in units kV (kilovolts). The peak kilo-voltage, kVp, is the maximum kV potential value applied across the X-ray during the exposure. The power supply has a ripple, so kVp is used to indicate the max voltage. The anode, usually a disk, is the positively-charged pole of the circuit, and is also the target of the bombarding electrons [22]. The cathode is

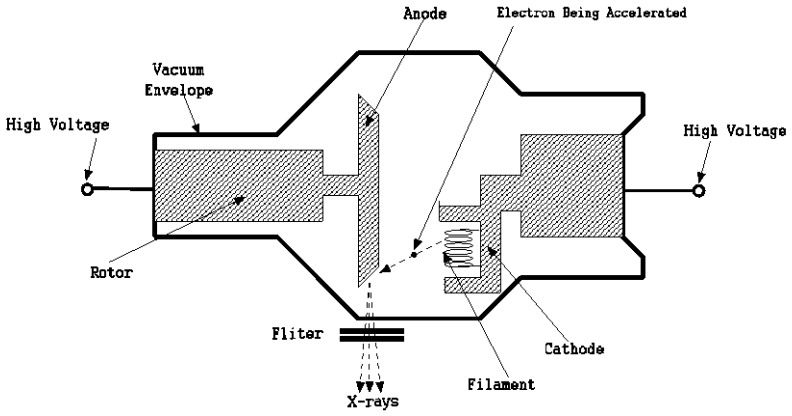

Figure 3.2: The illustration of X-ray tube.

the negative voltage pole of the circuit, and is the source of electrons that bombard the anode target. During the X-ray exposure, the cathode filament will be heated up by passing the filament current through it. When the filament of the cathode is hot enough, some electrons can become free electrons when they obtain the enough thermal energy to overcome the binding energy. As electrons boil off of the filament from the cathode, the high voltage between the anode and

cathode will accelerate electrons towards the target material, making a weak current. The flow of current from the cathode to the anode inside the X-ray tube is the X-ray tube current, which is different (much lower) than the filament current. It is an important parameter to decide the level of X-ray radiation dose and the unit is usually mAs (milli amps times second) [23]. After being accelerated into the anode, only a small fraction of electrons is converted to emit X-rays, and most of the electron energy is converted into heating the anode [24].

It is ideal to design a small focal spot for the bombarding electrons on the anode so that X-rays can be thought of as emitted from a point source because any increase in source size will result in blurring of the image [21]. However, there is a physical limit to the size of such a focal spot since the anode material might melt if too much heat is deposited into this small area. This limit is improved by the use of line focus principle as shown in Figure 3.3. Incorporating a small anode beveled angle (7^o-15^o) allows the use of a large actual focal spot, allowing the heat dissipation over a larger surface, while the dimension of the actual focal spot for emitting X-rays is still small [25]. The X-rays are viewed from a shallow angle almost parallel to the bevel. In this way, the object sees the anode "stripe" at a large obliquity, and the stripe has the effective shape and area of a small spot. To improve heat dissipation further, the anode disk is rotated so that the actual focal spot can be kept refreshed with cooler area. In this way, the actual focal spot is an annulus, focal track, along the anode. The heat can be dissipated over a larger surface in that focal track as figure 3.3 (b) shows. The effective focal spot size for X-ray tubes used in mammography is 0.15mm to 0.45mm [26].

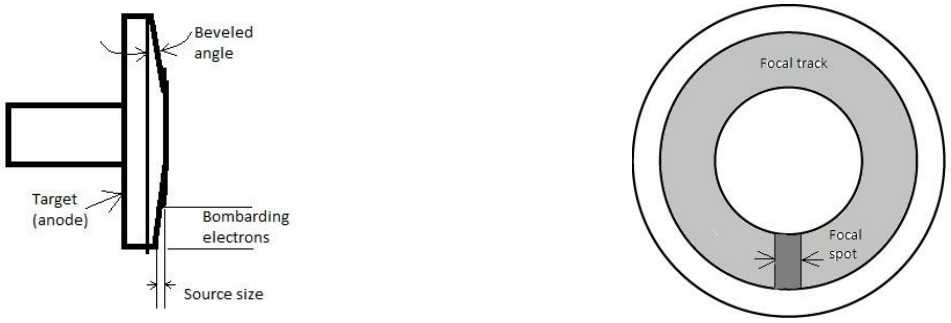

(a) Side view of the anode. (b) A front view of the anode.

Figure 3.3: The illustration of the heat dissipation in Anode.

The emitted X-ray beam from the tube is characterized by its energy spectrum. During the interaction between accelerated electrons and target, there are two kinds of X-rays contributing

to the X-ray spectrum, bremsstrahlung radiation and characteristic X-rays [20]. Bremsstrahlung radiation, braking radiation in German, is produced by such process that energetic electrons interact with the coulomb field of the nucleus of the target material atoms, which will decelerate the bombarding electrons. According to the classical electrodynamics [27], the deceleration of high speed electrons upon bombarding the anode results in emission of broad and continuous electromagnetic radiation, the bremsstrahlung radiation, as Figure 3.4 shows. Sometimes, an energetic electron collides directly with a nucleus and its entire energy appears as bremsstrahlung radiation, which represents the upper energy limit of X-ray energy spectrum. So, the bremsstrahlung spectrum of energies is produced with a range from a few keV to a maximum of the energy of the electron beam, which depends on the applied potential between the anode and cathode.

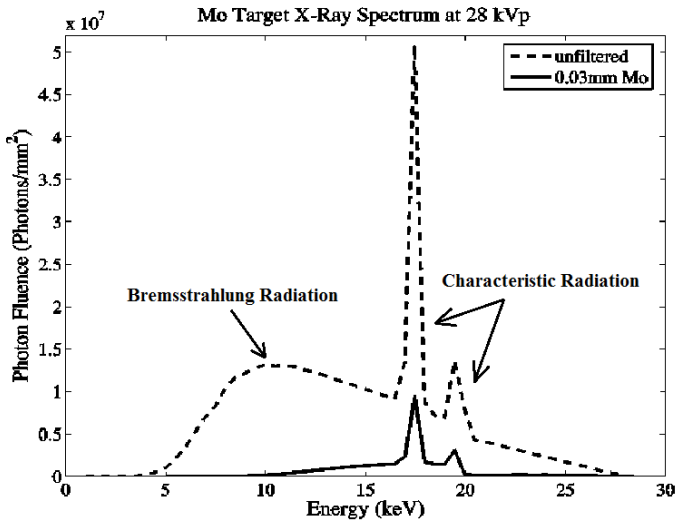

Figure 3.4: Energy spectrum of the X-rays emitted from a diagnostic mammography X-ray tube at 28 keV. The anode is molybdenum. The peaks are due to the characteristic radiation and the background is due to bremsstrahlung radiation. Adding 25 μm of a rhodium filter reduces much of the low-energy component of the X-ray spectrum, but also significantly attenuates X-rays in the unfiltered spectrum above 20 keV.

Another component of X-ray spectrum, characteristic radiation, occurs when these energetic electrons interact with the atomic electrons in the target material. In the atom, atomic electrons are bounded in obits with specific quantized energy levels (binding energy) [28]. Different orbits, or called atomic shells, have different binding energies by charge-charge interactions. The inner shell will have greater binding energy than the outer shell for atomic electrons. The production of characteristic X-rays begins when the accelerated electrons interact with the atomic electrons of

inner shell in the anode target, giving the atomic electron enough energy to knock it out of the binding state to free it to leave a vacancy in that shell. This vacancy will be filled quickly by an electron from a outer shell, which will be filled by another atomic electron from a more distant outer shell. Thus, this ejection and fill sets up a whole cascade of electron transitions, until the vacancy of the most outer shell is filled by free electrons in the environment [21]. Each transition of atomic photons will emit the X-ray at a discrete energy level, which is equal to the difference between two binding energies. Since each element in the elemental periodic tables has its own unique atomic shell binding energy levels, the characteristic X-rays are unique to each material. For example, the characteristic X-ray energies of molybdenum, which is one of the most common anode materials in mammography X-ray tube, are mostly at 17.9 keV and 19.5 keV. So, the composition of X-ray tube determines the X-ray spectrum. Two peaks in Figure 3.4 are due to the characteristic radiation.

The X-ray spectrum generated in the tube needs be further refined by using filters which allow X-ray photons with a specific energy range to pass though [29]. Usually, a directly generated X-ray spectrum cannot be applied to a patient because low energy X-ray photons is easily absorbed, which may cause potential damages to human bodies. Another important reason is that a proper spectrum energy range can make a X-ray image with a good image contrast [30]. High energy X-rays can penetrate human tissues and the low energy part is mostly absorbed. The filter is made of sheets of metal, attached to the tube but not in the vacuum tube. If the appropriate filter is chosen, the X-ray spectrum can be narrowed down to pretty small range to take advantage of better contrast from the low energy photons and reduce the unnecessary absorption for humans [31]. The filter material can be the same as the anode material or varied to match the anode material for different imaging purposes. Usually, the X-ray energy spectrum for mammography is between 10 to 30 keV [32]. The composition spectrum obtained from a typical mammography X-ray tube is shown in Figure 3.4. This spectrum is produced at 28 kVp with and without filtration. As one can see, the molybdenum anode spectrum is composed of bremsstrahlung and characteristic radiation. The filtered spectrum, using a 25 μm rhodium (Rh) filter at 28 kVp, shows a distribution with no X-rays below about 5 keV, and a dramatic decrease of X-rays at below 17 keV and 20 keV. The filtration eliminates the majority of low-and high-energy X-rays, as shows in Figure 3.4.

3.1.2 X-ray Interaction with Matter

The next step along the imaging chain is the X-ray interaction with matter (i.e. the breast tissue in mammography). When the X-ray beams pass through a matter, they will get attenuated and thus X-ray photons are removed from the incident beam. Within the X-ray energy spectrum for breast X-ray imaging, this attenuation takes place by two main processes: photoelectric absorption and Compton scatter [33].

The photoelectric absorption involves the interaction of the incident X-ray with an inner shell electron in the absorbing atom that has a binding energy close to but lower than the energy of the incident X-rays [25]. In this process, X-ray exhibits discrete particle characteristics by quantum mechanics theory, although they can exhibit wave properties like other electromagnetic waves. The incident X-ray photon imparts all of its energy to the bound electron with the ejection of that electron leaving a vacancy in that shell. Some of the photon energy is used to overcome the binding energy of the inner shell and the rest appears as the kinetic energy of the ejected electron. The vacated electron shell is filled by an electron from an outer shell, producing a characteristic X-ray of human body tissues. Atoms in human body contain mostly low atomic number (e.g. hydrogen, Z=1; carbon, Z=6; nitrogen, Z=7; and oxygen Z=8;), which means low binding energy characteristic X-rays will be emitted, less than 4keV, and absorbed again by human tissues locally. Thus, for photoelectric absorption in human tissues, the energy of the incident photon is locally deposited.

On the other hand, the Compton scatter is an inelastic interaction of an X-ray photon with either a free electron or, loosely bound in one of outer shells, where the binding energy is much lower than the incident X-ray photons energy [25]. Partial energy transferred to the electron causes a recoil and removal from the atom at an angle. The remainder of the energy is transferred to a scattered X-ray photon with a trajectory of angle relative to the trajectory of incident photon. As a result, the X-ray photon is deflected onto a new path from its original direction with some loss of energy.

These two interaction mechanisms discussed above mainly contribute to attenuate the incident X-ray photons as it passes through human tissues [33]. Attenuation is the removal of X-ray photons from the X-ray beam by either absorption or scattering events. For a monoenergetic

X-ray beam with N_0 photons passing through a thin slab with uniform material with thickness *dl* along the incident X-rays direction, the probability of attenuation, μ, is a constant (see in Figure 3.5(a)). Denote the fractional reduction of the number of photons from incident beams by *dn* , which is given by,

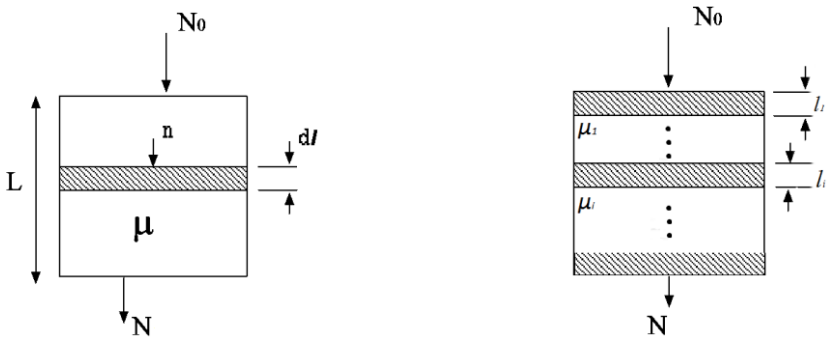

(a) Single composition (b) Compound material

Figure 3.5: An X-ray beam with *N0* photons passes through an object.

$$dn = \mu n\, dl\,. \tag{3.2}$$

Here, *N* is the number of photons emerging from the material. Rearranging and taking the integral on both sides, we can get,

$$-\int_{N_0}^{N} \frac{dn}{n} = \int_{0}^{L} \mu dl \tag{3.3}$$

where we put minus sign on the left side to say that *dn* is a decrease during the attenuation. Since μ is constant in this case, it can be taken outside the right side integral of Equation (3.2). Solving Equation (3.2) gives the Lambert-Beers Law [34]:

$$N = N_0 e^{-\mu L} \tag{3.4}$$

The entity μ is called the linear attenuation coefficient and its unit is *cm*-1 , which means the value of μ gives the probability that an X-ray photon will be attenuated per centimeter within the object through absorption and scattering. The attenuation process for materials comprised of ≥2 elements as in Figure 3.5(b) can be determined as the weighted average (by the fractional thickness for different composition) on the exponential part as shown in Equation (3.3),

$$N = N_0 e^{-\sum_i \mu_i l_i} \tag{3.5}$$

where μ_i is the attenuation for *ith* element in the compound and l_i denotes the thickness of the *ith* element along the incident direction. In the general situation, attenuation coefficient depends on both incident X-ray photons energy ε and attenuation position of the object **r** in the continuum with complicated composition materials, like breast. The attenuation μ should be expressed as $\mu(\mathbf{r}, \varepsilon)$ and the summation becomes an integral. In the X-ray energy range for medical images, the linear attenuation coefficient varies with the X-ray energy. In chapter 5, we will generalize the simple Beer's law of Equation (3.5). A 2D mammogram is due to line integrals of μ through the breast as we shall see later.

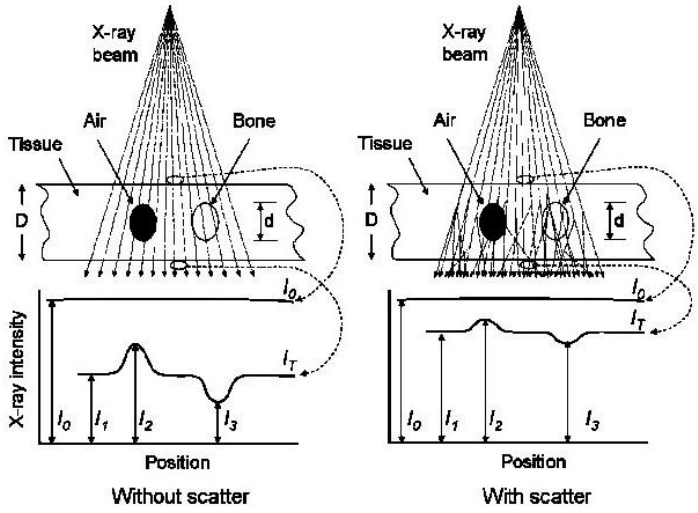

Figure 3.6: Ideal projection radiograph contrast with and without scatter. If the source is far from the object, then *I0* is a uniform incident fluence and *I1*, *I2* and *I3* are fluences through tissue, air and bone, respectively. The subject contrast is the difference in signals due to object and due to the background. On the right is typical situation in the presence of scatter, demonstrating a loss of subject contrast and smaller difference between incident and transmitted radiation intensity relative to the no-scatter case on the left.

With the background discussed above, we can talk a little about how scatter affects image contrast. X-ray image contrast is the spatial variation in the X-ray beam after passing through the patients. The variation is due to the different X-ray attenuation within the patient's tissue, decided by the density, different tissue, and thickness properties [35]. Figure 3.6 gives a simple example. The transmitted photons without deflection, are usually called primary radiation photons. Ideally, only primary radiation photons contribute to the formation of the image, and

the maximum subject contrast is achieved. The deflected X-ray photons from Compton interaction can also pass through the object. X-ray scatter reduces subject contrast by adding background signals that are not representative of the anatomy as seen in Figure 3.6. An important measurement is the scatter-to-primary ratio, S/P, indicating the scattered X-ray fluence to the primary X-ray fluence incident on the detector. Typical S/P ratios encountered in radiograph depend on the thickness of the object [36]. We will talk more about scatter in chapter 4.

After the X-ray beam passes through the object, the transmitted X-ray photons with object contrast is recorded on the detector with conversion into a visible 2-dimensional image. X-ray detectors can be classified as direct or indirect [37]. The direct detection system transfers X-rays directly to electrical charge without intermediate states from ionization of the detector materials atoms. Amorphous selenium (a-Se) has been usually used as the direct X-ray detector material [34]. The indirect detection system transfers X-rays to visible light photons and then finally to electrical charge. A scintillator-based X-ray detector is used in an indirect detection system. In the indirect detection mechanism, X-rays interact with a phosphor, causing it to emit light photons. These light photons then propagate by optical diffusion to a photo-detector, such as film emulsion or silicon photo-diode. The photo-detector then records the pattern of visible light discharged by the phosphor as an image. Both direct and indirect detection process can be described by a cascaded linear model with the assumption of a stationary system [12]. More details are given in section 4.2.

3.2 Basic breast anatomy: Normal and Abnormal

The breast is inherently a low-contrast organ and highly variable in density and size, and presents tremendous challenges for breast imaging. A basic understanding of breast anatomy can help understand the composition of breast radiography in gray scale. Also, many researchers, including us, apply a physical anthropomorphic phantom to replace the real breast in various prototype imaging studies. Otherwise, it is unethical to directly use women for breast cancer studies. With the background knowledge of breast tissues, we can understand to what degree the anthropomorphic phantoms emulate real breasts can reach.

3.2.1 Breast normal composition

The breast is attached to the chest wall. The skin of breast is usually 0.5 to 2 mm in thickness [38]. The fascia layers lie beneath the skin. Blood vessels and lymphatic vessels penetrate the facial layers, running through the muscle and the other breast tissue. The pectoralis muscle spreads like a fan across the chest wall and permits breast traction when the breast is positioned and compressed.

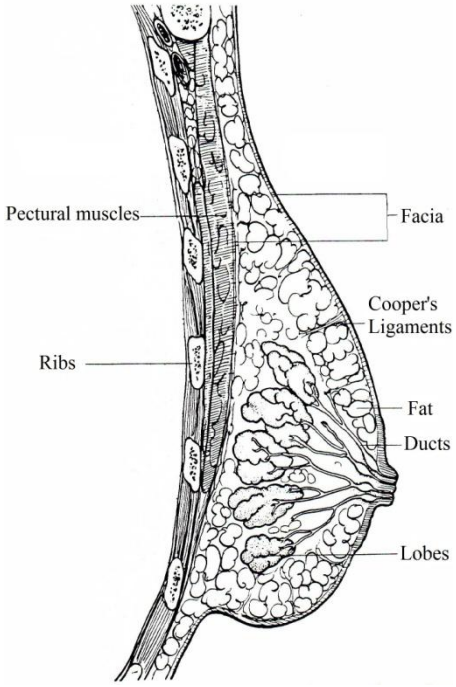

Figure 3.7: The basic structure of a breast. A sagittal section is shown

In general, the breast is a grouping of glandular, fatty and fibrous connective tissues positioned over the pectoral muscles of the chest wall and attached to the chest wall by fibrous tissue called Cooper's ligaments as Figure 3.7 shows. A layer of fatty tissue surrounding the breast glands and extends to throughout the breast. The fibrous connective tissues of the breast house the lobules (milk producing) and the ducts (milk passages). There are 8-20 major ducts that originate from the nipple. Each one dilates into narrower and shorter branches until form the terminal duct and its lobule called the terminal duct lobule unit, leading to a tree-like structure. The ductal structure is an important component of the breast anatomy since practically most breast cancers originate in the ductal or lobular epithelium, with very few arising in the connective or adipose tissue [39]. Breast ducts also contribute significantly to the parenchymal

pattern, the background texture (anatomical variability). Most attenuated X-ray radiation is absorbed by these two types of tissues, contributing to the breast image background contrast. Adipose (fatty) and glandular tissues are the two predominant tissue types in the breast that might mask the tumor masses in X-ray image.

3.2.2 Breast abnormalities

Breast abnormalities can be divided into major types: tumor masses and micro calcifications [40]. Microcalcifications are mineral deposits (calcium) with high attenuation (relative to normal tissue), while tumor masses are groups of abnormal cells with low-contrast X-ray transmission attenuation (similar attenuation coefficient as that of normal tissues). Both types can be differentiated as being malignant or benign. Micro calcifications can be present as either a tiny single spot or a cluster. Usually, they have small size with diameter range 0.1mm-1mm [38]. Scattered spotty micro calcifications are often a sign of benign breast tissue. Five or more calcifications, each with a diameter $\leq$ 0.5mm, isolated in a cubic centimeter volume, have a high probability of malignancy. Furthermore, malignant calcifications are more irregular in shape, size and distribution [41].

Tumor masses are of more interest to us. They vary in shape, size and density. The study by Kopans [38] suggested that $\geq$50% benign tumor masses are $\leq$ 1cm in diameter. The American college of Radiology (ACR) classifies the masses shapes are round, oval, lobulated , irregular as shown in Figure 3.8. A mass can have one of five types of margins (small-scale boundary structure): circumscribed, micro lobulated, obscured, ill-defined and spiculated, as illustrated in figure 3.7(a). The more irregular in shape, the more possible in malignancy. The probability of malignancy is high in lesions with ill-defined margins [41]. So, a lesion that is round, oval, lobulated with sharply defined borders has a very high likelihood of being benign.

It is now evident that tumors have a very limited capacity to grow without extra vascular support, which means they require an adequate supply of oxygen and nutrients and an effective means to dispose its waste product for survival and growth. Angiogenesis refers to extra blood vessel formation to sustain such metabolic process and can be one of the hallmarks of cancer. The development of new blood vessels in a cancer setting (angiogenesis) is conducted by

numerous physiological and pathological stimuli, where the main stimulus is hypoxia [42]. Malignant breast tumor angiogenesis factors stimulate formation of disorganized vessel networks with abnormally increased vessel permeability. As a result, the absorption of vascular contrast agents (iodine in X-ray image) in malignant breast is often different to that in benign and normal tissue. The different permeability can provide can help diagnose malignant masses. Clinical diagnosis with application of angiogenesis relies on the analysis of morphological features (margin information of tumors) and vascular enhancement patterns; however no consensus exists to which feature is more informative.

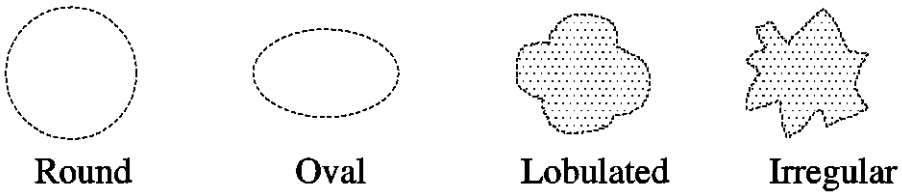

Figure 3.7: (a) Possible mass shapes.

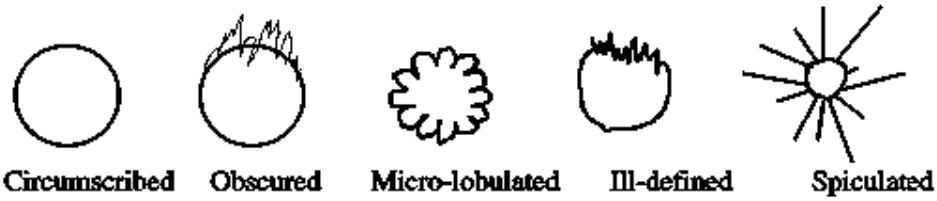

Figure 3.8: (b) A mass can have one of five margin types.

3.3 Conventional mammography

Here, we introduce conventional mammography. It is worth describing conventional mammography since it is a wide-spread modality for screening breast images. Moreover, breast tomosynthetic units are hardware modifications of conventional mammographic units and not quite mature. They are modifications of conventional mammography image systems.

The common mammography unit is composed of an X-ray tube and an image recorder mounted on the opposite sides of a gantry (see Figure 3.9 (a)). The system geometry is unusual since only on half of the field of the X-ray tube is used as illustrated in Figure 3.9 (b). A compression paddle is attached to the mammography unit in order to compress and hold the

breast. The compression level is usually measured as force put on the paddle in units of Newton's. The average thickness of compressed breast is approximately 5 cm. Breast compression is an important step during mammography. It can lessen overlapping normal shadows by flattening the

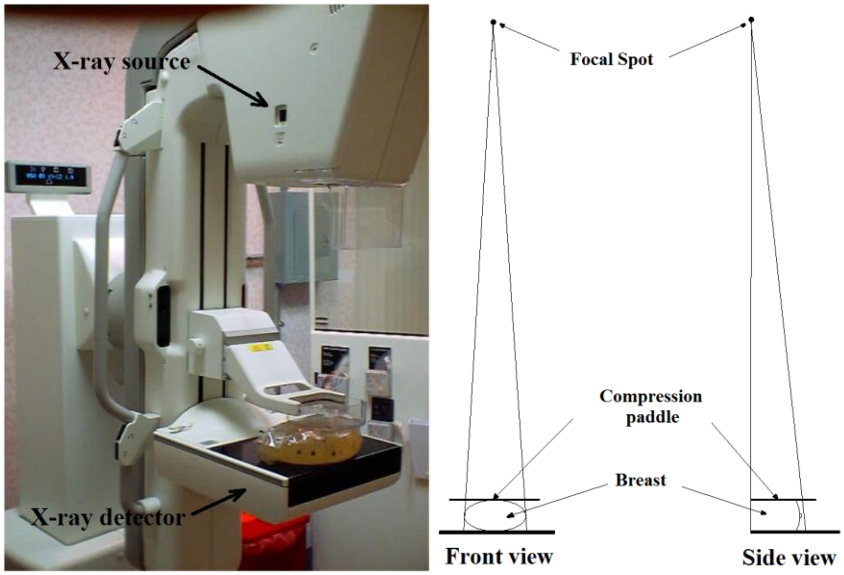

(a) (b)

Figure 3.9: (a) GE digital mammography equipment. The X-ray tube is housed in the box at the top. A phantom sits atop the detector (dark panel at bottom). (b) Geometric arrangement of system in mammography. The geometry is not in relative scale but we can have a sense that the source is far away from the breast so that incident rays can be seemed as an approximated uniform fluences.

breast for better visualization of anatomy and potential abnormalities. The compression allows the use of a lower X-ray dose since a thinner amount of breast is being imaged. Also, thinner breast will reduce X-ray scatter that improve the image contrast. Furthermore, the image blurring caused by patient motion can be reduced by immobilization of breast from compression. Typically, two views of images are taken from each breast in conventional mammography [43]. As Figure 3.10 shows, two images are taken from over the breast (from top to bottom), called cranial-caudal (CC) view and form an oblique or angled direction, called mediolateral-oblique (MLO) view as illustrated in Figure 2.1. These images are recorded on a detector, which represents the summation of breast tissue attenuation along the transmission path. Two types of mammography are classified based on different detectors.

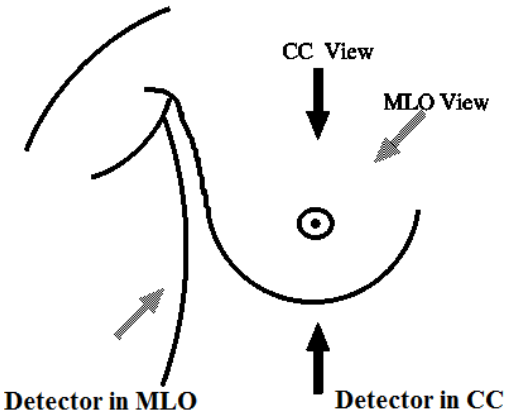

Figure 3.10: Solid arrows indicate the positioning of CC view. Dotted arrow indicate MLO view. The X-ray tube is positioned above the breast.

3.3.1 Screen-film mammography

In screen-film mammography, transmitted X-rays are recorded on a screen film cassette under the breast after X-rays from a point source penetrate the breast. As these X-rays pass through the breast, they are attenuated to varying degrees by different tissues. The result appears as the gray-scale regions, such as glandular tissue, tumor masses and micro-calcifications appear as varied levels of white regions on screen-film mammogram due to different attenuations at different tissue structures as Figure 3.10(a) shows. Film-screen mammography has following advantages [44]: (1) The technology is relatively inexpensive and well established. (2) The image receptor is capable of achieving very high limiting spatial resolution (at least 20 lines-pairs/mm).

However, screen-film mammography has some limitations on displaying the finest features due to inadequate contrast leaving a limited sensitivity for the detection of breast cancer with dense breast [6]. Film does not have a linear sensitivity to photon flux and there is a narrow range over which it can detect small difference in contrast [45]. Also, the processing time and storage space is worse for film than for digital images. Another limitation is that the structural noise due to film granularity degrades the visibility of micro-calcifications and other fine breast structures [46]. Moreover, the film-screen systems are not applicable for tomosynthesis which requires several images acquired and read out in digital form for further data processing. This limitation can be effectively overcome with digital mammography.

3.3.2 Digital mammography

A Digital mammography, sometimes called full-field digital mammography (FFDM), system is similar to screen-film mammography. The digital detector and a computer equipment are included in the digital mammography system. The digital detector can convert X-ray photons to digital signals and save them on the computer instead of the film cassette. These signals or images can be processed and displayed on a soft copy or hard copy device [47]. It is easy to apply the contrast enhanced method in the digital mammography system, which need a further data processing after X-ray scan.

Digital mammography is established in clinical practice, but still has some space to improve. Some research studies [6] suggested that the overall diagnostic accuracy of digital and film mammography for breast cancer was similar, but digital mammography is more accurate in women with dense breasts. The improved performance in the digital mammography is mainly associated with the X-ray detector and the display device. The digital mammography system can provide high resolution display monitors and hardcopy devices. Current large-area flat-panel detectors can accommodate small and average-size breasts with an $18cm \times 24cm$ detector for larger breasts, and achieve a spatial resolution of $50\ \mu m$ per pixel [48]. While digital mammography may lack the spatial resolution of film, it can provide improved contrast resolution if using tomosynthesis, which can improve the abnormalities contrast. Digital breast tomosynthesis can inherit most advantages of digital mammography and provide further benefits.

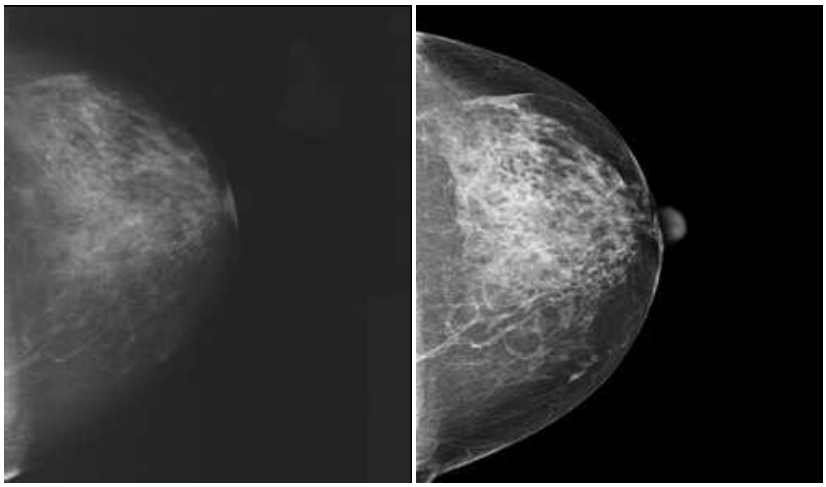

(a) Screen-film mammogram (b) Digital mammogram

Figure 3.11: Conventional mammograms of the same breast at CC view.

Chapter 4

Digital Breast Tomosynthesis (DBT): 3D Breast Imaging

Breast tomosynthesis is a 3D X-ray breast imaging modality. The hardware can be easily adapted from conventional mammography as shown in Figure 2.8(a). We go through the entire imaging system and address problems in each stage. These problems have been attacked piecemeal i.e. many separate studies have been done to investigate one or two factors in the system, and the whole problem is too large to be addressed in this thesis. We shall start with the introduction of the reconstruction stage, discuss about the digital breast tomosynthesis system and a new modality based on DBT systems, contrast-enhanced digital breast tomosynthesis. Here, we mainly focus on the mass detection in DBT systems and do not consider detection of calcifications.

4.1 Reconstruction

Reconstruction in the breast tomosynthesis procedure is the final step and an important one. The purpose of this step is to estimate the spatial distribution of attenuation coefficient of breast tissues, which we call the object, from a set of projection data [49]. These projection data are a measurements from pixels in the detector. Each measurement is proportional to the Lambert-Beer Law of Equation (3.5), whose exponential component is equal to the summation of the attenuation coefficients or line integral parts. The estimated object (3D reconstruction image) is represented as a discrete image array in gray scale, composed of voxels for a 3D object. The 3D object should give a set of 2D projection images each of which is like mammography. These 2D projection images follow Beer's law in Equation (3.5). In X-ray imaging reconstruction, we usually take the logarithmic transform on projection data before we apply the reconstruction algorithm. The logarithmic transform is done by dividing both sides of Equation (3.5) by N_0 and taking the negative logarithm of the resulting quantity. We obtain

$$g = -\ln\left(\frac{N}{N_0}\right) = \sum_i \mu_i l_i \tag{4.1}$$

where g is the projection data after the log step. Equation (4.1) applies to a single ray passing through several layers l_i and attenuation μ_i. When the object is continuum, the summation in Equation (4.1) becomes an integral,

$$g = -\ln\left(\frac{N}{N_0}\right) = \int \mu(l)dl \tag{4.2}$$

Equation (4.2) applies to a single ray passing through an object where the attenuation varies continuously with space. Now, the reconstruction problem becomes: Given the measured line integrals of an object, we need to estimate the attenuation distribution. This definition of the reconstruction problem is restated more precisely in Chapter 5.

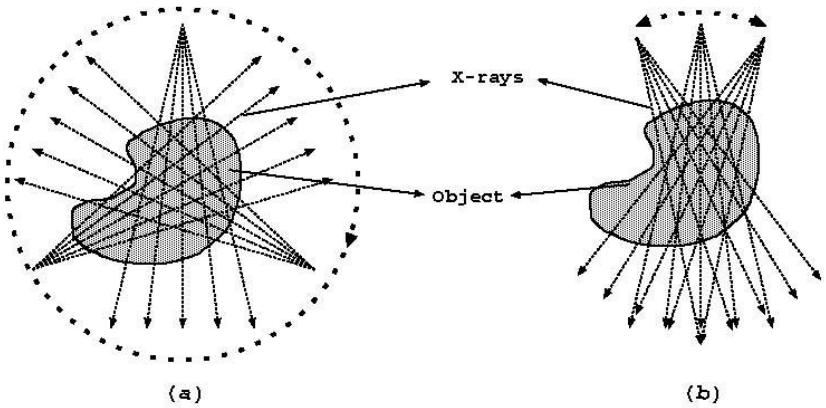

Figure 4.1: (a) A general CT geometry. (b) Tomosynthesis geometry. In both geometries, the dotted line denotes the trajectory in which the tube moves around the object. The arrows are rays from the source (X-ray tube) and the rays are detected by a suitable detector.

There are various geometries used in X-ray tomography and two important cases are introduced here. If the X-ray tube rotates around the object over a full angular range (360^0 or 180^o), one obtains a computed tomography (CT) geometry as Figure 4.1(a) shows. This geometry is widely used in X-ray imaging. On the other hand, if the X-ray tube rotates over a limited range of angles, one has a tomosynthesis geometry as shown Figure 4.1(b). Digital breast tomosynthesis system is an application of this geometry. The reconstructed 3D object can be decomposed into a set of transverse slices. Each one contains an image contribution mainly due to the breast object in that slice, but also contains "out-of-focus" contributions from nearby slices. The spatial resolution for the 3D DBT image is non-isotropic. The high resolution, same as

detector resolution, is retained in the two dimensions lying in the transverse plane (parallel to the detector plane) as seen in Figure 4.2, while a lower resolution applies in the z-dimension.

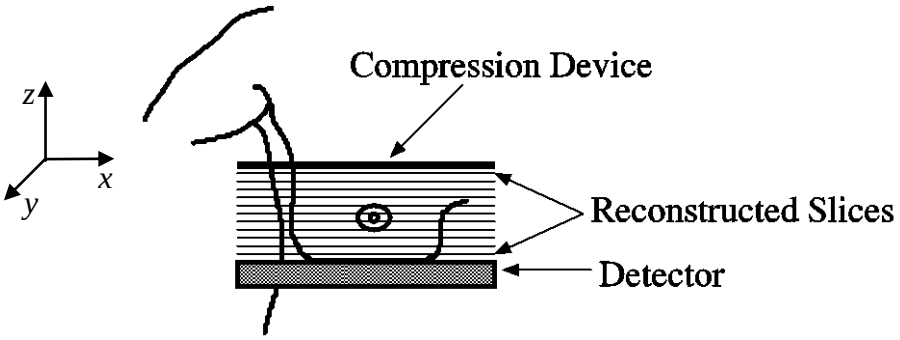

Figure 4.2: The reconstructed tomosynthesis slices are parallel to the detector images plane and the spatial coordinate is defined.

Before we go into details of reconstruction, we take a extremely simple example to help understand the idea of reconstruction. A 2D object is composed of 4 blocks as Figure 4.3 shows. The attenuation coefficients are homogenous within each block and labeled as μ_1, μ_2, μ_3, μ_4. We assume the projection scenario where the line integrals are measured in the horizontal, vertical, and diagonal directions. For simplification, we just set the path length equal to unity along all directions. Four measurements in total are selected in this example which composes a set of independent equations,

$$\begin{aligned} g_1 &= \mu_1 + \mu_2, \\ g_2 &= \mu_3 + \mu_4, \\ g_3 &= \mu_1 + \mu_3, \\ g_4 &= \mu_1 + \mu_4. \end{aligned} \tag{4.3}$$

Four independent equations are established for four unknowns. From elementary algebraic knowledge, we can, practically speaking, get a unique solution to this problem. If we generalize the problem to a case where the object is composed of N by N blocks , we need at least N^2 independent measurements to uniquely estimate the attenuation coefficient distribution of the object. When the object is divided more finely (equivalently N is larger), the task of solving sets of equations becomes quite impractical. Furthermore, in a DBT system, we do not have enough measurements to determine the attenuation uniquely. In a realistic example, a DBT system has 25 projection angles and the detector is composed 3584×2816 pixels. The number of equations

can add up to 10^8 and given the discretization of the object estimate the number of unknowns is more than 10^9. This even more problematic when we consider that there exist inevitable errors and noise in these measurements. Therefore, more efficient ways are needed to get a good estimation. For tomosynthesis, there is always too little information to solve for an accurate reconstruction. But the reconstruction that we can get is still clinically useful. One practical problem is the computational complexity of solving gigantic equations in so many unknowns.

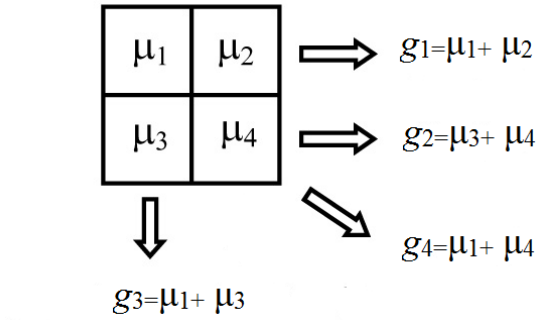

Figure 4.3: A 2D example of an object and its projection.

One remedy is called analytical reconstruction [50]. The idea of this method is the backprojection of line integrals. The process is like this, an individual measurement (the line integral part *g*) is backprojected by setting image pixels to the same value along the ray path. This means that the projection intensity is evenly distributed along the direction from which it was originally acquired as Figure 4.4(a) shows. The final reconstructed image is taken as the sum of backprojected measurements along all X-ray paths over projection angle views. So the location with high attenuation coefficient parts in the object will be enhanced more than that of low attenuation coefficient part by the convergence of different ray paths. The backprojection is conceptually simple, but it will blur the image contrast. Usually, people modify the projection image before the backprojection in order to get an estimated object with sharp contrast. The mathematical derivation comes from the Radon and inverse Radon transformation, which will be discussed in chapter 5.

Another remedy is called iterative reconstruction. This procedure aims to gradually change a image array per calculation loop until the estimation is quite close to the object. The basic idea is that we start with an initial guess for the object. Next, we calculate line integrals of this estimation along ray paths. This process is called forward projection. Then we calculate

differences between the forward projection and measured projection. We use these projection differences to update the estimation of the object. If the calculated line integral is lower than the measured sample, all the pixels along the ray are increased in value. Likewise, if the calculated one is higher than the measured sample, all of the pixel values along the ray are decreased. After the first complete computation loop, there is still an error between the computed projection with updated estimation and the measured values. This is because the change made for any one measurement disrupts all previous corrections. The idea of iterative reconstruction is that the errors become smaller with repeated iterations until the estimation converges to the proper solution. The choice of reconstruction can affect breast tomosynthesis image quality considerably. In Chapter 5, we will discuss reconstruction .

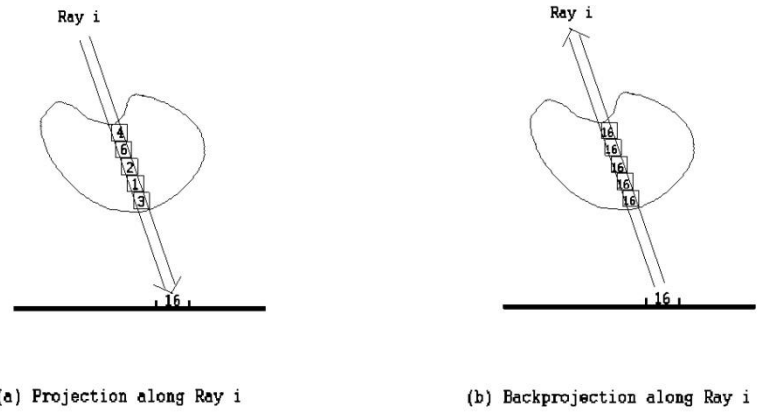

Figure 4.4: (a) The backprojection along the *ith* ray (b) the forward projection along the *ith* ray.

4.2 X-ray System

The DBT system is based on physics principles of X-ray production given in section 3.1. In this section, we shall discuss some different factors involved in the digital breast tomosynthesis system, which also can affect the reconstructed image quality.

4.2.1 Data Acquisition and Processing

Digital breast tomosynthesis system is similar to the digital mammography system. The X-ray source can rotate over a limited angle. There are two types of breast tomosynthesis geometries available: complete isocentric illustrated in Figure 4.5(a) and partial isocentric (stationary detector system) illustrated in Figure 4.5(b). In Figure 4.5, the relative distance of X-ray source

to detector as compared to breast-to-detector much smaller than it is in reality. This allows us to more cleanly depict acquisition modes as Figure 2.8(b). In a complete isocentric geometry, the X-ray tube and the detector are rotated simultaneously around a fixed central point over limited angular range while the stabilized breast is stationary during a scan. For the partial isocentric system, the stabilized breast and the detector remain stationary while the X-ray tube is rotated in an arc above the breast. In both geometries, the X-ray tube is pulsed to acquire different projection images at several angles. After the reconstruction processing, this set of projection images can provide tomographic slices that enable a radiologist to view a tomographic breast structure.

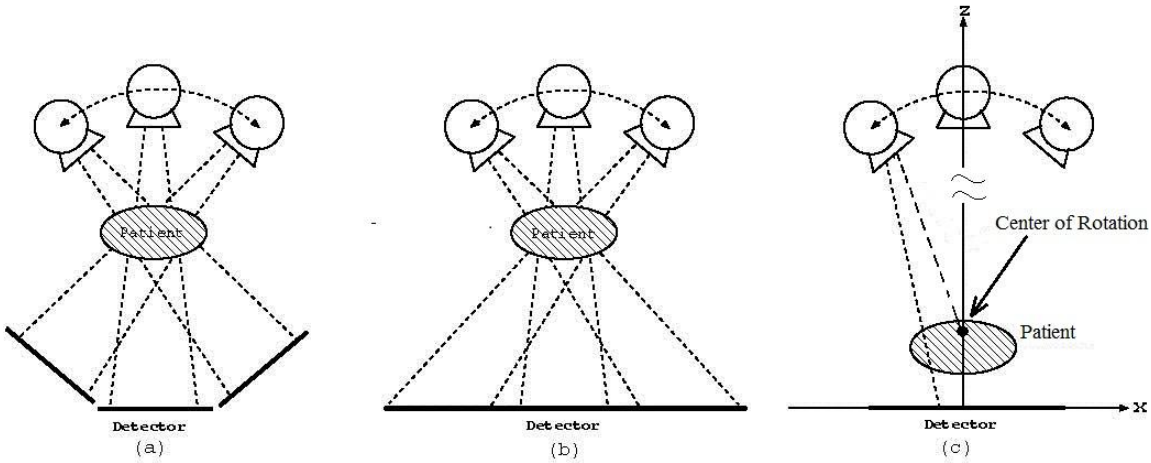

Figure 4.5: Tomosynthesis geometries (a) Complete isocentric motion in which both the X-ray tube and the detector rotate about a fixed central point. (b) Partial isocentric motion in which the detector is stationary and the X-ray tube rotates about some rotation points. (c) The COR is out of detector plane with stationary detector.

Typically, the center of rotation (COR) of X-ray source is not located in the detector plane. The angular range is defined between lines connecting the source and center of rotation point as seen in Figure 4.5(c). The angular range for breast tomosynthesis is from $\pm 15^{o}$ to $\pm 25^{o}$ [51] with a varying number of projection views. This limited angular range results in incomplete sampling causing some artifacts in the z direction. Although, more angular samples can provide more information about the object that is helpful to reconstruction, it might degrade the final image quality because of a dose constraint. First, more angular samples will make the projection images noisier. The total radiation dose to a patient at N_{angle} views is equal to that used for the two projection views of a conventional mammography. Since conventional screening mammography already uses a low dose, the distributed dose for each tomosynthetic projection view is extremely

low, yielding noisier data. These noisy data can affect the reconstructed image quality. Second, more angular samples mean more acquisition time, which means more possibility for patient motion during the scan, causing severe artifacts in the reconstruction image. In a digital breast tomosynthesis system, the X-ray tube has to be operated much faster than in screening mammography so that projection images can be acquired in a reasonable time (around 30 seconds) without significant patient motion. A reasonable number of views should be 11-25. Also, the angular schedule can affect image quality. Given a fixed number of angles, more angular samples near the boundary of the angular range result in a better resolution in the Z direction but poorer resolution in the XY plane. More samples near 0^o results in better XY images but poorer Z resolution [52]. This impact on lesion detectability may be important. Chen *et al.* [53] explored different acquisition techniques with different angular range and numbers of scan. Their result shows that the acquisition setting with 49 views over $\pm 25^o$ provided the best performance. However, considering the scan time and patient motion during the scan, the angular range and number of projection are smaller. In clinical prototype machines, GE provides one with 9 scans with $\pm 12.5^o$ angle range, Hologic Inc. provides one with 15 scans with $\pm 7.5^o$, and Siemens inc. provides 25 scans with $\pm 22.5^o$.

4.2.2 Focal Spot Size

For the digital breast tomosynthesis system, the typical X-ray source is not a point and the focal spot size is around 0.3mm, which can cause focal spot blur in the projection data. Ideally, if the X-ray source is a point, we can get a perfect reconstructed image with complete data acquisition. As discussed in section 3.1.1, the focal spot is an area in the X-ray tube. The image will be blurred by the superposition of rays from different areas of the focal spot.

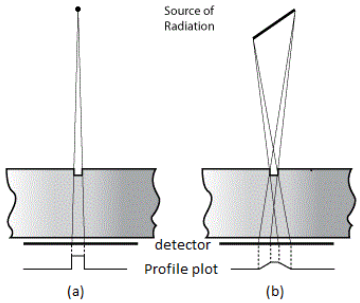

Figure 4.6: (a) A projection with a point source. (b) A projection with focal spot size.

Here is a 2D example. In the Figure 4.6(a), the radiation originates at a point source. Since all of the radiation originates from basically the same point, we can get a very sharp boundary in the image. In the second image, the source size is assumed as tilted line. Radiation rays from different parts of X-ray source passes through the object by different chords. The final profiles is the superposition of all attenuated rays, which give a notch with less sharp boundary, as Figure 4.6(b) shows.

4.2.3 Focal Spot Motion

During the scan with a DBT system, the X-ray tube moves along the arc over the detector. When it moves through specific projection angles, the X-ray tube will be turned on (no current passes through the cathode filament) and release amounts of radiation to patients. Digital breast tomosynthesis system has two different radiation exposure modes, step-and-shoot and move-and-shoot exposure.

The step-and-shoot mode means the X-ray tube fully stops at a projection angle, exposes certain amounts of radiation to a patient as acting approximately as point source as depicted in Figure 4.7(a). Then the tube is turned off and moves to the next angle. Theoretically, step-and-shoot mode can avoid any blur caused by tube motion. But step-and-shoot is challenging in mechanical design and can easily cause mechanical instability if scan time is short. For a practical breast tomosynthesis system, the set of projection images should be acquired quickly in order to avoid image artifacts from patient motions. If step-and-shoot is employed, a complete stop is applied at each angle view, hence requiring longer scan time. In that mode, patient motion might happen with higher possibility and cause artifacts in reconstructed images.

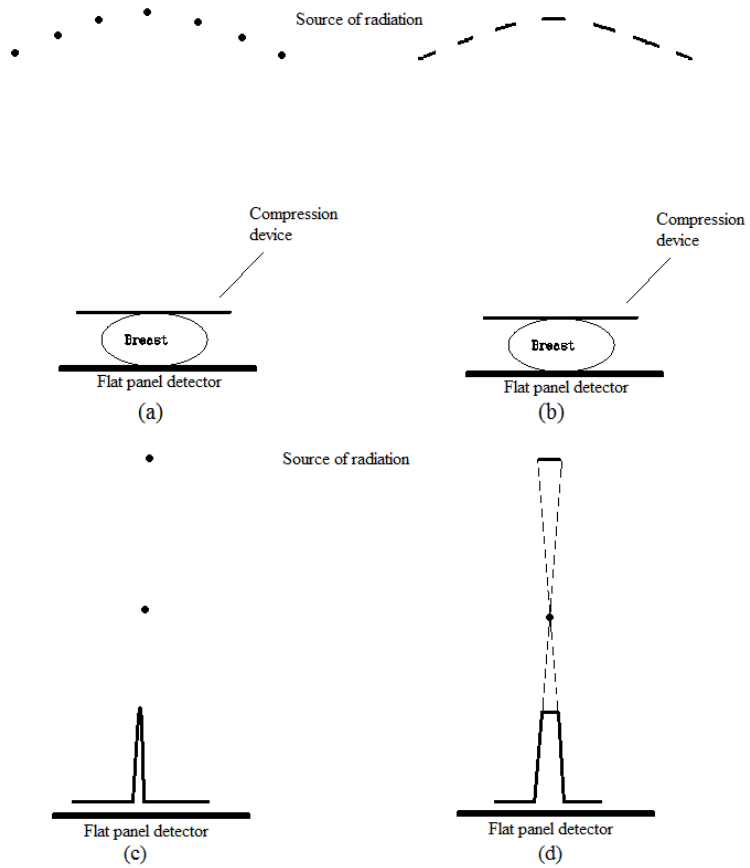

Figure 4.7: DBT system with ideal point source. (a) Step-and-shoot mode. (b) Move-and-shoot mode. in each case the dots in (a) and dashes in (b) indicate when the tube is firing as it travels. (c) Image of a point source after log step in step-and-shoot mode for one X-ray tube position. the small amount of the blur is due partly to focal-spot blur. (d) Same, but for continuous-tube motion X-ray firing. The considerable blur is due to mostly to focal-spot motion.

The move-and-shoot mode means that when X-ray tube moves close to a projection angle, it starts to expose radiation while the tube keeps moving. For this mode, the X-ray source size is seen as further stretched along the motion direction as depicted in Figure 4.7(b). The superposition of X-rays happens from the source at different positions, therefore introducing focal spot motion blur into the system. A study in [54] quantified the blurring effects on the acquired data. These are dependent on the details of digital breast tomosynthesis system geometry. Detailed comparison between these two modes are beyond the scope of this thesis. In this thesis, we focus on the move-and-shoot mode, also known as the continuous motion mode.

4.2.4 X-ray Spectrum Parameters for DBT

The X-ray spectrum is important to the final image quality in breast tomosynthesis. An improper spectrum can give a bad contrast in the projection data, which will be propagated to the breast tomosynthesis image through the reconstruction algorithm. Recall that the kV setting, together with target material and filtration, determines the energy spectrum of the X-ray photons. Higher kV shifts the spectrum to higher energy ranges. In general, the desired kV setting depends on the density and thickness of the breast, and target/filter materials. It is observed that thicker and denser (i.e. 100% glandular) breasts tend to require higher kV settings to obtain the best signal contrast. Since reduced breast compression is applicable in breast tomosynthesis, the X-ray kV needs to be raised a little in order to penetrate the thicker breast effectively. Zhao *et al.*[55] presented a theoretical study of the choice of kV using a-Se flat-panel digital detector. Their results showed that for tomosynthesis with 11 projection views, the optimal kV is at least 2-3 kV higher than the optimum spectrum for screening mammography. Glick *et al.*[56] investigated the effect of the kV setting using an indirect CsI based detector for DBT. Different detectors might require different optimal spectra, which in turn affects detectability. It was observed that the kV setting that gave best image quality was consistent with the result in Zhao's report.

Similar to kV setting, target/filter combinations can affect the energy spectrum. The optimization criteria for breast tomosynthesis differs from the ones for conventional mammography because of different acquisition protocols and data processing. Therefore, an examination of different target/filter combination is required for different cases. In a breast tomosynthesis system, there are usually four target-filter combinations: Mo-Mo, Mo-Rh, Rh-Rh and W-Rh. Zhao *et al.* [55] studied three different combinations (Mo-Mo, Mo-Rh and W-Rh) for a direct a-Se detector system. Their result showed that W-Rh was the optimal target/filter combination for all breast thickness (2-8cm). For different detector systems, the target/filter combination can be different. Glick *et al.* [56] explored the same three target/filter combinations. The results suggested that W-Rh provided better performance for tomosynthesis system using indirect CsI detector system than two other combinations (Mo-Mo and Mo-Rh).

4.3 Noise

There are several kinds of noise affecting tumor detection in the digital breast tomosynthesis system, Poisson noise, anatomical noise, and detector noise. They have important effects on image quality.

4.3.1 Poisson Noise

In X-ray production, X-ray emission follows a Poisson distribution like any electromagnetic radiation. That is, the number of photons emitted into 4π s.r. per unit time by the source follows a Poisson distribution. This noise is also known as quantum noise or radiation noise. Even after limited solid angle effects due to finite detector size and attenuation, the number of X-ray photons hitting the detector still follows a Poisson distribution. Note that quantum noise is inherent in the X-ray radiation, and cannot be eliminated by detection methods. The quantum noise effect can be relieved by increasing radiation dose since the relative amount of radiation noise vs. mean photon number decreases as the number photons grows. But this is not practical because higher dose means more photons, which will cause more damage to human tissues.

4.3.2 Anatomical noise in the breast

Anatomical noise as shown in Figure 2.7 is also referred as "structural noise", "object variability" or "clutter" [57]. It is an important influence on tumor detection. For example, if one drops a coin onto pebbles of similar size and color, it is hard to locate the coin since it is mashed by pebbles. This "clutter" effect was first modeled as a noise process by radar engineers facing similar problems in radar images. The fluctuations in attenuation of breast structures occur at many spatial scales. These attenuation fluctuations can be modeled as a stationary noise process and are propagated into the projection image still as a modified stationary noise process. In projection data, the breast anatomical noise power spectrum can be described in a power law form [58]. The anatomical noise can be propagated into the reconstruction and affects the tumor detection.

The anatomical structure includes normal breast components as discussed in section 3.2. Since some tumor attenuations are close to normal breast structure ones, the anatomical structure might contribute to a loss of lesion detection accuracy by masking them. Bochud *et al.* [59]

conducted a study for conventional mammography to demonstrate the importance of variations in background anatomy. The result suggested that the anatomical structural noise is a dominating effect on the detection of a large signal (like a mass). Anatomical noise effects on detection performance cannot be relieved simply by increasing the radiation dose. This is because the clutter noise and mean signal both grow at the same rate as dose is increased. Burgess *et al.* [60] have shown that both quantum noise and anatomical noise impeded visualization and reduced lesion detectability. It suggested that even if there was no other noise mechanism, the anatomical noise could reduce lesion detection accuracy considerably. We have devoted considerable efforts to relieve the anatomical noise to improve the detectability on masses as described in Chapter 6, using contrast-enhanced imaging.

4.3.3 Detector Effects

In a digital breast tomosynthesis system, the effects of the large area flat-panel detector can play an important role in image quality [55]. At the entrance to the detector plane, the attenuated X-ray field is spatially varying and corrupted by Poisson noise. When X-ray photons first hit the detector, a certain fraction of the photons are lost and the rest are absorbed and converted to the signal. Here, we just qualitatively summarize the behavior of digital breast tomosynthesis detectors.

Two different types of detectors, indirect and direct, are applied in the conversion. The CsI based amorphous silcon flat-panel detector is an indirect detector. An indirect detector [48] is a scintillator-based detector, where X-ray photons interact with phosphor, emitting a number of visible light photons increased by a gain factor. Thus, the number of optical photons can be described as a Poisson random variables multiplied a gain factor. These optical photons then propagate by a diffusion process to a photo-detector or silicon photodiode. One electron is produced for every absorbed photon. The optical diffusion results in a blob of optical photons at the interface of CsI and silicon. This spreading can be described as a convolution with a spread kernel. The resulting blob of electrons are integrated over small pixel areas, and additive Gaussian readout noise is added to the signal [12]. Thus the random number of electrons excited by optical photons does not follow a Poisson distribution anymore. The detector effects are difficult to characterize analytically after the detector transformation of the entering X-ray photon field. That is, probability of the number of electrons, and hence the level of the readout in

term, of current, is difficult to write analytically. However, with certain stationarity assumptions, linear cascaded modeling can be used to characterize the MTF (modulation transfer function) and NPS (noise power spectrum) changes induced by the detector [61]. But on average the number of electrons rises monotonically with the number of X-ray photons. The electrons are read out as current which is converted to a digital number by analog-to-digital converters. So the final output is a digital current measurement at each pixel rather than a number of photons. These measurements can be transferred to a computer for reconstruction processing.

The direct detection process is that the X-ray photons are transferred directly to electrons without an intermediate stage [34]. The a:Se (amorphous selenium) director is a direct detector. It is extensively described in [62]. Although these two types of detectors have different physics, they have something in common: (1) Both detectors are kinds of energy integrating detectors for X-ray photons rather than photon directly counting. The read-out for each detector pixel is proportional on average to incident X-ray photons. (2) Poisson noise is modified during the transformation in both detectors and extra detector noise is added the read-outs. The detector performance is described in input-output metrics such as detective quantum efficiency (DQE) [63]. The literature on detector performance is vast and beyond the scope of the present discussion.

4.4 Scatter

The scatter effects in breast imaging can degrade the image quality as discussed in section 3.1.2. At the low X-ray energies (25-40 kV) used in the breast imaging, the probability of absorption via photoelectric interaction within the breast is significant. However, the probability of Compton scattering of X-rays within the breast is still quite high. Even though a breast is of a relatively small size, scatter is still significant and it is still one significant source that reduces contrast. Around 33% to 50% of the total radiation photons would have experienced the deflection during the interaction in a breast [64]; i.e. the scatter-to-primary ratio (SPR) could be 0.5 to 1.0 depending on the thickness of the breast and X-ray energies.

The SPR in digital breast tomosynthesis applications has been studied by several groups. Sechopoulos *et al*. [64] reported a comprehensive analysis of scattering properties covering a

wide range of related parameters and investigated the magnitude and the distribution of scatter-to-primary ratio on DBT projection images intensively.

The most effective way to reduce scatter in 2D conventional mammography is using an anti-scatter grid. A grid is essentially a collimator placed atop the detector. The vanes are angled to point to the X-ray focal source. Undeflected photons follow straight paths from the focal spot to collimators and most can pass through the grid. Scattered photons that deviate from this straight line path and get absorbed by the collimator. Also, a grid can attenuate part of the primary radiation as well as scattered photons.

For most tomosynthesis geometries, grids are difficult to implement. For the partial-isocentric detector system for breast tomosynthesis, the detector rotates over the stabilized detector with a range. It would be very difficult to design an anti-scatter grid for this geometry because most primary X-ray photons would be blocked by the standard grid orientation with a large oblique angle [12]. For an isocentric geometry, grids are still not used in this imaging system to avoid grid line artifacts and high patient dose [65]. Since the exposure time for each projection in tomosynthesis is very short, it is difficult to avoid grid lines if a grid is used [12]. Zhao *et al.* [55] showed that the use of a grid is not beneficial for tomosynthesis acquisition because the grid will reduce the number of photons reaching the detector and then worsen the problem of detector noise.

Instead of blocking scattered photons with a grid, one might attempt to allow scattered photons to hit the detector, then try a digital scatter correction (SC) techniques after the scan. The basic SC idea is as follows: First, obtain an initial estimate of the attenuation object. Then, use this estimate to simulate, using a Monte Carlo packages, the flight of photons through the breast. From the Monte Carlo result, one can obtain an estimate of scatter and subtract it from the detector reading. The scatter-corrected images can then be used to obtain an improved reconstruction [66]. However, the scatter correction method based on Monte Carlo simulation is not practical in clinics due to the high computing power required. It can take hours to finish running Monte Carlo simulations. SC methods should be based on Monte Carlo simulation, and the effects of SC on lesion detection are still under investigation.

In mammography, there is an SC method based on a convolution-based scattering model [67]. The scatter process is assumed as a space invariant process and mainly depends on the object thickness only. Thus, the scatter radiation can be approximated as the convolution between the total radiation and scatter point spread function (sPSF) which can be measured experimentally [68]. In a DBT system, at each projection angle, the scatter process can be assumed to be modeled as a linear spatially invariant stationary process. The sPSF is measured per projection angle and SPR for different projection angles are calculated by convolution between sPSF and total radiation at that angle. This method is fast and should be a good approximation for SPR in the middle area of the breast image. However, in the area close to the breast boundary, the convolution model has a big deviation. The scatter process is not spatially invariant anymore because the thickness of breast varies near the boundary. In X-ray breast imaging, the scatter distribution is mainly depends on the thickness of a breast, thus the sPSF is not spatially invariant and the convolution method collapses nearby the breast boundary.

In sum, there are several SC methods and some are more accurate but computationally intensive than others.

4.5 Breast Compression in Tomosynthesis

In conventional mammography, breasts are highly compressed in order to reduce tissue overlap as discussed in section 3.3. The side view is shown in Figure 3.8(b) and the front view is shown in Figure 4.2. However, high compression pressure is not necessary for breast tomosynthesis imaging. The least possible compression is needed to pull tissues out of the chest wall and keep motion at minimum [69]. Therefore, there is the possibility of less painful compression using tomosynthesis. The compression is measured in force in units of Newtons [70]. Less compression means less force put on the breast though the compression pad. Furthermore, reduced compression can relieve discomfort. The discomfort with full compression in conventional mammography discourages some women from undergoing the exam. On the other hand, if the breast compression is reduced, the X-ray energies need to increase in order that X-rays more efficiently penetrate the dense breasts as discussed 4.2.4. Different X-ray energies with different compression degree (as measured for example by compression force on a paddle)

is a variable that can be adjusted to optimize lesion detection. No specific studies for tomosynthesis have been done to date.

4.6 Contrast-enhanced digital breast tomosynthesis (CE-DBT)

A digital breast tomosynthesis system can provide a 3D picture of breast slice by slice. Therefore, it can improve the detectability of tumors by reducing the possibility of mistaking the superposition of tissues as a potential tumor. However, mass tumor detection in breast imaging is a complicated detection task. Some masses might be deadly malignant masses and others benign ones. They have attenuation coefficients close each other. Thus they look similar in the gray scale image. Misdiagnosis of them may put a lot of physical and psychological distress on patients. Furthermore, for some malignant masses it is still difficult to differentiate them with normal breast anatomies. The attenuation of mass tumors sometimes is also quite similar to normal tissues [51]. Thus, in the 2D picture, the malignant tumors might look like normal tissues. Contrast-enhanced digital breast tomosynthesis aims to improve the conspicuity of malignant masses by reducing the masking effects of breast background tissue.

The idea of contrast-enhancement is that women are intravenously injected with a contrast agent in breasts. A contrast agent is a material that is readily seen on an X-ray image. Such agent can diffuse in breast tissues through blood vessels. Tumor growth and metastasis are accompanied by angiogenesis, the development of new blood vessels with increased permeability [42]. As a result, the absorption of contrast agents is often different in cancerous breast than in normal and benign breast tissues [71]. In a short time after the injection, the contrast agent will concentrate around the malignant tumors for a while. In breast X-ray imaging, the contrast agents are usually based on iodine [72]. The reasons are: (1) The energy level of X-ray breams used in the breast imaging is typically low, (below the 50 keV on average). (2) The attenuation coefficient of iodine has a sudden increase above 33.2 keV. This means structures taking iodine-based contrast agent are much more attenuating at high X-rays energies than all other structures in the breast thus are enhanced in DBT images. There are two ways images are evaluated, both of them are under investigations. One is to look at the image where the iodine concentration peaks, typically around one minute post injection [73]. Regions having high uptake

flow reflect active tissue growth and may be indicative of malignant tissues. Another method is known as kinetic analysis [74]. In this method, the flow of the iodine into and out of a tissue area is analyzed. It has been shown that malignant cancers often exhibit a rapid wash-in and wash-out of iodine while benign tissues have a slow uptake of iodine over the five minutes duration [75]. There are two basic image acquisition protocols for CE-DBT, temporal subtraction (TS) CE-DBT and dual energy subtraction (DE) CE-DBT.

4.6.1 CE-DBT: Temporal Subtraction

For temporal subtraction, as Figure 4.8(a) shows, the lightly compressed breast will be scanned under a DBT system before the injection of the contrast agent with a high energy (HE) spectrum, where most photon energies are around above 33.2 keV. This set of projection images is called the pre-contrast images, consisting of several 2D projection images at several projection angles. Next, an iodine-based contrast agent is injected intravenously into the breast. During the injection, the breast is kept compressed to avoid a big shift from patient motion. After the injection, the breast takes another scan at the same energy and with the same scan condition (breast location and DBT system parameters) as the pre-contrast scan. Projection images acquired in this way are called post-contrast images. In some initial studies [70, 76], three to five post-contrast images at intervals of 1 minute are acquired. In the image processing steps, pre-contrast and post-contrast images are first logarithmically transformed. Next, the post-contrast images are subtracted per pixel from the pre-contrast ones at corresponding projection angles. Ideally, the recorded information of the breast is the same between the pre-contrast and post-contrast projection images except for the concentrated iodine part. Thus, the subtraction step can remove the background tissue information but keep the information on concentrated iodine. The subtracted images are the input data for the reconstruction algorithm, and the reconstruction image can provide a more clear 3D description of suspicious masses compared with DBT images. The Figure 4.9(a) gives an example of TS CE-DBT image. This image demonstrates the malignancy(arrow) which is highlighted in the zoomed area.

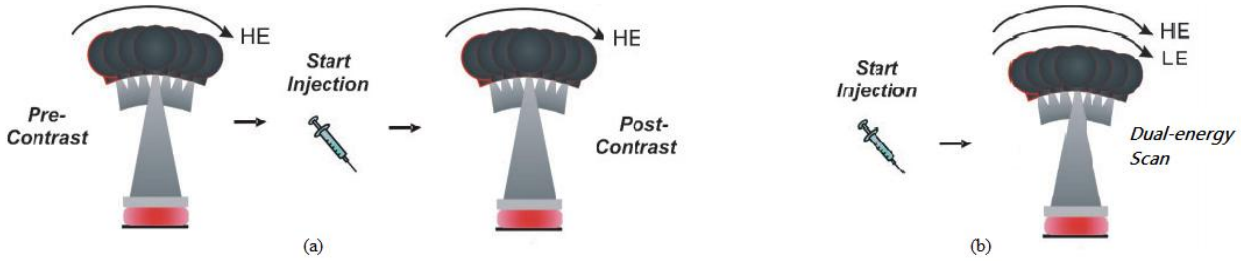

Figure 4.8: Illustration of image acquisition sequence. (a) Temporal subtraction method. (b) Dual-energy subtraction method.

In practice, it takes some time to inject contrast agents between the pre-contrast and post-contrast image acquisition with the breast compression. Patients probably move during the injection time interval even with the compression. This causes the mismatched location of the breast between pre-contrast images and post-contrast images. Thus the subtraction will leave some artifacts, called motion artifacts, which will be propagated into the reconstruction image, degrading the reconstruction image quality. As a matter of fact, motion artifacts have an important impact in TS CE-DBT [51]. Motion artifacts could be reduced by more pronounced compression of the breast but that would lead to more patient discomfort if done for several minutes and might affect the blood flow diffusion through breast vascular, thus affecting the contrast enhancement as shown in the zoomed area of Figure 4.9(a) .

4.6.2 CE-DBT: Dual-energy Subtraction

In order to overcome the potential motion artifacts and keep a good visualization of contrast agents, the dual-energy subtraction technique is proposed. The strategy is that the contrast agent is injected into a breast and subsequent acquisition of two sets of images is done at high energy (HE) and low energy (LE) as Figure 4.8(b) shows. After the logarithmic transformation for each set, HE images undergo a weighted subtraction from LE images with a weight for optimal visualization of the iodine contrast, which is called a weighted log subtraction [77]. In this strategy, there is no time gap between two acquisitions due to the injection. Thus, it reduces the possibility of patient motion during the scan.

The idea of enhancement in DE is a little complicated compared with TS. For projection data, the concentrated iodine has no sudden attenuation increase in LE images but are highlighted in HE images. Recalling that attenuation coefficients decrease with increasing the X-ray energy spectrum, the weighted subtraction aims to rescale the LE images to a level comparable with the

HE images and cancel the background tissues information in the HE pictures as much as possible. Thus the subtraction weight is dependent on the HE and LE energy spectrums [78] because the attenuation coefficients are energy dependent. The subtracted images will be reconstructed into a 3D DBT image by enhancing the concentrated iodine part as Figure 4.9(b) shows. If we compare the clip displacement in the zoomed area of Figure 4.9(b) is smaller than the one in Figure 4.9(a). But the DE method did not cancel the background noise as well as TS method did.

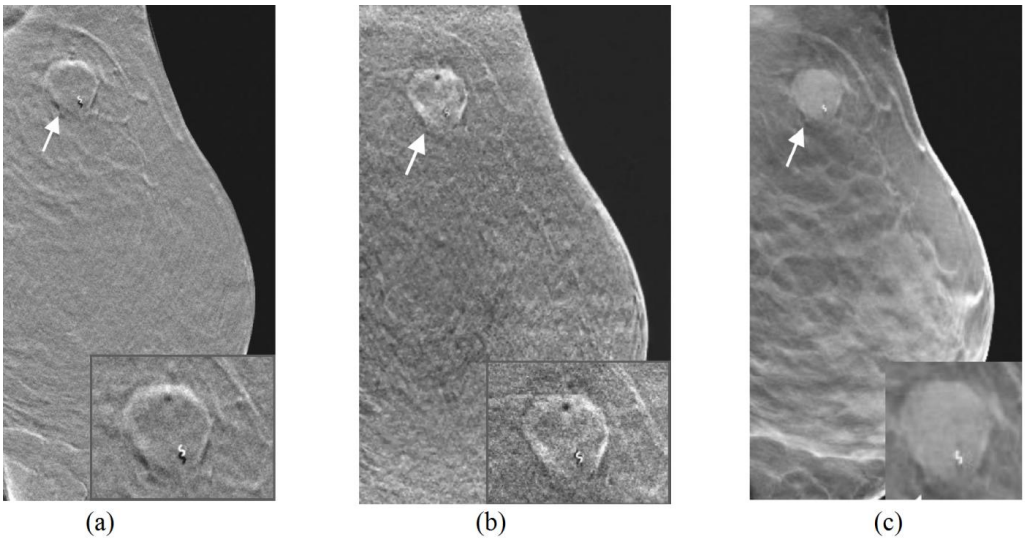

Figure 4.9: The FBP reconstruction of a slice of the same breast with an invasive ductal carcinoma using different modalities. Suspicious rim enhancement was demonstrated on both CE-DBT techniques. (a) The focal slice of reconstruction using a Temporal subtraction CE-DBT modality. The post-contrast image is acquired 90 seconds after the injection. The clip (white and black "sine wave" squiggle) in the lesion shows a displacement around 2 mm because of the patient motion between pre- and post-contrast image acquisition. (b) The focal slice of reconstruction using dual-energy CE-DBT modality. The HE and LE projection images are acquired 90 seconds after the injection. (c) The focal slice of reconstruction with the DBT modality.

DE CE-DBT holds promise to provide new and supplemental diagnostic information for improved cancer detection [79]. Its implementation requires careful attention to the acquisition and processing techniques to provide best image quality at lowest total radiation dose. Furthermore, given the total radiation dose, the dose split between HE and LE also affects the image quality. Hu *et al.*[80, 81] analyzed the signal and noise acquired by the a-Se detector with a Tungsten (W) target, using a cascaded linear system model. It included the effect of detector performance, X-ray spectra, system geometry, filters for FBP reconstruction as well as the effect of structural noise. The system acquires 25 views over an approximately 50 degrees angular range with move-and-shoot mode. The X-ray tube was enabled with potentials from 23 and 49 kV and employs three filters, 0.05mm rhodium (Rh) for low energy acquisitions and 0.3mm

copper (Cu) or 1.0mm titanium (Ti) for high energy views. The structural noise was determined using the CIRS model 020 phantom. The total radiation dose is consistent with conventional mammography. The results show that the optimal image quality is achieved with relevant X-ray energies (25 kV for Rh filtered spectra 49 kV for Cu filtered spectra) by dose split between HE and LE with ratio 1.8:1.

Basically, the HE and LE images are acquired at two complete DBT scan loops (two-loop-scan) in consecutive order. The two-loop-scan takes around 1 minute. There is still a possibility that patients will move during the scan and the compression of the breast is pretty much uncomfortable with compression. The idea of an interleaved DE acquisition protocol is proposed to relieve these effects. The method integrates the two loop scans into one DBT scan by alternatively acquiring HE and LE images. One HE image is acquired at one projection angle and for the next projection angle, a LE image is acquired at the next scan angle. This protocol induces different data processing methods. We will focus on this interleave method and evaluate the image quality in the rest of the thesis.

Chapter 5

Image Reconstruction in Transmission Imaging

As we point out in Chapter 4, the goal of transmission tomography, including tomosynthesis breast imaging, is to obtain an estimate of the attenuation coefficient map of a patient breast. There are two main geometries in transmission tomography: general CT and tomosynthesis geometry. Many reconstruction methods can be applied to these geometries and these reconstruction can be classified into two categories: analytical and iterative reconstruction [82]. Analytical reconstruction such as the filtered backprojection (FBP) algorithm tries to restore the object in the continuous spatial domain with simple imaging models. Iterative reconstruction such as simultaneous algebraic reconstruction (SART) technique can incorporate some sophisticated imaging models. Both FBP and SART algorithms are based on deterministic method, which means they do not include a noise model during the reconstruction. On the other hand, there is another type of iterative reconstruction, called statistical reconstruction. It incorporates noise model (Quantum and detector noise) of the acquisition data into its reconstruction method to improve image quality. However, because of the complex X-ray detector effect, it is extremely difficult to apply a noise model in the reconstruction methods and we do not talk about statistical reconstruction in details. In the following, we first model the transmission imaging system and discuss the mathematical formulations for FBP and SART.

5.1 The Imaging model representation for Object and Projection

5.1.1 Image formation for Transmission Imaging

We start with the general transmission scanning geometry. Given a point source, a small discrete detector element are connected by a narrow X-ray beam or "ray", we can use the symbol i (i = 1,...N) to index different rays, i.e. a ray connecting the source and a detector bin. Note that one physical detector element can be associated with many rays during the acquisition. For simplicity, we use a two dimensional (2D) object to help understand the image formation illustrated in Figure 5.10. We show an object illuminated by one unscattered X-ray and one

scattered ray. We may define the object of two space coordinates, x and y, by $\mu(x,y)$ or $\mu(\mathbf{r})$, where $\mathbf{r}$ is a vector expressed by (x,y). For 3D case, $\mathbf{r}$ is a vector expressed by (x,y,z).

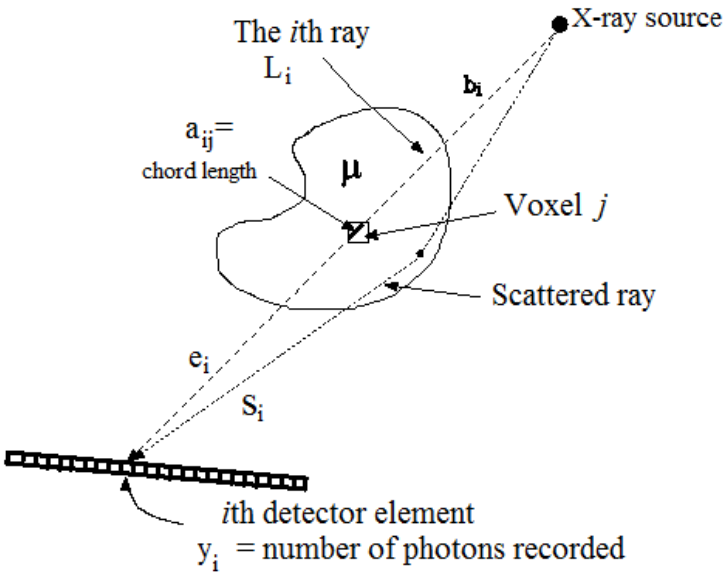

Figure 5.10: A beam of X-ray is shown propagating through a cross-section of the object. The detector is composed of many small pixel elements. One unscattered and one unscattered rays are shown.

As discussed in Chapter 3, the unit of $\mu(x,y)$ should be in the unit of cm^{-1}. Let b_i denote the number of incident X-ray photons in the ith ray entering the object, called the blank scan. Let e_i be the number of photons exiting through the ith ray and y_i be the number of photons detected by the ith detector element. And s_i is the scattered photons detected by the ith detector element. In Figure 5.10, the illustration is idealized in several ways. In reality, first the X-ray source is not a point source, but has finite dimensions due to the finite focal spot size. Second, the detector bin is small but not a point. The source extends a small solid angles as seen from the bin. The object voxels have finite width. As a result, the number of X-ray photons that pass through a given voxel and hit a given detector element (bin) is the result of a complex geometrical calculation (e.g. a volume calculation over a voxel). For mathematical simplification, if we think the X-ray source is monoenergetic, the width of the ray is sufficiently small and only one ray hits one detector bin, we can express the relationship between b_i and e_i based on the Lambert-Beers law in section 3.1.2 for the ith ray:

$$e_i = b_i \exp\left(-\int_{L_i} \mu(\mathbf{r})dl\right)_i, \quad i = 1,...,N. \tag{6.1}$$

where L_i is the line between the source and detector for the *i*th ray and the line integral is calculated along the *i*th ray as shown in Figure 5.10. In the following, we talk more about the integral part in Equation (6.1).

5.1.2 Object and Projection Representations

The quantity of interest in transmission tomography (i.e. breast tomosynthesis) is the linear attenuation coefficient map $\mu(\mathbf{r})$, which is a continuous function. We can represent $\mu(\mathbf{r})$ with a finite parameterization. For simplicity, the continuous function $\mu(\mathbf{r})$ can be viewed on a digital display with a finite number pixels, $\{\mu_j\}_{j=1,...,M}$, by integrating over the *j*th pixel area,

$$\mu_j = \int_{-\infty}^{\infty}\int_{-\infty}^{\infty}\int_{-\infty}^{\infty} \mu(\mathbf{r})\xi_j(\mathbf{r})d\mathbf{r} \tag{6.2}$$

where *M* is the number of voxels in the object, and $\xi_j(\mathbf{r})$ is the basis function. The conventional basis is the "pixel" basis for 2D and "voxel" basis for 3D. In this thesis, we use rect functions as our voxel basis. The voxel basis $\xi_j(\mathbf{r})$ is 1 inside the *j*th voxel, and is 0 otherwise. Thus voxel basis function is given by,

$$\xi_j(\mathbf{r}) = \text{rect}\left(\frac{x - x_j}{\Delta a_x}\right)\text{rect}\left(\frac{y - y_j}{\Delta a_y}\right)\text{rect}\left(\frac{z - z_j}{\Delta a_z}\right) \tag{6.3}$$

where,

$$\text{rect}(x) = \begin{cases} 1 & |x| \le \frac{1}{2} \\ 0 & |x| > \frac{1}{2} \end{cases} \tag{6.4}$$

In, Equation (6.3), (x_j, y_j, z_j) is the center coordinates of *j*th voxel and $\Delta a_x, \Delta a_y, \Delta a_z$ are the voxel widths in *x*,*y*,*z* directions respectively. Thus, the voxel could be cubic or rectangularoid.

With introducing the voxel basis, we can represent the 3D continuous object, $\mu(\mathbf{r})$, by a vector, $\boldsymbol{\mu} = \{\mu_j; j = 1,...,M\}$, whose element μ_j is the average value of $\mu(\mathbf{r})$ in the jth voxel. Intuitionally, the digitized object should be displayed as a 3D digital matrix by 3D voxel basis. In our project, the 3D discrete matrix is transformed to a vector by row-by-row and plane by plane scanning the matrix and then linking one row after another and one plane after another [83]. This is called lexicographic ordering. Thus, $\mu(\mathbf{r})$ is approximated as follows,

$$\mu(\mathbf{r}) \approx \sum_{j=1}^{M} \mu_j \xi_j(\mathbf{r}) \tag{6.5}$$

Plugging Equation (6.5) into the line integral part in Equation (6.1), we can get the following equation:

$$\int_{L_i} \mu(\mathbf{r}) dl \approx \int_{L_i} \sum_{j=1}^{M} \mu_j \xi_j(\mathbf{r}) = \sum_{j=1}^{M} \mu_j \int_{L_i} \xi_j(\mathbf{r}) dl = \sum_{j=1}^{M} a_{ij} \mu_j \tag{6.6}$$

where $a_{ij} = \int_{L_i} \xi_j(\mathbf{r}) dl$ is the line integral along the ith ray through the jth basis function. The unit of a_{ij} is *cm*. In practice, a_{ij} can be simply understood as the chord length of the ith ray passing through the jth pixel. The method to calculate these chord lengths is based on the Siddon's ray-tracing method [84]. The detailed discussion is beyond this thesis. We can represent $\{a_{ij}\}$ by the $N \times M$ matrix $\mathbf{A}$, called system, whose ith row and jth column element is a_{ij}. The ideal model in Equation (6.1) becomes the discrete one:

$$y_i^{ideal} = b_i \exp(-[\mathbf{A}\boldsymbol{\mu}]_i), \quad i = 1,...,N. \tag{6.7}$$

where

$$[\mathbf{A}\boldsymbol{\mu}]_i = \sum_{j=1}^{M} a_{ij} \mu_j \tag{6.8}$$

The system matrix **A** depends only on the system geometry. As a remainder, the imaging model Equation (6.7) is ideal since it does not take into account any noise (i.e. Poisson noise and electronic noise) or polyenergetic X-ray source effects. But, such system matrix is extremely important since it give a simple mathematical description of the tomography system. Any more sophisticated reconstruction methods are based on this idea of description. In our project, the

object space $2000 \times 1000 \times 50$ digital breast for the breast tomosynthesis system. The projection data are acquired over 11 angles using a $1800 \times 2400 (18cm \times 24cm)$ detector, the size of the system matrix in single precision format is 19008000 GB ($2000 \times 1000 \times 50 \times 1800 \times 2400 \times 11 \times 4$ bytes). Thus, **A** must be computed on the fly rather pre-computed and saved in computer memory during the reconstruction.

5.1.3 Forward Imaging Model

After building up a mathematical model of the physical imaging system, we talk about a forward model which is an important step in addressing the inverse problem of reconstruction. Also, we talk about the possibility of extending the simple imaging model Equation (6.7) to include noises (Quantum and Poisson noise), polyenergetic effects of the X-ray source, and also scatter events although we did not implement in our project. For reconstruction algorithms, they are tightly correlated with forward imaging model. Generally speaking, the more accurate forward imaging model we use, the better image quality we can get.

As mentioned in Chapter 3 we know that the X-ray source emits a random number of photons whose count distribution is Poisson. Hence, b_i's are a random variables (r.v.) and the number of detected photons y_i are therefore also random. We represent the detector readouts as a vector $\mathbf{y} = \{y_i; i = 1, ...N\}$. There exist some additional counts recorded, primarily caused by Compton scattering, which is also Poisson r.v.[85]. A common way to model scatter events is using an additive term denoted by s_i even though the scatter effects can be reflected in the system matrix $\mathbf{A}$, which will make **A** more complicated and hardly incorporated into the reconstruction algorithm implementation.

Given the stochastic model, we shall redefine the terms used below: b_i denotes a Poisson r.v. representing the number of photons emitted by the X-ray tube along the *i*th ray during the exposure time, y_i^{pre} the r.v. representing the total number of photons before they interact with the detector for the *i*th ray, s_i the Poisson r.v. representing the number of photons from scatter events

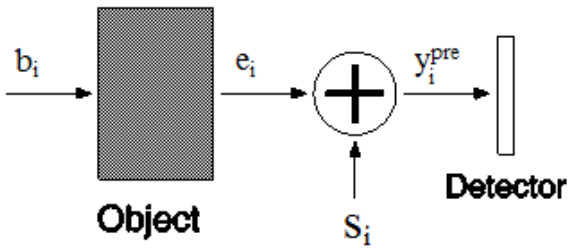

Figure 5.11: Pseudo-physical interpretation of the transmission data.

for the *i*th ray and e_i the random number of photons without being scattered along the *i*th ray as seen in Figure 5.10. Therefore, we can write down the relationship as illustrated in Figure 5.11,

$$y_i^{pre} = e_i + s_i \tag{6.9}$$

In section 5.4, we show that e_i and y_i^{pre} follow a Poisson distribution with mean $\bar{b}_i \exp\left(-[\mathbf{A\mu}]_i\right)$ and $\bar{b}_i \exp\left(-[\mathbf{A\mu}]_i\right) + \bar{s}_i$, where $\bar{b}_i$ is the mean of b_i and $\bar{s}_i$ is the mean of s_i. Thus, our forward imaging model for transmission measurements is:

$$y_i^{pre} \overset{\text{i.i.d.}}{\sim} Poisson\left\{\bar{b}_i \exp\left(-[\mathbf{A\mu}]_i\right) + \bar{s}_i\right\} \tag{6.10}$$

In the medical imaging field, the item $\bar{b}_i$'s are determined by the "blank scan": transmission scans with air only between the source and detector [86]. These scans can experience a long duration. Thus, the estimated blank scans contain much less variability (both Quantum and detector noise are ignorable) than other transmission measurements with less exposure time. Therefore, we use the symbol b_i, called blank scan, as a known non-random parameter instead of $\bar{b}_i$. Therefore, Equation (6.10) can be,

$$y_i^{pre} \overset{\text{i.i.d.}}{\sim} Poisson\left\{b_i \exp\left(-[\mathbf{A\mu}]_i\right) + \bar{s}_i\right\} \tag{6.11}$$

Equation (6.11) includes the effects of Quantum noise and scatter effects only. It does not model the polyenergetic effect and electronic detector noise.

The discussion above assumes a monoenergetic X-ray source. Practically, the photons emitted by X-ray source tube has a wide energy spectrum as mentioned in Chapter 3. Thus, the blank

scan b_i is energy-dependent. Also, the attenuation coefficient $\boldsymbol{\mu}$ is energy-dependent because of the interaction between photons and matters. Then, we can rewrite Equation (6.11) by:

$$y_i^{pre}(\varepsilon) \overset{\text{i.i.d.}}{\sim} Poisson\left\{b_i(\varepsilon)\exp\left(-[\mathbf{A}\boldsymbol{\mu}(\varepsilon)]_i\right)+\bar{s}_i(\varepsilon)\right\} \tag{6.12}$$

The total X-ray photons passing though the object for each *i*th ray and before hitting the detector should be expressed by integrating over the energy spectrum:

$$\begin{aligned} y_i^{pre} &= \int y_i^{pre}(\varepsilon)d\varepsilon \\ &\overset{\text{i.i.d.}}{\sim} \int\left\{Poisson\left(b_i(\varepsilon)\exp\left(-[\mathbf{A}\boldsymbol{\mu}(\varepsilon)]_i\right)+\bar{s}_i(\varepsilon)\right)\right\}d\varepsilon \end{aligned} \tag{6.13}$$

Since the summation of Poisson random variable is still a Poisson random variable, we can safely interchange the operations "$\int$" and "*Poisson*". Therefore, our forward model is given by,

$$y_i^{pre} \overset{\text{i.i.d.}}{\sim} Poisson\left\{\int\left(b_i(\varepsilon)\exp\left(-[\mathbf{A}\boldsymbol{\mu}(\varepsilon)]_i\right)+\bar{s}_i(\varepsilon)\right)d\varepsilon\right\} \tag{6.14}$$

In reality, the data we got is the final read-out through the detector. We use the symbol y_i for the final data, which includes the detector effects. In Chapter 4, we discussed the complex effects of detector noise. It not only corrupts the Poisson distribution of y_i^{pre} but also adds correlation to y_i^{pre}. Noise models for imaging forward depend on the type of detector and each type is extremely complex and difficult to be described mathematically. Thus, some researches treat the detector noise as a correlated Gaussian noise and some just ignore the detector noise, assuming $y_i \approx y_i^{pre}$ [16]. In the following, since we do not apply the statistical reconstruction in the DBT system, we just treat y_i as a set of noisy data. Furthermore, in the model for reconstruction algorithm, we assume photons are monoenergetic.

5.1.4 Forward-projection and Back-projection

Since, the accurate likelihood of acquisition data y_i is hardly defined because of the complex X-ray detector effects. So, we turn to deterministic approaches to transmission tomography which begins with estimating the line-integral from the ideal model, Equation (6.1). In this way,

we do not model Poisson noise and detector noise in our reconstruction. The ideal line-integral estimates:

$$l_i = \int_{L_i} \mu(\mathbf{r}) dl \quad i = 1, ..., N \tag{6.15}$$

where l_i denotes the line integral of attenuation coefficients of the voxel along the *i*th ray path. We can obtain the estimate g_i of l_i by log-transform of our actual acquisition data, y_i as follows:

$$g_i = \log\left(\frac{b_i}{y_i - \bar{r}_i} \right) \tag{6.16}$$

Note that y_i's and g_i's are noisy measurement data and their accurate statistical properties are complex. The mean of g_i, $\bar{g}_i = l_i$. Since Poisson noise and detector noises are ignored in this deterministic way, we give the relation between $\bar{g}_i$ and l_i,

$$g_i \approx \bar{g}_i = l_i \tag{6.17}$$

Then, we can calculate the estimate of object, $\hat{\boldsymbol{\mu}}$ from $\{g_i\}$ using some reconstruction algorithms. Given the discrete notation discussed above, we can rewrite Equation (6.17),

$$\bar{g}_i = [\mathbf{A}\boldsymbol{\mu}]_i = \sum_{j=1}^{M} a_{ij} \mu_j, \quad i = 1, ..., N \tag{6.18}$$

Since Equation (6.18) is a series of linear equations, it can be represented as a linear system,

$$\mathbf{g} \approx \bar{\mathbf{g}} = \mathbf{A}\boldsymbol{\mu} \tag{6.19}$$

where $\mathbf{g}$ is a line integral vector with *N* elements and $\bar{\mathbf{g}}$ is the mean of $\mathbf{g}$. This linear system model is the basis for reconstruction in deterministic method. The reconstruction is an inverse problem and its goal is to solve this linear system, where $\mathbf{A}$ and $\mathbf{g}$ are known and $\boldsymbol{\mu}$ is unknown. This linear system is inconsistent since $\mathbf{g}$ contains noise and underdetermined due to the limited angle effect. Conventionally we call the forward-projection operation along *i*th ray as,

$$[\mathbf{A}\hat{\boldsymbol{\mu}}]_j = \sum_{j=1}^{M} a_{ij} \hat{\mu}_j \tag{6.20}$$

where, $\hat{\boldsymbol{\mu}}$ is one estimate of the attenuation map whose element is $\hat{\mu}_j$. In this way. we can get an estimated projection given $\mathbf{A}$. Also, we can define a back-projection operation for *j*th pixel or voxel as,

$$[\mathbf{A}^T\mathbf{h}]_i = \sum_{i=1}^{N} a_{ij} h_i \tag{6.21}$$

where $\mathbf{h}$ should be generalized projection data. It can be the noisy line integral $\mathbf{g}$, processed line integral or estimated projection. As mentioned in Chapter 4, the backprojection operation is performed by smearing a set of projection images uniformly back into the object space along the incident X-ray paths. Both operation are important for any reconstruction algorithms.

5.2 Filtered-Backprojection (FBP) for DBT systems

5.2.1 Introduction of classical FBP algorithm

The FBP method is an analytical reconstruction algorithm. It is a Fourier transform (FT) based algorithm applied on line integral projections which are supposed to be acquired with parallel beams and full projection angle range, like the CT geometry [87]. The theory behind the FBP algorithm is the central slice theorem (CST) [25]. With a 2D object, the theorem claims that the FT of a projection profile in the Fourier domain has the same orientation of the projection line as shown in Figure 5.12. With the full projection angle range and large number of angular samplings, the FT of projection lines can cover the whole Fourier domain (the spatial-frequency space). A complete two-dimensional (2D) FT of the object cross-section can be obtained by summing up these FT of projection lines as shown in Figure 5.13. Theoretically, once we get these FT of projection profiles, we can restore the object by doing the 2D inverse Fourier transform (iFT) of the 2D FT of object's cross-section [88] .

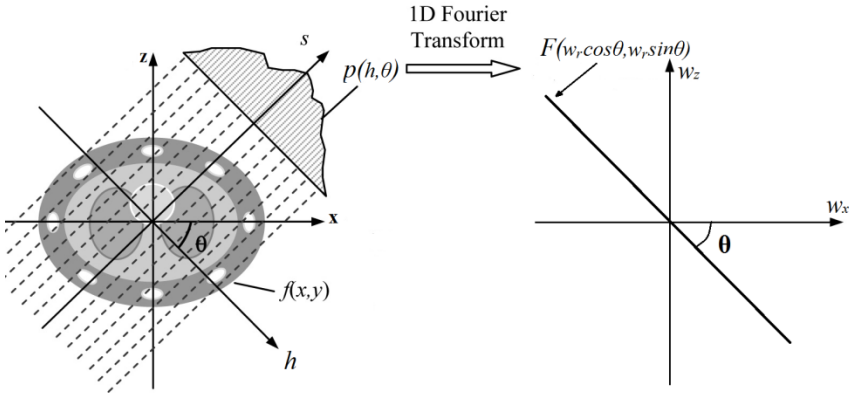

Figure 5.12: The illustration of the central slice theorem for a 2D project. *f(x,z)* is a object function, *p*(*h*,θ) is the projection profile along angle θ in polar coordinate system. w_r is the radial spatial frequency in Fourier domain. The central slice theorem says that $F(w_r,\theta)$ is the Fourier transform of *p(h,θ)*.

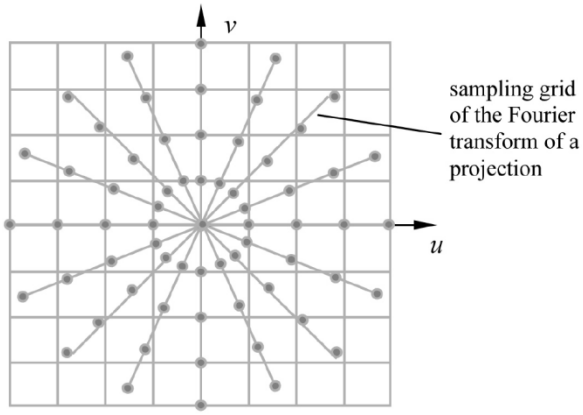

Figure 5.13: Sampling pattern in Fourier space based on the central slice theorem.

Ideally, if the FT of a projection is shaped as a sliced pie in Figure 5.14(a), we can obtain 2D FT of the object by simply summing up. Unfortunately, in the spatial frequency space, the FT of each projection is shaped as a strip [50], as shown in Figure 5.14(b). If we simply sum up these FT of all projections that are spaced over 2π, the center region is artificially enhanced and outer regions are underrepresented. To get the ideal pie-shaped region with the strip-shaped region, we can multiply the strip-shaped FT by a weighting function that has a lower intensity near the center and higher intensity near the edge as shown in Figure 5.14(c). Usually, we call such filter as ramp filter. The net effect of the ramp filter is to maintain the same "mass" as the summation of the pie-shaped wedges if we do the summation of the filtered strips.

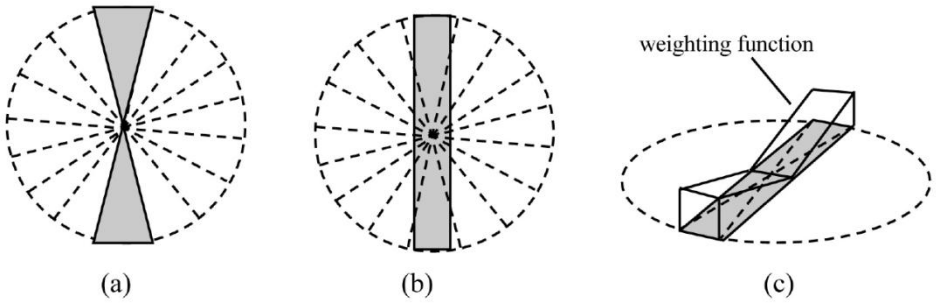

Figure 5.14: Illustration of the filtered backprojection concept. (a) ideal frequency sampling data form one projection, (b) actual frequency sampling data from one projection, and (c) weighting function in the frequency domain to approximate ideal conditions.

In practice, we do the 1D iFT of projection data line by line after filtering and then sum them up to restore the object rather than do the summation first in Fourier domain then do the 2D iFT. The reason is that the sampling pattern produced in the Fourier domain is non-Cartesian. Samples from different projections falls on a polar coordinate grid as shown in Figure 5.13. To perform a 2D iFT, these samples must be interpolated to a Cartesian coordinate. Such interpolation in Fourier domain will introduce an error on a single Fourier sampling and affects the appearance of the entire image after the iFT.

For the convenience of mathematical description in below, we follow the notation in Figure 5.12 in continuous space. We think of discrete line-integral through log-transform as continuous function rather than a discrete vector, $\mathbf{g}$. Let's say that we have a 2D object $f(x,z)$ and the projection file at angle θ is expressed as $p(h,\theta)$ in the polar coordinate system where $h = x\cos\theta+z\sin\theta$. The FT of $p(h,\theta)$ is $F(w_r,\theta)$ as Figure 5.12 shows. In the spatial-frequency space, we can say $w_r = w_x\cos\theta + w_y \sin\theta$ by the CST. If the projection angle range cover 360^o, we have the conventional FBP algorithm [87]

$$f(x,z) = \int_{-\pi/2}^{\pi/2} Q(h,\theta)d\theta = \int_{-\infty}^{\infty} F(w_r,\theta)\left|w_r\right| e^{\zeta 2\pi w_r h} dw_r \qquad (6.22)$$

where $Q(h,\theta) = \int_{-\infty}^{\infty} F(w_r,\theta)\left|w_r\right| e^{\zeta 2\pi w_r h} dw_r$ and ζ is the imaginary number.

The FBP reconstruction can be implemented in three steps:

1. Get Fourier transforms of the projection images:

$$F(w_r,\theta) = \mathrm{FT}\left\{ p\left(h,\theta\right)\right\}$$

2. Apply the ramp filter $|w_r|$ to the Fourier transformed and inverse Fourier transform on $F(w_r,\theta)$:

$$Q(h,\theta) = \int_{-\infty}^{\infty} F(w_r,\theta)|w_r|dw_r$$

3. Backproject the filtered projection data $Q(h,\theta)$ to restore the object in continuous space:

$$f(x,z) = \int_{-\pi/2}^{\pi/2} Q(h,\theta)d\theta \quad \text{where } h = x\cos\theta + z\sin\theta$$

For digital implementation, we process the backprojection in Equation (6.21). The pre-condition is that the forward imaging geometry is parallel beam.

5.2.2 FBP for the DBT system with stationary detector

The DBT system has three deviations comparing with the conventional FBP algorithm. First, the projection data are acquired with limited projection angle range, say $-\alpha \le \theta \le +\alpha$, where $\alpha \le 90^0$. Thus, we cannot restore an accurate estimation of the object due to the lack of a complete information of the object. Secondly, projections from the DBT system are acquired with the cone beams rather than parallel beams. However, the distance between X-ray source and center of rotation is around 15 times as the distance between the COR and detector as Figure 5.14(c) shows. For a breast with a reasonable size (2~5 cm thickness), it is safe for us to assume that the acquisition geometry is with parallel beams. Thirdly, for the DBT system we study, projection data are acquired with a stationary detector rather than an isocentric detector. This means that for an oblique projection angle θ, the hitting rays pass through the object are not perpendicular to the detector line as shown in Figure 5.15. Thus we cannot directly apply the CST to the projection data to build the FBP algorithm. So, we need re-define the FBP algorithm with the new system geometry. For the followings, the DBT system in this thesis means the Tomo geometry with the stationary detector and we mainly discuss how to apply FPB algorithm with the DBT geometry. For the convenience of explanation, we start with a 2D system although the actual DBT system is 3D. Later, we show the extension to 3D.

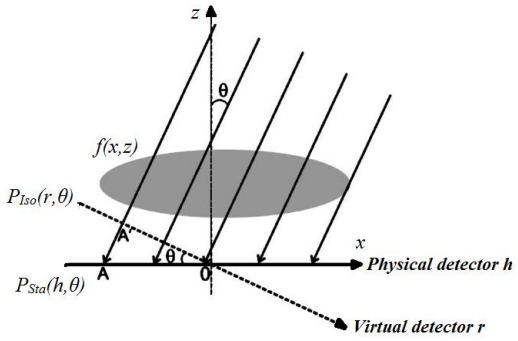

Figure 5.15: The illustration of virtual detector and physical detector. The dash line r is for virtual detector and the line is for stationary physical detector. *f(x,z)* is the 2D object. At projection angle *θ*, $P_{\text{Sta}}(h,\theta)$ is the projection data acquired by the physical (stationary) detector. $P_{\text{Iso}}(h,\theta)$ is the projection acquired by the virtual detector.

5.2.3 Definition of notation

In DBT system, let's say *f*(*x*,*z*) represents our 2-D object. The coordinate system (*x*,*z*) is consistent with one slice of the DBT system along y direction in Figure 5.2. As Figure 5.15 shows, $P_{\text{Sta}}(h,\theta)$ is the projection of the line integral at angle θ with the stationary detector where the detector axis *h* is overlapped with x axis. Here, "Sta" means stationary geometry. Let $S_{\text{Sta}}(v,\theta)$, be the FT of the projection $P_{\text{Sta}}(h,\theta)$,

$$S_{\text{Sta}}(v,\theta)=\int_{-\infty}^{+\infty}P_{\text{Sta}}(h,\theta)e^{-\zeta 2\pi hv}dh \tag{6.23}$$

where $S_{\text{Sta}}(v,\theta)$ is called as stationary Fourier slice and *v* is the corresponding spatial frequency. Since CST does not directly apply to $P_{\text{Sta}}(h,\theta)$, we do not know the orientation of $S_{\text{Sta}}(v,\theta)$ in spatial-frequency space so far. In order to establish the relation between $S_{\text{Sta}}(v,\theta)$ and the CST, we introduce the virtual detector axis *r* [89]. At one projection angle θ, the detector line *r* is virtually placed as perpendicular to the X-ray beam as Figure 5.15 shows in dash line. The projection data acquired by virtual detector is defined as $P_{\text{Iso}}(r,\theta)$. Here, "Iso" means isocentric geometry. Also, we put a constraint on virtual projection data,

$$P_{\text{Sta}}(h,\theta)=P_{\text{Iso}}(r,\theta)\qquad \text{if } r=h\cdot\cos\theta \tag{6.24}$$

We define the isocentric Fourier slice, $S_{\text{Iso}}(\omega_r,\theta)$ as the FT of $P_{\text{Iso}}(r,\theta)$ for a projection angle θ. We can apply the CST to $S_{\text{Iso}}(\omega_r,\theta)$ since $P_{\text{Iso}}(r,\theta)$ is acquired with isocentric detector

virtually and say that ω_r is the radial frequency along angle θ in the spatial-frequency space. On the other hand, we can apply the CST to $S_{\text{Sta}}(v,\theta)$ indirectly by mapping $S_{\text{Sta}}(v,\theta)$ to $S_{\text{Iso}}(\omega_r,\theta)$. Then, we can build up a FBP algorithm for the DBT system. In section 5.5, we show that isocentric and stationary Fourier slices have one-by-one correspondence,

$$S_{\text{Iso}}(\omega_r,\theta) = S_{\text{Sta}}(\omega_x,\theta)\cdot\cos\theta, \qquad \omega_x = \omega_r\cdot\cos\theta \text{ and } \omega_z = \omega_r\tan\theta \tag{6.25}$$

Furthermore, we also show that the spatial frequency, $v = \omega_x$. So, the stationary Fourier slice, $S_{\text{Sta}}(v,\theta)$ can be expressed as $S_{\text{Sta}}(\omega_x,\theta)$.

In the spatial-frequency space, a cone area can be constructed by $S_{\text{Iso}}(\omega_r,\theta)$ with the CST for the limited projection angle range ($-\alpha \le \theta \le +\alpha$) as Figure 5.16 shows. Unlike the CT system, we can see that we lose much low frequency information along ω_z and ω_x, the null area outside the cone area. Thus, given the DBT system, the object cannot be reconstructed accurately. Actually we can only get an approximated estimation of the object following the classical FBP algorithm but the spatial resolution of the estimation along z direction will be pretty much poor.

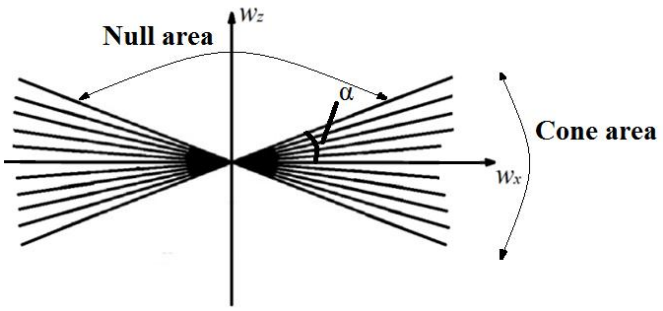

Figure 5.16: The illustration of Fourier domain where α is the half angular range.

5.2.4 FBP for DBT system in 2D

Now, we show how to get a reasonable estimation, $\hat{f}(x,z)$ for the object, $f(x,z)$ given the DBT projection data, $P_{\text{Sta}}(h,\theta)$, where $-\alpha \le \theta \le +\alpha$ and $\alpha \le 90^o$ from the classical FBP algorithm. Similar to the classical FBP algorithm, we apply the ramp filter, $|\omega_r|$ on $S_{\text{iso}}(\omega_r,\theta)$ and take iFT on them,

$$Q_{\text{Iso}}(r,\theta)=\int_{-\infty}^{+\infty}S_{\text{Iso}}(\omega_r,\theta)|\omega_r|e^{\zeta 2\pi\omega_r r}d\omega_r \tag{6.26}$$

where $Q_{\text{Iso}}(r,\theta)$ is the filtered samplings with isocentric geometry. Then, we backproject $Q_{\text{Iso}}(r,\theta)$ under the isocentric geometry to estimate the object approximately,

$$\hat{f}(x,z)\sim\int_{-\alpha}^{+\alpha}Q_{\text{Iso}}(r,\theta)d\theta=\int_{-\alpha}^{+\alpha}\int_{-\infty}^{+\infty}S_{\text{Iso}}(\omega_r,\theta)|\omega_r|e^{\zeta 2\pi\omega_r r}d\omega_r d\theta \tag{6.27}$$

Comparing with Equation (6.22), the biggest difference in Equation (6.28) is the smaller integral range over the angle. On the other hand, for the backprojection, $\int_{-\alpha}^{+\alpha}Q_{\text{Iso}}(r,\theta)d\theta$ it is based on the isocentric geometry (the dash line in Figure 5.15) rather than the stationary geometry (the line in Figure 5.15). Although the line integral paths are same for both geometries, the sampling positions in detector lines are different, which will cause a little difference when Equation (6.28) is implemented digitally. For the package in our lab, we implement the backprojection following the stationary geometry for the geometrical consistency with physical detector. Thus, we need to build a specific FBP for the stationary detector. Start with Equation (6.27), we substitute $S_{\text{Iso}}(\omega_r,\theta)$ with $S_{\text{Sta}}(\omega_x,\theta)$ using Equation (6.25) and define the filtered samplings with stationary detector,

$$Q_{\text{Sta}}(h,\theta)\equiv Q_{\text{Iso}}(r,\theta)=\int_{-\infty}^{+\infty}S_{\text{Sta}}(\omega_x,\theta)\frac{|\omega_x|}{\cos\theta}e^{\zeta 2\pi\omega_x h}d\omega_x \tag{6.28}$$

where $r=h\cdot\cos\theta$ and we use the relation, $\omega_x=\omega_r\cdot\cos\theta$. Then, we put Equation (6.28) into Equation (6.27) and we can get the same approximated estimation as,

$$f(x,z)\sim\int_{-\alpha}^{+\alpha}Q_{\text{Sta}}(h,\theta)d\theta=\int_{-\alpha}^{+\alpha}\int_{-\infty}^{+\infty}S_{\text{Sta}}(\omega_x,\theta)\frac{|\omega_x|}{\cos\theta}e^{\zeta 2\pi\omega_x h}d\omega_x d\theta \tag{6.29}$$

where $S_{\text{Sta}}(\omega_x,\theta)$ is the FT of $P_{\text{Sta}}(h,\theta)$. In Equation (6.29), we design a specific FBP algorithm dealing with the backprojection in the stationary geometry. Here, we define a new ramp filter, $\tilde{H}_{RA}(\omega_x)=\frac{|\omega_x|}{\cos\theta}$ for the stationary geometry.

For the digital implementation, Equation (6.29) is still not a proper form since the integral over ω_x goes to infinity. Thus, we need to truncate ω_x by assuming that the FT of projections in the stationary geometry are band limited with the uniform frequency cut-off, Γ. In other words, $S_{\text{Sta}}(\omega_x,\theta)$ has zero energy outside the interval $(-\Gamma,\Gamma)$ along the ω_x for all projection angles. Under this assumption, the FBP algorithm in Equation (6.29) is expressed as,

$$\begin{aligned} f(x,z) &\sim \int_{-\alpha}^{+\alpha}\int_{-\Gamma}^{+\Gamma} S_{\text{Sta}}(\omega_x,\theta)\frac{|\omega_x|}{\cos\theta}e^{\zeta 2\pi\omega_x h}d\omega_x d\theta \\ &= \int_{-\alpha}^{+\alpha}\int_{-\Gamma}^{+\Gamma} \tilde{H}_{RA}(\omega_x)\cdot S_{\text{Sta}}(\omega_x,\theta)e^{\zeta 2\pi\omega_x h}d\omega_x d\theta \end{aligned} \tag{6.30}$$

Practically, to ensure the aliasing-free sampling, the projection bandwidth Γ must satisfy the Nyquist sampling criterion:

$$\Gamma = \frac{1}{2\delta} \quad \text{cycles/mm} \tag{6.31}$$

where δ is the projection sampling interval in the stationary detector in millimeters (or the interval between two nearby detector bins) and Γ is usually called Nyquist frequency. Then the Equation (6.30) can be implemented digitally by the sampling theorem with the cut-off frequency in Equation (6.31). We can define the truncated ramp filter for the stationary geometry,

$$\tilde{H}_{RA}(\omega_x) = \begin{cases} |\omega_x| \big/ \cos\theta & |\omega_x| \le \Gamma \\ 0 & \text{Otherwise} \end{cases} \tag{6.32}$$

Now, we want to understand the cut-off frequency effect on the FT of the object in the spatial-frequency space, the cone area in Figure 5.15. Again, we turn to virtual detector to apply CST indirectly in to the truncated stationary Fourier slices, $S_{\text{Sta}}(\omega_x,\theta)$ where $\omega_x \in (-\Gamma,\Gamma)$. Given the relation between the physical detector and virtual detector in Equation (6.24) and (6.25), the truncated isocentric Fourier slices, $S_{\text{Iso}}(\omega_r,\theta)$ still has the form in Equation (6.25) and the cut-off range for the radial frequency ω_r should be $(-\Gamma/\cos\theta\ ,\ \Gamma/\cos\theta)$ given the relation in Equation (6.25), where $\Gamma/\cos\theta$ is cut-off frequency for ω_r and angle dependent. Furthermore, this cut-off frequency for ω_r satisfies the Nyquist sampling criterion. Actually, in

order to match the constraint of virtual detector in Equation (6.24), the virtual detector sampling interval should be $\delta \cdot \cos\theta$ if the real detector sampling interval is δ. Then, the Nyquist sampling criterion is automatically satisfied $\frac{\Gamma}{\cos\theta} = \frac{1}{2\delta \cdot \cos\theta}$ cycles/mm. So, the FT of the object in the spatial-frequency space becomes a bow-tie shape as shown in Figure 5.17(a) with the band limit assumption. Thus, Equation (6.30) becomes,

$$\hat{f}(x,z) \sim \int_{-\alpha}^{+\alpha} Q_{\text{Iso}}(r,\theta)d\theta = \int_{-\alpha}^{+\alpha}\int_{-\Gamma/\cos\theta}^{\Gamma/\cos\theta} S_{\text{Iso}}(\omega_r,\theta)|\omega_r| e^{\zeta 2\pi\omega_r r} d\omega_r d\theta \tag{6.33}$$

and truncated ramp filter, $H_{RA}(\omega_r,\theta)$ along the radial frequency is,

$$H_{RA}(\omega_r,\theta) = \begin{cases} |\omega_r| & \omega_r \le \Gamma/\cos\theta \\ 0 & \text{otherwise} \end{cases} \tag{6.34}$$

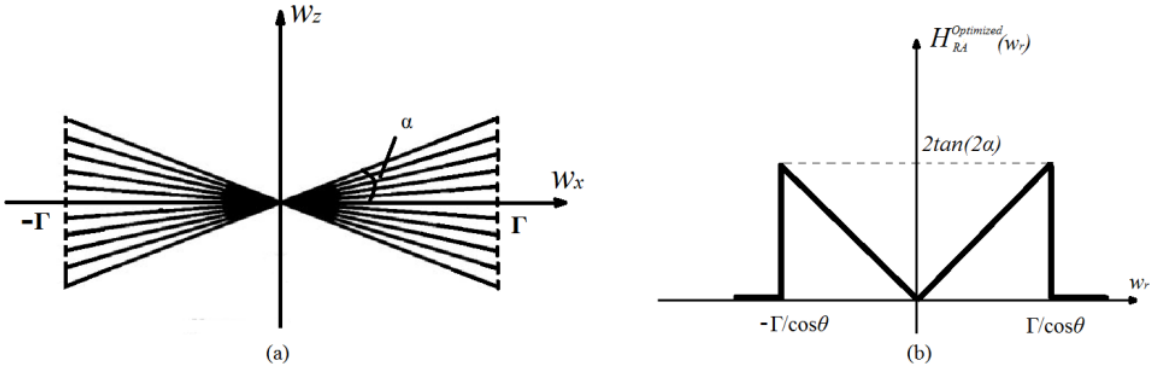

Figure 5.17: (a) The band limited bow-tie area in the spatial frequency domain. (b) The optimized band limited Ramp filter for stationary geometry.

5.2.5 General FBP for 3D DBT system

For 3D DBT system, the y axis is perpendicular to the x-z plane and the corresponding spatial frequency ω_y is perpendicular to the $\omega_x - \omega_z$ plane in Figure 5.3. Thus, we have a 2D projection images at one angle rather than a profile. The CST claims that the 2D FT of a projection image in the Fourier domain has the same orientation of the projection image in the spatial domain. Thus, all the stuff we discussed above in 2D can be extended to 3D. The stationary and isocentric profile line become planes with the same relation,

$$P_{\text{Sta}}(h, y, \theta) = P_{\text{Iso}}(r, y, \theta) \qquad \text{if } r = h \cdot \cos\theta \tag{6.35}$$

and in Fourier domain, we have,

$$S_{\text{Iso}}(\omega_r, \omega_y, \theta) = S_{\text{Sta}}(\omega_x, \omega_y, \theta) \cdot \cos\theta, \qquad \omega_x = \omega_r \cdot \cos\theta \text{ and } \omega_z = \omega_r \tan\theta \tag{6.36}$$

where ω_r is the radial frequency in $\omega_x - \omega_z$ plane, same definition as in Equation (6.25) rather than a true radial frequency in 3D space.

Then, for a 3D object $f(x, y, z)$ we have a 2D projection image $P_{\text{Sta}}(h, y, \theta)$ whose 2D FT is $S_{\text{Sta}}(\omega_x, \omega_y, \theta)$.

Moreover, Mertelmeier *et al*. [90] gives the optimized the ramp filter $H_{RA}^{Optimized}(\omega_r, \theta)$ for the isocentric projection image,

$$H_{RA}^{Optimized}(\omega_r, \omega_y, \theta) = \begin{cases} 2 \times \tan(2\alpha) \times \dfrac{|\omega_r|}{\Gamma / \cos\theta} & \omega_r \le \Gamma_x / \cos\theta, \ \omega_y \le \Gamma_y \\ 0 & \text{otherwise} \end{cases} \tag{6.37}$$

where 2α is total projection angular range, ω_r has the same definition in Equation (6.36) and Γ_x and Γ_y are the cut-off frequency defined as

$$\Gamma_x = \frac{1}{2\delta_x} \quad \text{and} \quad \Gamma_y = \frac{1}{2\delta_y} \text{ cycles/mm} \tag{6.38}$$

where δ_x and δ_y are the projection sampling interval along *x* and *y* direction in the stationary detector in millimeters. In this thesis, $\delta_x = \delta_y$. Actually $H_{RA}^{Optimized}(\omega_r, \omega_y, \theta)$ is a normalized ramp filter with the cut-off frequency, $\Gamma / \cos\theta$. Figure 5.17(b) shows one slice along the ω_y. In our project, we use this optimized ramp filter to get an approximated 3D image reconstruction. For the geometry consistency for backprojection, we need to transform the optimized ramp filter to one in the stationary geometry. With the relation in Equation (6.36), the optimized ramp filter for the 3D stationary geometry is given by,

$$\tilde{H}_{RA}^{Optimized} = \tilde{H}_{RA}^{Optimized}(\omega_x, \omega_y, \theta) = \begin{cases} 2 \times \tan(2\alpha) \times \dfrac{|\omega_x|}{\Gamma_x} & \omega_x \le \Gamma_x,\ \omega_y \le \Gamma_y \\ 0 & \text{otherwise} \end{cases} \tag{6.39}$$

Here, it does not have a cosθ item in the denominator of Equation (6.39) unlike the Equation (6.37). Thus, the FBP algorithm for 3D DBT system becomes,

$$f(x,y,z) \sim \int_{-\alpha}^{+\alpha} \int_{-\Gamma_y}^{+\Gamma_y} \int_{-\Gamma_x}^{+\Gamma_x} \tilde{H}_{RA}^{Optimized} \cdot S_{\text{Sta}}(\omega_x, \omega_y, \theta) e^{\zeta 2\pi\omega_x h} e^{\zeta 2\pi\omega_y y} d\omega_x d\omega_y d\theta \tag{6.40}$$

where $\tilde{H}_{RA}^{Optimized}$ is defined in Equation (6.39).

In a clinical setting, there are factors that might degrade the image quality from FBP algorithm, like noise and aliasing along z direction. During the filtering process in spatial-frequency space, we can apply other kinds of filters to Fourier slices by dot production. This can been seen as a convolution between projection data and filter kernels in spatial space for the property of Fourier transform. Generally, the FBP algorithm can be expressed,

$$f(x,y,z) \sim \int_{-\alpha}^{+\alpha} \int_{-\Gamma_y}^{+\Gamma_y} \int_{-\Gamma_x}^{+\Gamma_x} H \cdot \tilde{H}_{RA}^{Optimized} \cdot S_{\text{Sta}}(\omega_x, \omega_y, \theta) e^{\zeta 2\pi\omega_x h} e^{\zeta 2\pi\omega_y y} d\omega_x d\omega_y d\theta \tag{6.41}$$

where "·" means multiplication point by point and "*H*" stands for different filters (one or more) we apply to Fourier slices.

For the DBT system, noises in projection samplings are independent Poisson noises and are distributed over whole spatial frequency axis. The shape of the ramp filter given above is a high-pass filter. Thus it can suppress the low frequency noises. To suppress the high frequency noises, we use a new filter, called the Spectral apodization (SA) filter defined in $\omega_x - \omega_y$ plane and same plane along ω_z,

$$H_{SA} = H_{SA}(\omega_x, \omega_y) = \begin{cases} 0.5\left[1 + \cos\left(\dfrac{\pi\omega_x}{A \cdot \Gamma}\right)\right] & |\omega_x| \le A \cdot \Gamma (\text{ if } A \le 1) \text{ or } |\omega_x| \le \Gamma (\text{ if } A \ge 1) \\ & \omega_y \le \Gamma_y \\ 0 & \text{otherwise} \end{cases} \tag{6.42}$$

where *A* defines the width of cutoff frequency in ω_x direction. By multiplication with the stationary Fourier slices, the SA filter can reduce the high frequency noises because $H_{SA}(\omega_x)$ goes to zero when ω_x goes beyond the cutoff frequency . In this thesis, we choose *A* = 0.75.

By sampling theorem, in spatial-frequency space, we should have periodic bow-tie shape Fourier slice ω_x and ω_z. In Figure 5.17(a), we just show the *0*th order. In tomosynthesis, the limited angle acquisition affects the spatial resolutions of the reconstruction along the *z* direction. Usually, the reconstruction pixel size along *z* axis is much larger than that along *x* direction. Thus, the Nyquist frequency along ω_z is much small and aliasing might occur [91]. This means the periodic cones along ω_z might overlap in the boundary as. To minimize aliasing along the ω_z

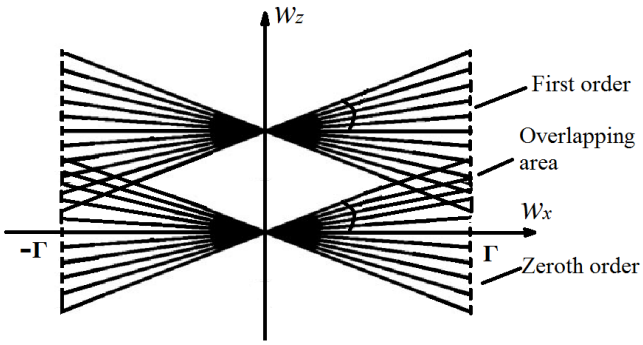

Figure 5.18: One slice of bow-tie Fourier slice sampling for different period. Each line represents the 2D Fourier slice.

direction, the Slice Thickness (ST) filter is applied. It is defined in $\omega_y - \omega_z$ plane and same plane along ω_x,

$$H_{ST}(\omega_y,\omega_z)=\begin{cases}0.5\left[1+\cos\left(\dfrac{\pi\omega_z}{B\cdot\Gamma}\right)\right] & \omega_y \le \Gamma_y,\ |\omega_z| \le B\cdot\Gamma \text{ and } |\omega_z| \le \Gamma\cdot\tan(\alpha) \\ 0 & \text{otherwise}\end{cases} \quad (6.43)$$

where *B* defines the width of cutoff frequency in ω_z direction. If we apply this filter into the bow-tie shape Fourier slice by dot production, the bow-tie shape Fourier slice is modified as Figure 5.19 shows. Comparing with the 2D Fourier slice in Figure 5.17, we cut the high frequency information (The dash part) along the ω_z where overlapping might happen. So, the cutoff frequency, $B\cdot\Gamma$ should be small enough to prevent aliasing between two nearby periods and not too small to degrade the image quality.

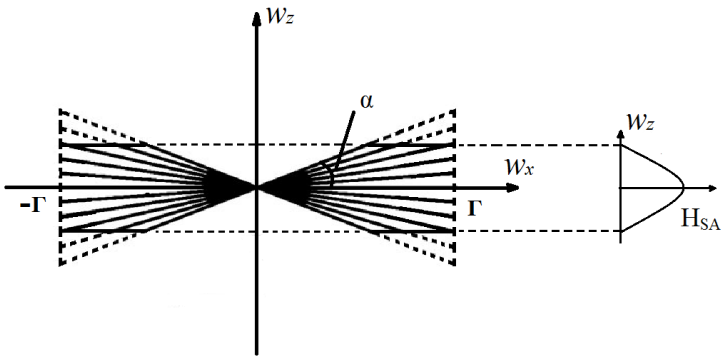

Figure 5.19: Illustration of SA filter in the Fourier domain.

From Equation (6.40), we can see the 2D iFT is processed over $\omega_x - \omega_y$, but ST filter is defined on $\omega_y - \omega_z$. We can transform the ST filter into the form in $\omega_x - \omega_y$ plane. Thus, it will simplify the dot multiplication in Equation (6.43) and we can apply ST filter directly on $S_{\text{Sta}}(\omega_x, \omega_y, \theta)$. From the relation in Equation (6.36), we know that $\omega_x = \omega_z \tan\theta$. Then we can express the ST filter on $\omega_x - \omega_y$ plane,

$$\tilde{H}_{ST} = \tilde{H}_{ST}(\omega_x, \omega_y) = \begin{cases} 0.5\left[1+\cos\left(\dfrac{\pi\omega_x}{B\cdot\Gamma}\right)\right] & \omega_y \le \Gamma_y, |\omega_x| \le \dfrac{B\cdot\Gamma}{\tan\theta} \text{ and } |\omega_x| \le \dfrac{\Gamma\cdot\tan(\alpha)}{\tan\theta} \\ 0 & \text{otherwise} \end{cases} \quad (6.44)$$

If we put the SA and ST filters into Equation (6.40) , we can give a general form of FBP algorithm,

$$f(x,y,z) \sim \int_{-\alpha}^{+\alpha}\int_{-\Gamma_y}^{+\Gamma_y}\int_{-\Gamma_x}^{+\Gamma_x} \tilde{H}_{RA}^{Optimized}\cdot H_{SA}\cdot\tilde{H}_{ST}\cdot S_{\text{Sta}}(\omega_x,\omega_y,\theta) e^{\zeta 2\pi\omega_x h} e^{\zeta 2\pi\omega_y y} d\omega_x d\omega_y d\theta \quad (6.45)$$

Where $\tilde{H}_{RA}^{Optimized}$, H_{SA}, $\tilde{H}_{ST}$ are defined in Equation (6.39), (6.42), (6.44).

In digital form, let us assume that the projection data is sampled with a sampling interval δ cm ($\delta_x = \delta_y = \delta$). The cutoff frequency is $\Gamma = \dfrac{1}{2\delta_x}$. Let the sampled projections be $P_{\text{Sta}}(k_x\delta, k_y\delta, \theta_t)$, where k_x, k_y and t take integers and θ_t represents for discrete projection angle in arc unit. The general FBP algorithm can for DBT system be implemented in three steps:

1. Perform the 2D discrete Fourier transform (DFT) of tomosynthesis projections $P_{\text{Sta}}(k_x\delta, k_y\delta, \theta_t)$ to get the stationary digital Fourier slices, $S_{\text{Sta}}(k_x\upsilon_x, k_y\upsilon_y, \theta_t)$ where υ_x and υ_y are sampling interval over frequency interval $(-\Gamma, \Gamma)$ along ω_x and ω_y direction,

$$S_{\text{Sta}}(k_x\upsilon_x, k_y\upsilon_y, \theta_t) = \text{DFT}\{\, P_{\text{Sta}}(k_x\delta, k_y\delta, \theta_t)\,\} \tag{6.46}$$

2. Apply digital version of the band limited transformed ramp filter, $\tilde{H}_{RA}^{Optimized}$, the SA filter, H_{SA} and the transformed ST filter, $\hat{H}_{ST}$, on $S_{\text{Sta}}(k_x\upsilon_x, k_y\upsilon_y, \theta_t)$ and take the inverse 2D discrete Fourier transform over limited frequency interval $(-\Gamma, \Gamma)$ to get filtered projection data,

$$Q_{Sta}(k_x\delta, k_y\delta, \theta_t) = \text{iDFT}\{\, \tilde{H}_{RA}^{Optimized} \cdot H_{SA} \cdot \tilde{H}_{ST} \cdot S_{\text{Sta}}(k_x\upsilon_x, k_y\upsilon_y, \theta_t)\,\} \tag{6.47}$$

3. Within the stationary geometry, backproject filtered projection data multiplying the spoke density *D*,

$$f(x, z) \simeq \text{Backproject}\{\; D \cdot Q_{Sta}(k_x\delta, k_y\delta, \theta_t)\;\} \tag{6.48}$$

The spoke density *D* comes from the item $d\theta$ in Equation (6.45). For the DBT system with equispaced angular sampling, the spoke density $D = \frac{2\alpha}{N-1}$, where *N* is the total number of projections. People propose the non-equispaced angular sampling in order to improve the detection of micro-calcification [92]. Thus, the spoke density should be projection angle dependent, $D(\theta_t)$ and is defined as,

$$D(\theta_t) = \left|\theta_t - \theta_{t-1}\right| \tag{6.49}$$

where $t > 1$ and if $t=1$, $D(\theta_1) = \left|\theta_2 - \theta_1\right|$

5.3 Simultaneous Algebraic Reconstruction Technique (SART)

SART is one of matrix inversion techniques to solve linear system model in Equation (6.19). There are several matrix inversion techniques applied in the transmission imaging system [87, 93]. Here, we just focus on SART algorithm and discuss this technique in detail, but not offer

any mathematical derivations since these are beyond the scope of the discussion. The derivation can be found from appropriate citations.

SART provides the estimate of the object, the linear attenuation map, $\boldsymbol{\mu}$ iteratively. With a initial guess of the estimated $\boldsymbol{\mu}$, this iterative procedure aims to gradually change the estimation array per calculation loop which is basically composed with forward-projection and back-projection operations in Equation (5.20) and (5.21). Both operations are related with the model of system matrix. SART is terminated when the estimation is quite close to the object. Actually, SART can incorporate sophisticated imaging models via the system matrix $\mathbf{A}$. This means that we can incorporate an arbitrary imaging geometry in modeling the system matrix without changing the reconstruction algorithm itself, for example, the arbitrary X-ray tube motion orbit (not an arc orbit) and cone beams geometry. As a reminder, for FBP algorithm, if we switch the imaging geometry from parallel beams to a cone beams geometry, the algorithm needs to be modified in a complex way to accommodate the new geometry [94].

We deal with the large-scale system of linear equations in transmission imaging modality. To We first write Equation (5.19) in an expanded form:

$$\begin{aligned} a_{11}\mu_1 + a_{12}\mu_2 + \cdots + a_{1M}\mu_M &\approx g_1 \\ a_{21}\mu_1 + a_{22}\mu_2 + \cdots + a_{2M}\mu_M &\approx g_2 \\ \cdots\cdots\cdots\cdots\cdots\cdots\cdots\cdots & \\ a_{N1}\mu_1 + a_{N2}\mu_2 + \cdots + a_{NM}\mu_M &\approx g_N \end{aligned} \tag{6.50}$$

Under ideal conditions, such simultaneous equations could be solved exactly by matrix inversion. However, such a direct matrix inversion approach is not feasible due to the following facts [25]:

- The numbers of *M* and *N* are prohibitively large.
- A unique solution will not exist if the equations are under-determined ($N < M$).
- No solution may exist when $N > M$, and $\{g_i\}$ are corrupted by noise.

In such circumstance, SART is applied to solve these equations without direct matrix inversion. To implement such a method, one can first make the initial guess at the solution. This initial guess, denoted by $\hat{\mu}_1^{(0)}, \hat{\mu}_2^{(0)}, \cdots, \hat{\mu}_M^{(0)}$, is represented by the vector $\hat{\boldsymbol{\mu}}^{(0)}$ in the *M*-dimensional space.

In most cases, one can simply set all the initial to be a constant. This initial guess is forward-projected to calculate the estimated line integral, Then we calculate differences between the estimated line integral and measured line integral from Equation (5.16). We apply backprojection to these projection differences and update the initial estimation $\hat{\boldsymbol{\mu}}^{(0)}$, giving the result $\hat{\boldsymbol{\mu}}^{(1)}$ for this loop. For the next loop, $\hat{\boldsymbol{\mu}}^{(1)}$ is the starting estimate to the another estimate $\hat{\boldsymbol{\mu}}^{(2)}$. We keep calculating the estimate iteratively until we approach the true object closely. The update function for the *k*th loop can be expressed as,

$$\hat{\mu}_j^{(k+1)} = \hat{\mu}_j^{(k)} + \frac{\lambda}{\sum_{i=1}^{N} a_{ij}} \sum_{i=1}^{M} \left(a_{ij} \frac{g_i - \sum_{j=1}^{M} a_{ij} \hat{\mu}_j^{(k)}}{\sum_{j=1}^{M} a_{ij}} \right) \tag{6.51}$$

where $\hat{\mu}_j^{(k)}$ is the *j*th element of estimated object at *k*th iteration ($k = 1, 2, \cdots$) and λ is a relaxation factor ranged over (0,2]. Thus, SART converges to a least squares solution which can be very noisy for severely ill-posed inverse problem such as limited-angle tomosynthetic reconstruction [95]. The derivation can be found in [96, 97]. From the Equation (6.51), the value update of each voxel is mainly composed of one forward-projection and one back-projection operation. As mentioned above, the system matrix for DBT system is computed on the fly because of the extremely large size. It take for while to finish one iteration loop calculation. It might take several iterative calculations (70-100 iterations) when the estimate is estimation is close to the true object. Thus, the computation burden of SART in DBT system is pretty much heavy.

In order to accelerate the speed of the estimation approaching to the true object, people propose the order-subset (OS) version of SART. The basic idea of OS is that, with the lexicographic indexing, we divide the whole projection data $\{g_i, i = 1, \cdots, M\}$ into L disjoint subsets. Each sub-group is denoted as $\{g_i, \forall i \in S_l\}$ with $l = 1, \cdots, L$, where S_l is index set for *l*th sub-group, $\bigcup_{l=1}^{L} S_l = \{i = 1, \cdots, M\}$. Usually, we divide the sub groups based on the projection angles. For example, for a DBT system, we have *T* projection images and we subdivide these projection into *L* ordered different sub-groups. Thus, each sub-group contains projection images with t/L angles. For each update for the estimation, the forward- and back- projection

operations in SART algorithm are performed over one sub-group of projections rather than over the whole projections. Therefore, one iteration is composed of L updates over each sub-group, each one sub-iteration update. Let $\hat{\mu}_j^{(k,l)}$ denote the estimated linear attenuation estimation of the jth element for the end of kth iteration and lth sub-iteration. With these definitions, the initial estimate for the next iteration loop is equal to the final updated values at current iteration as follows:

$$\hat{\mu}_j^{(k+1,1)} = \hat{\mu}_j^{(k,L+1)} \tag{6.52}$$

where $\hat{\mu}_j^{(k,L+1)}$ means the estimation when the kth iteration and lth sub-iteration calculation are done.

We can apply the idea of OS to SART by two different ways [97]. The first version of OS-SART can be expressed as,

$$\hat{\mu}_j^{(k,l+1)} = \hat{\mu}_j^{(k,l)} + \frac{\lambda}{\sum_{i'=1}^{N} a_{i'j}} \sum_{i \in S_l} \left(a_{ij} \frac{g_i - \sum_{j=1}^{M} a_{ij} \hat{\mu}_j^{(k,l)}}{\sum_{j=1}^{M} a_{ij}} \right) \tag{6.53}$$

The second version of OS-SART is,

$$\hat{\mu}_j^{(k,l+1)} = \hat{\mu}_j^{(k,l)} + \frac{\lambda}{\sum_{i' \in S_k} a_{i'j}} \sum_{i \in S_l} \left(a_{ij} \frac{g_i - \sum_{j=1}^{M} a_{ij} \hat{\mu}_j^{(k,l)}}{\sum_{j=1}^{M} a_{ij}} \right) \tag{6.54}$$

Similarly, the range for λ is still over (0,2]. Typically, $\sum_{i'=1}^{N} a_{i'j} > \sum_{i' \in S_k} a_{i'j} > 0$, hence the update for the current estimation, $\hat{\mu}_j^{(k,l)}$ in the second OS-SART is greater than one in the first OS-SART. So, you can get a reasonable estimation from the second with less iteration than from the first OS-SART. But, the first version OS-SART is already proved to be to converge [98], while the convergence of the second version OS-SART is still a mystery [97]. Here, we want to emphasize that, in DBT system, the convergence property is not so important to us. Because, limited projection angle range in DBT system provides less known projection information $\{g_i, i = 1, \cdots, N\}$ comparing with the number of unknown object elements $\{f_j, j = 1, \cdots, M\}$ in

linear system. Thus, inverse problem is an ill-posed. All we can do is to give a reasonable solution for the matrix inversion. However, considering the prohibitively large scale of system matrix $\mathbf{A}$, the speed of getting a reasonable estimation is more important to us or for clinical trials. Thus, in our thesis, we pick up the second version of OS-SART for our project.

In general, the SART procedure implementation can be summarized as follows:

1. Take an initial guess $\boldsymbol{\mu}^{(0,0)}$.
2. At the *k*th loop and *l*th sub loop, compute the estimated line integrals $\mathbf{g}^{(k,l)}$,
3. Subtract the estimated line integrals $\mathbf{g}^{(k,l)}$ from the actual line integral $\mathbf{g}$.
4. Perform backprojection operation on the difference tem divided by the normalization term over the projection angles which belong to the *l*th sub-group projection images.
5. Update $\hat{\mu}_j^{(k,l)}$ with a normalization and relaxation factor, $\sum_{i' \in S_k} a_{i'j}$.
6. Repeat from step 3 with next new sub iteration until all *L* sub-groups are used.
7. Repeat from 2 with next new iteration or stop with a reasonable estimate.

5.4 Poisson Nature of Transmitted Photons

We shall prove that the item e_i, the photons passing though the object without scattering, still follows a Poisson distribution. The Photons emitted along the *i*th ray follow a Poisson distribution,

$$\Pr[b_i = n] = \frac{1}{n!} e^{-\bar{b}_i} \bar{b}_i^n. \tag{5.55}$$

Each of b_i may either pass unaffected to the detector along the line or may interact with the object (attenuated or scattered) with the probability *p*. These are Bernoulli trials since the photons interact independently. From the Beer's law in Equation (5.7), we know that the probability of *p* of surviving passage along the *i*th ray using the discrete line integral expression is given by,

$$p = \exp\left(-[\mathbf{A}\boldsymbol{\mu}]_i\right). \tag{5.56}$$

The probability of number of photons e_i can be expressed as,

$$\Pr[e_i = m \mid b_i = n] = \binom{n}{m} p^m (1-p)^{n-m},\ m = 0,\ldots,n. \tag{5.57}$$

Using the property of total probability, we get,

$$\begin{aligned}
\Pr[e_i = m] &= \sum_n \Pr[e_i = m \mid b_i = n] \Pr[b_i = n] \\
&= \binom{n}{m} p^m (1-p)^{n-m} \frac{1}{n!} e^{-\bar{b}_i} \bar{b}_i^n \\
&= \frac{1}{m!} e^{-\bar{b}_i p} (\bar{b}_i p)^m \\
&= \frac{1}{m!} e^{-\bar{b}_i \exp(-[\mathbf{A}\boldsymbol{\mu}]_i)} \left(\bar{b}_i \exp\left(-[\mathbf{A}\boldsymbol{\mu}]_i\right)\right)^m
\end{aligned}$$

Therefore, the distribution of photons that survive passage is also Poisson with mean $E[e_i] = \bar{b}_i \exp\left(-[\mathbf{A}\boldsymbol{\mu}]_i\right)$.

5.5 Comment on Equation (5.23)

If we put the Eq (6.24), with the relation $r = h \cdot \cos\theta$ into the Equation (6.23), we can get

$$S_{\text{Sta}}(v,\theta) = \int_{-\infty}^{+\infty} P_{\text{Iso}}(h \cdot \cos\theta, \theta) e^{-j2\pi hv} dh \tag{5.58}$$

With new variables $r = h \cdot \cos\theta$ and $\omega_r = v / \cos\theta$, we have,

$$S_{\text{Sta}}(v,\theta) = \frac{1}{\cos\theta} \int_{-\infty}^{+\infty} P_{\text{Iso}}(r,\theta) e^{-j2\pi\omega_r r} dr \tag{5.59}$$

The integral part of Eq (A2) is isocentric Fourier slices,

$$S_{\text{Iso}}(\omega_r,\theta) = \int_{-\infty}^{+\infty} P_{\text{Iso}}(r,\theta) e^{-j2\pi\omega_r r} dr \tag{5.60}$$

From the central slice theorem, we know that ω_r is radial frequency in the spatial frequency domain. Recalling the relation between the polar and Cartesian coordinate, we have,

$$v = \omega_r \cos\theta = \omega_x \tag{5.61}$$

Put Eq (A3) into Eq (A2), we can prove ,

$$\begin{aligned} S_{\text{Iso}}(\omega_r, \theta) &= S_{\text{Sta}}(\omega_x, \theta) \cdot \cos\theta \\ \text{with } \omega_x &= \omega_r \cdot \cos\theta \quad \text{and} \quad \omega_z = \omega_x \tan\theta \end{aligned} \tag{5.62}$$

Thus, in the Fourier domain, we can say that $S_{\text{Sta}}(v, \theta)$ is the projection of the $S_{\text{Iso}}(\omega_r, \theta)$ onto the ω_x axis in the spatial frequency domain with a scaling 1/cosθ and ω_r is the radial frequency.

Chapter 6

Impact of Subtraction and Reconstruction Strategies on Dual-Energy Contrast Enhanced Breast Tomosynthesis with interleaved Acquisition

This chapter is paraphrase of a conference paper [99] on which I was first author and did most of the work. (I note that this paper was awarded an honorable mention in the section of the SPIE Medical Imaging Conference where it is presented. My co-worker Yihuan Lu helped with the acquisitions.

6.1 Introduction

Contrast Enhanced Digital Breast Tomosynthesis (CE-DBT) is clinically useful [73]. It retains the 3D advantages of DBT over conventional digital mammography and allows for enhanced display of structures including masses and vasculature. It does so by cancelling background variations in tissue attenuation so that the iodinated structures are more easily seen. A relevant image quality metric to measure performance is SDNR (signal-difference-to noise ratio). CE-DBT may find its usefulness as a screening tool, where the total dose is the same as that of a conventional DBT scan. Alternatively, it could be used as a higher dose diagnostic tool following a suspicious finding from a screening conventional mammographic scan. IN this paper we constrain CE-DBT acquisition to a dose equal that of conventional DBT with is itself equal to that of conventional mammography. Like breast MR, CE-DBT can characterize the contrast agent uptake kinetics of a tumor but it displays anatomy at a higher spatial resolution than breast MR. In this chapter, we are not concerned ith contrast kinetics, but with obtaining high SDNR values at a single time point

In DBT, CE strategies to cancel tissue background and highlight iodinated structures include temporal subtraction (TS) and dual-energy (DE) imaging. Both TS and DE have problems in the propagation of artifacts into the reconstruction, but here we focus on DE-DBT.

In DE-DBT, contrast injection is followed by a high energy (HE) acquisition (above the iodine K-edge) and a low energy (LE) acquisition. As shown in Figure 6.1 (b), DE-DBT can be done by a "two sweep" acquisition protocol. However, there are important advantages in instead doing a one-sweep "interleaved" acquisition (Figure 6.1 (c) and (d)) in which a HE acquisition at one angle alternates with a LE acquisition at the next angle while the X-ray tube sweeps through its arc. Advantages of interleave vs. two-sweep acquisitions [74] include (1) less artifacts due to patient motion (2) less patient time spent under uncomfortable compression. Due to these advantages, our work focuses on the interleaved acquisition protocols in Figure 6.1 (c) (d). Figure 6.1 summarizes acquisition and processing of conventional DBT, double-sweep DE-DBT, and two ways of doing interleaved DE-DBT.

6.2 Experimental Methods

We presume that for all the acquisition protocols of 6.1, the X-ray tube is swept continuously (not in step-and-shoot mode), and the kV and filter switching is fast enough for the interleave schemes. The sweep times are all equal, so the double-sweep method of Figure 6.1 (b) takes at least twice as long as the other cases. All acquisitions are presumed to be acquired at a dose equal to that of the screening DBT case of Figure 6.1 (a). In this case, the dose from each interleave exposure at a given angle is twice that of an exposure from the same angle in the double-sweep method. Angles are equispaced by $\Delta\theta$. For clarity, only 6 angles are shown though our acquisitions will use more. We note that if a step-and-shoot mode is possible, then the HE and LE acquisitions in the interleave scans can be acquired with $\Delta\theta = 0$, and if a photon-counting detector is used, HE and LE acquisitions could be acquired simultaneously. But here, we exclude these two possibilities.

Conventional data processing for DE-DBT is shown in Figure 6. 1(b) and (c). This entails a weighted subtraction of HE and LE projection data followed by reconstruction of the subtracted data. Subtraction, designed to remove anatomical background variability from the CE reconstruction, can create artifacts due to patient motion. The interleave scheme of Figure 6.1 (c) is less susceptible to patient motion artifacts than the double-sweep method. However, this interleave method incurs a subtraction artifact *even in the absence of patient motion*. Since the angular difference $\Delta\theta$ in the interleaved HE, LE acquisitions creates a shift in the associated

image pairs, and weighted subtraction of the shifted image pairs creates artifacts that can propagate into the reconstruction and thus lower image quality. We shall refer to the scheme in Figure 6.1 (c) as "subtract/recon" or SR.

We propose to reduce these types of artifacts by the alternate strategy of first reconstructing the HE and LE data separately and then subtracting the reconstructions as shown in Figure 6.1 (d). We call this the RS (reconstruct-then-subtract) strategy. The actual reconstruction algorithm can also affect the propagation of subtraction artifacts, and we explore the effects of FBP and SART on SDNR. The algorithms can be used in an SR context or an RS context.

Our purpose is to explore the effects on lesion SDNR of six acquisition and processing cases. Let DS mean double-sweep and IL mean interleave. As defined previously, RS and SR refer to the reconstruct-then-subtract and subtract-then-reconstruct strategies. The six cases are then: DS-SR-FBP, IL-SR-FBP, IL-RS-FBP, DS-SR-SART, IL-SR-SART and IL-RS-SART.

Note that our focus here is in the effects on lesion SDNR of subtraction artifacts in the presence of background variability under the 6 acquisitions. Many other factors can affect lesion SDNR, such as contrast kinetics during acquisition, spectrum tailoring, detector characteristics and other factors, but our work here does not consider these. Also, we do not model patient motion in this study even though we have pointed out that interleave acquisition is less susceptible to patient motion artifacts than double sweep acquisitions.

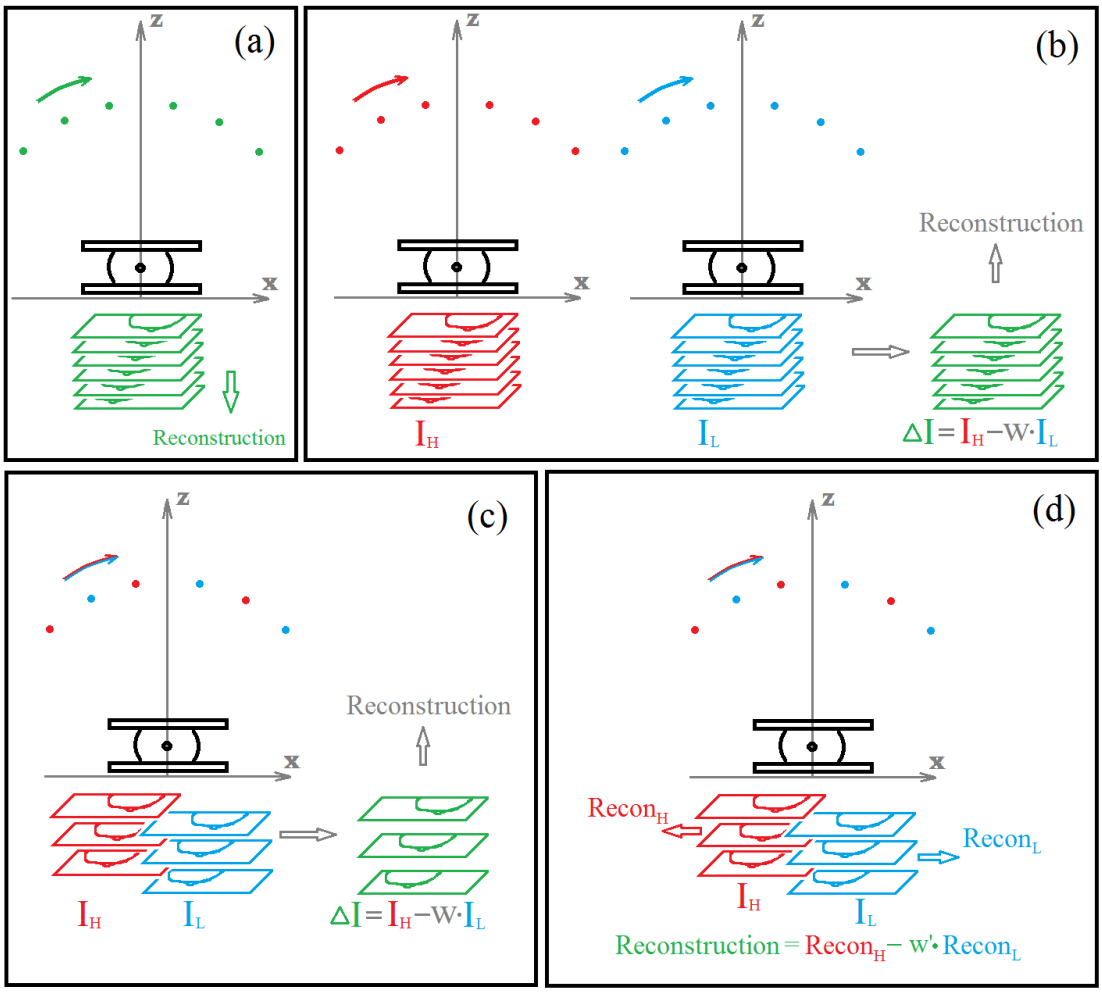

Figure 6.1. Acquisition protocols. (The 3D acquisition and processing takes place in the X-Y-Z space, but for clarity we do not display the Y-axis.) A compressed breast is shown in the X-Z plane and the detector assumed coincident with the X-Y plane. The sketch is not meant to be to scale. Dots indicate source positions. (Discrete dots imply a step-and-shoot acquisition, but in experiments we use continuous tube motion.) For clarity, only 6 source positions are depicted. A green dot is for conventional DBT kV, red for HE kV and blue for LE kV acquisitions. The stacks of rectangles indicate the projection data (after the log step). "Reconstruction" indicates the application of a reconstruction algorithm to the projection data. (a) Conventional DBT (b) Double-sweep DE-DBT. Here the ΔI is the weighted subtraction, with weight w, of projection data $\Delta I = I_H - w \cdot I_L$ which is then reconstructed (c) Interleaved CE-DBT with weighted subtraction of adjacent scans followed by reconstruction. The vertical offset between the stacks of I_H and I_L projections indicates that associated I_H and I_L pairs are obtained from slightly different angles and are therefore laterally shifted in the x-direction. (d) Interleaved CE-DBT with separate reconstruction of HE, LE data denoted by $Recon_H$ and $Recon_L$. This is followed by weighted subtraction, with weight w', in the reconstruction domain.

Figure 6.2. The Siemens Mammomat Inspiration DBT unit is shown with the phantom situated for acquisition. The compression paddle sits atop the phantom, and the phantom sits directly atop the carbon-fiber detector cover. The inset shows the slab of the phantom with the iodine inserts. The gantry is shown at its extreme angle of 25 degrees.

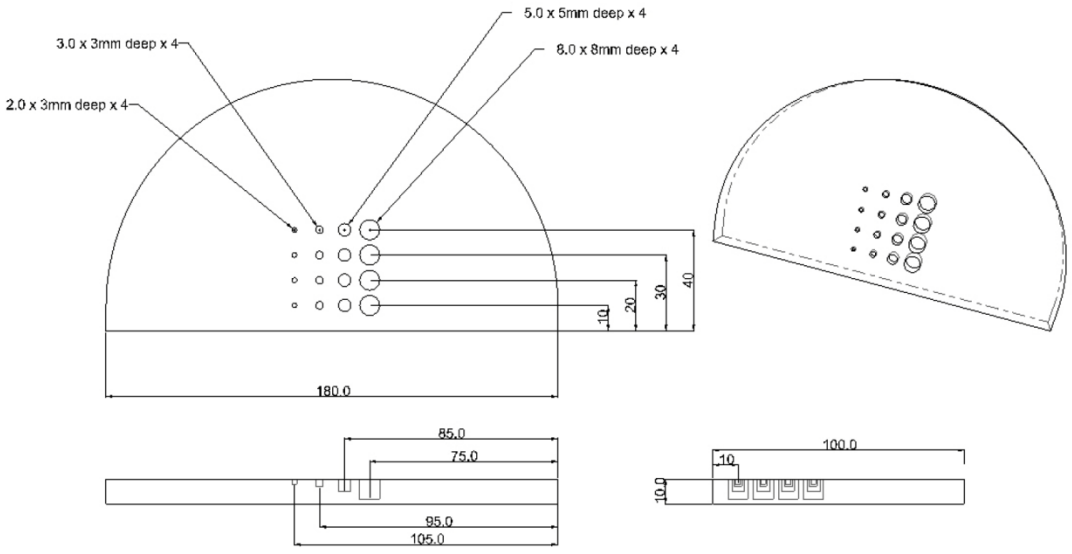

Figure 6.3. Geometry of the iodine inserts. All dimensions are in mm.

6.2.1 Phantom

We acquired phantom images on a prototype Siemens Mammomat Inspiration DBT unit. Figure 6.2 shows the phantom as it is situated in the scanner. The phantom (Figure 6.2) comprised four 1 cm thick semi-circular CIRS model 20 layers designed to mimic the spatial variability of adipose and glandular tissue and the phantom was designed to include 50% adipose and 50% glandular. The 3rd slab (inset in Figure 6.2) was modified to include a 4 by 4 contrast-detail array of cylinders filled with solid iodine inserts. Figure 6.3 shows the insert geometry. The cylinders in each column are 2, 3, 5 and 8 mm in diameter with the depth of each cylinder equal to its height. The tops of all 16 cylinders lie in one plane, and it is this reference plane which we will use for in-plane SDNR evaluation. The iodine concentration in each row is (top to bottom) 1, 2, 3 and 5 mg/ml.

6.2.2 Acquisition details

Since our DBT unit could not acquire data in interleave mode, we used double-sweep acquisitions to obtain both DS data (Figure 6.1 b) and IL data (Figure 6.1 c and d). We did this in the following way: To get DS data, we did two sweeps at 71 mAs (H) and 71 mAs (L) and kept all projection data. To get IL data, we did two sweeps at 140 mAs (HE) and 140 mAs (LE) and then culled alternate projections to obtain HE, LE pairs as shown in Figure 6.1 c and d. The resulting interleaved acquisition comprised 12 HE acquisitions and 12 LE acquisitions spanning $-25°$ to $+22°$ with an angular separation of $\Delta\theta = 2°$. The DS acquisitions comprised 24 HE and 24 LE acquisitions each spanning the same $-25°$ to $+22°$ angular range. The tube motion was continuous with an X-ray duty cycle (% of $\Delta\theta$ during which X-rays are generated) of 4.5% for DS and 9% for IL. Because of the small duty cycle the motion blur was negligible. The effective total interleave sweep time was 30 sec and the effective DS sweep time (2 sweeps) was 60 sec. The a-Se detector had a 300 μm thickness and 85 μm detector bin pitch with no bin averaging on readout. For HE, we used a target/filter W/Cu at 49 kV and for LE W/Rh at 28 kV. The acquisition leads to about a 50%/50% dose split for HE/LE. The total dose, 1.4mGy for any acquisition, was comparable to that of a conventional DBT screening acquisition. The projection data were corrected for detector gain nonuniformity and for shading due to radiometric effects and the heel effect. No correction of the reconstruction due to scatter was done.

6.2.3 Reconstruction algorithms

For the FBP reconstruction [90] we applied a ramp filter in the X-direction and modified the ramp with a Hamming apodization filter with a cutoff frequency of 0.75 of the Nyquist. A Hamming slice thickness filter to control Z direction aliasing is also applied in the Z direction with a 0.035 Nyquist cutoff. For a stationary detector geometry, the various filter cutoffs depend on θ as described in [74]. We used an ordered-subset version of SART [100] with 4 iterations and a constant image as the initial condition. For both FBP and SART, we applied a final median window filtering to the reconstruction, using a 5 by 5 pixel window. The rectanguloid reconstruction voxels had dimensions $85 \times 85 \times 1000$ μm. For reconstructions, we used a ray-driven Siddon-based forward projector [84] and a voxel-driven backprojector based on bin interpolation. The reconstruction programs were implemented using a graphics processing unit (GPU) which resulted in high-performance computing in both FBP and iterative SART reconstruction. The average speedup factor was over 100 relative to a traditional CPU implementation.

6.2.4 Data processing strategies

Let I_H and I_L represent the interleaved projection data after the log step (as in Figure 6.1 c and d). Let $\hat{\mu}$ denote a reconstructed image. Let Φ denote a reconstruction operator (SART or FBP). Then the SR strategy of Figure 6.1 (c) can be summarized as $\Delta I = I_H - wI_L$ followed by $\hat{\mu}_{SR} = \Phi(\Delta I)$. The weight w = 0.3 was determined using methods in [81]. For the RS strategy, we first perform two reconstructions $\hat{\mu}_H = \Phi(I_H)$ and $\hat{\mu}_L = \Phi(I_L)$. Then $\hat{\mu}_{RS} = \hat{\mu}_H - w'\hat{\mu}_L$ completes the RS strategy. We used w' = 0.2 derived empirically. In [99] a form of RS was used with Φ = simple backprojection and a post-filter applied to the result. For the DS data processing (Figure 6.1 b), I_H and I_L denote the double-sweep (non-interleave) projection data. Again $\Delta I = I_H - wI_L$ with w = 0.3 and $\hat{\mu}_{SR} = \Phi(\Delta I)$.

The RS and SR strategies are characterized by an important difference. For the reconstructions in RS, each of the HE and LE detector values are backprojected along the directions from which they were acquired. But for SR, a given detector bin contains contributions from an HE ray and an LE ray each separated by $\Delta\theta$. Therefore, there is an ambiguity in the proper direction to be used for backprojection. One could backproject along the

HE ray or the associated LE ray of the interleaved pair, or at some average angle. In our reconstructions we backprojected along the HE direction.

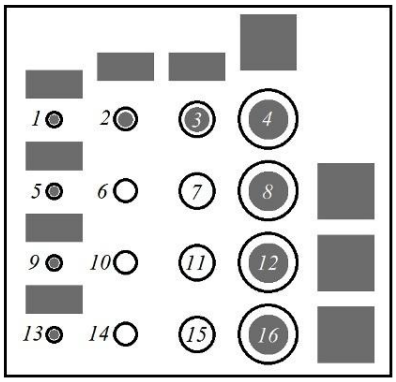

Figure 6.4. The numbers in each circle index the signal. The circular grey regions (70% of signal radius) are signal templates used in SDNR and the adjacent square and rectangular grey regions are the associated background regions used in SDNR calculation.

6.2.5 SDNR calculation

SDNR was calculated for each of the 6 cases mentioned in Section 2.1 and for 10 of the 16 signals of the 4 by 4 contrast-detail phantom. SDNR was evaluated in a reference plane containing the tops of all cylinders as seen in the lower left of Figure 6.3. SDNR was defined as the (mean signal - mean background) / (standard deviation of background) in a manner similar to [89, 101]. Note that fluctuations due to the propagation of subtraction artifacts are an important contributor to the means and standard deviation in the SDNR definition. Figure 6.4 shows the circular signal templates and square background templates used in SDNR calculations. Signals 6, 7, 10, 11, 14 and 15 were not evaluated due to lack of space for fitting a background template. Signals 1, 5, 9 and 13 were evaluated, but we note that the very small diameter of these four signals led to less reliable SDNR values.

Table 6.1. SDNR for each of the 6 acquisition-reconstruction combinations. The signals corresponding to each signal index are shown in Figure 6.4. DS = double sweep and IL = interleave

Signal index	DS-SR-FBP	IL-SR-FBP	IL-RS-FBP	DS-SR-SART	IL-SR-SART	IL-RS-SART
1	1.159	1.641	1.187	1.491	2.682	2.747
2	1.165	-0.188	0.583	1.388	-0.017	1.697
3	0.855	0.658	0.885	1.407	1.323	2.177
4	1.198	0.545	0.971	2.014	1.313	2.247
5	2.420	2.572	2.363	2.388	3.088	4.207
8	1.656	0.604	1.173	2.474	1.656	3.135
9	2.666	2.384	2.752	3.427	3.788	5.399
12	2.144	0.911	1.992	2.542	1.528	4.233
13	3.318	1.581	3.667	3.848	2.289	7.021
16	2.584	1.187	3.118	3.280	2.147	5.358

6.3 Results and Conclusions

Figure 6.5 shows reconstructions in the reference plane. Note that the subtraction artifacts, striations in the interleaved reconstructions indicating incomplete background removal, are more apparent for the SR cases in Figure 6.5 (b) and (f) than in the RS cases of Figure 6.5 (c) and (g).

Table 6.1 summarizes quantitative SDNR results. One observation illustrated in the table and figure is the following: (1) For our proposed interleave protocol, and for both FBP and SART, the RS method yields superior results relative to the SR method. A second observation is that (2) for projection data collected under any protocol, the SART reconstruction yields better SDNR than FBP. A third observation is that (3) in comparing any DS result to any IL result, there is no consistent superiority of one method vs. the other. However, the particular case of IL-RS-SART is far superior to any DS result. Note that the SDNRs for signal 2 in the IL-SR-FBP and IL-SR-SART cases are negative. This is due to the fact that signal 2 is of small diameter with a small averaging template, so very few pixels are used to calculate signal difference. In this case, the few noisy pixels in the signal-absent case were of higher intensity on average than those of the signal-present case. Here "noise" is mainly to the propagation of subtraction artifacts, not quantum noise.

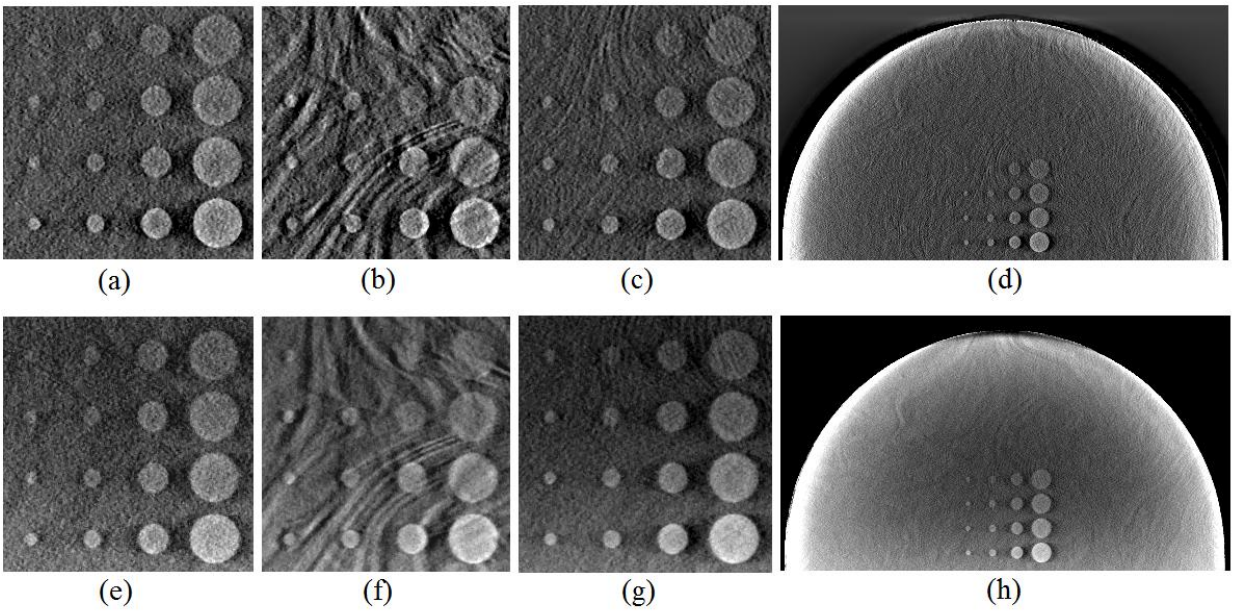

Figure 6.5. Reconstructions in the reference plane. (a) DS-SR-FBP. (b) IL- SR-FBP. (c) IL-RS-FBP (d) IL-RS-FBP. (e) DS-SR-SART. (f) IL-SR-SART (g) IL-RS-SART (h) IL-RS-SART. (DS=double sweep, IL=interleave, SR=subtract-then-reconstruct, RS=reconstruct-then-subtract) The grey scales for each image here are chosen for viewing convenience, but quantitative image quality is summarized in Table 6.1. The reconstructions show only the signal region, except for (d) and (h) which show the full phantom slice corresponding to (c) and (g).

6.3.1 Discussion

There are strong practical reasons - less susceptibility to patient motion and less patient time spent under compression - to use interleaved acquisition rather than double-sweep acquisition for DE-DBT, but for continuous tube motion, interleaving incurs unavoidable artifacts in the reconstruction even in the absence of patient motion. For interleaved acquisition, reconstruction followed by subtraction (RS) is preferred (in the sense of SDNR) over subtraction followed by reconstruction (SR) for DE-DBT, though the choice of algorithm (SART vs. FBP) has an even stronger effect.

The choice of weight for the RS method depends on the algorithm and we shall pursue a means to determine this. For CE-DBT, SDNR should be linear with iodine content, and we shall verify that this relation holds with interleave acquisition. To do this study of relative quantitation, we need to apply careful correction for scatter. Of course the parameter space for a given algorithm (filters for FBP, relaxation and iteration number for SART) is large and affects image quality, but we will attempt to verify that over a large algorithm parameter space, the RS

(reconstruct-then-subtract) method retains advantages over SR (subtract-then-reconstruct) for dual energy DBT.

Chapter 7

Introduction to Emission tomography

Nuclear medicine imaging is a non-invasive modality for the study of dynamic body functions without trauma to patients [102]. Usually, a radiopharmaceutical labeled with a radionuclide, e.g. ^{99m}Tc-Sestamibi for SPECT, is administered to the patient to tag a specific biochemical function with regards to a specific target organ [103]. Gamma-ray emanations from these radionuclide will hit a area radiation detector and their counts and positions on the area are estimated. From this information, one may reconstruct a 3D map of the radiopharmaceutical density in the body for a physician review.

Here, we give a brief introduction to the SPECT imaging process. During a scan, these injected radionuclide atoms of the radiopharmaceutical emit gamma photons having sufficient energy to penetrate human body tissue in significant numbers. Most of these penetrated photons will be recorded by a gamma ray detector. One of widely used detector called Anger camera [104] has a large scintillator layer composed of NaI (thallium-doped sodium iodide) crystal preceding an array of photomultiplier tubes (PMTs). Actually, these photons can hit the detector in a specific direction. This specific direction is decided by a collimator put above the detector. Usually, the collimator is a thick sheet of heavy metal (e.g. lead) perforated like a honeycomb by long thick channels. Thus, the collimator will absorb photons travelling in directions other than those roughly perpendicular to the collimator. When a photon hits the detector, it first interacts with the NaI crystal and ionizes NaI atoms within the crystal causing visibly optical photons. Then these visible light is collected by the array of PMTs and an electronic circuit estimates the location of interaction within the scintillator layer. A histogram of incident photons binned with respect to their estimated hitting position on the detector constitutes a single 2D planar image known as projection [103]. It is a projection in the sense that it is a 2D line integral of a 3D object. The "object" is the 3D distribution of the radiopharmaceutical. This 2D image contains *in vivo* distribution information of radiopharmaceutical. Several such 2D images acquired at different position of the detector form the data used in emission tomography. By tomographic reconstruction, an 3D map of the radiopharmaceutical density within the patient can be digitally reconstructed with these 2D images.

7.1 Basic Principles of SPECT

7.1.1 Planar Imaging

We first describe conventional planar imaging. The 3D distribution of radiopharmaceutical within the patient body is imaged onto a 2D projection image given a detector at one position. The gamma photons emitted by internally distributed radionuclide can penetrate through the patient's body. During the penetration, these photons interact with body tissue and might get absorbed or scattered. There are two main interaction effects, photoelectric effect and Compton scattering, given the photon energy range for clinical SPECT. Those photons passing through the body are used to obtain a projection image.

Radionuclide emits gamma photons along all directions. Since a gamma photon has a high energy (small wave length) and no electric charge, we cannot confine the direction of these photons by lenses or electromagnetic field. In SPECT, we use a collimator with a lot of apertures to confine gamma photons. The collimator will be put above the detector. Collimators are usually made of a plate of heavy metal with high atomic number like lead or tungsten which can absorb the photons effectively. There are different designs of collimator. In this thesis, we mainly focus on one type of collimator whose apertures are parallel to each other and has hexagonal hole shape. Thus, these parallel hole collimator can confine incident photons to directions approximately perpendicular to the detector face as Figure 7.1 shows. The figure also gives various parameters of the collimator such as bore length (l_c), bore diameter (d_c), and septal thickness.

The collimated photons hit the scintillation layer (NaI) of the detector first. During the interaction with scintillation layer, some of the photon energy is deposited by ionizing NaI atoms. Such deposited energy is converted to visible photons. The intensity of the visible light flush is proportional to the energy of the incident photon. The scintillation light is guided toward to several photocathode of PMT's coupled to the crystal. Each PMT transfers these visible light flush to current signals proportional to the amount of light impinging on it and output these signals to the preamplifier circuit. A digital pulse-position analysis circuit estimates the position of the scintillation event based on current pulses from various PMT's. This is then discredited to give a quantized position on the camera face, known as "bin". The current pulses from various

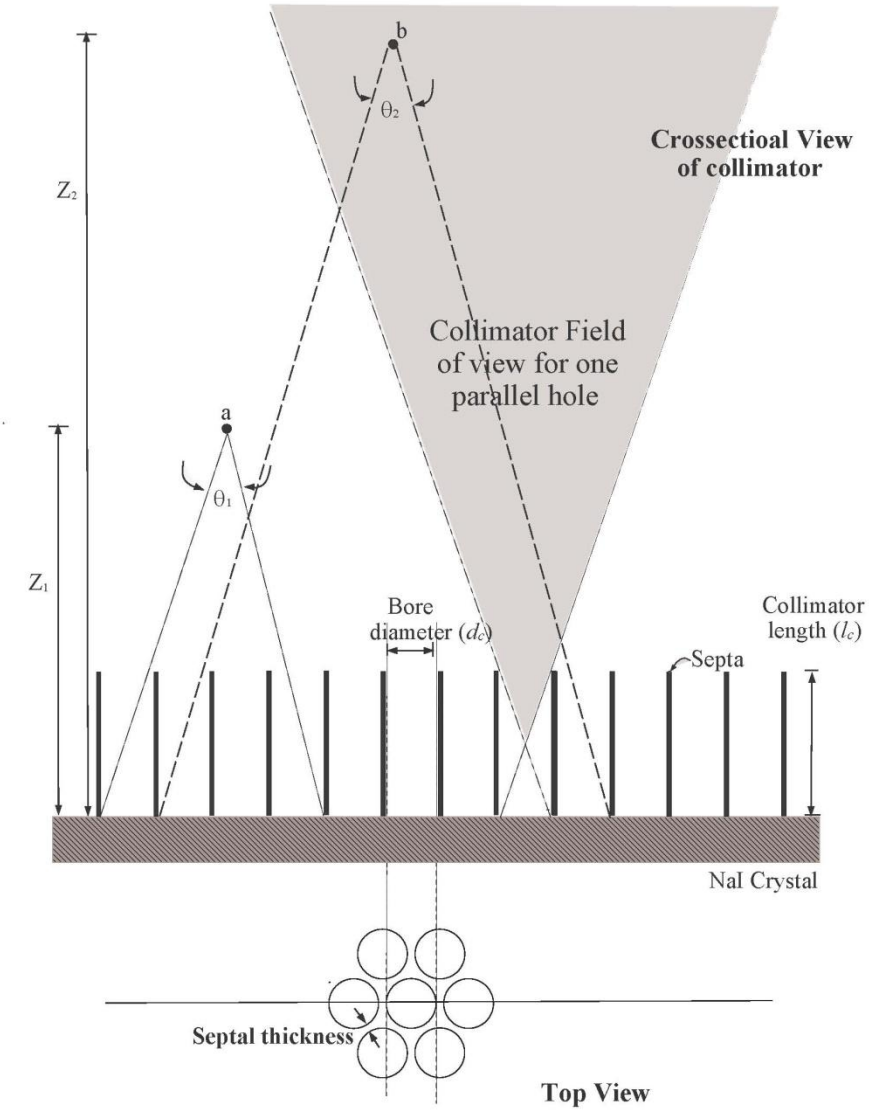

Figure 7.1: Basics of a parallel-hole collimator geometry: The hexagonal array in the bottom part of the figure is the top view of a few bores of a typical collimator. A cross-sectional view through the center of the hexagonal array is shown in the top part of the figure. The figure is not to scale relative to a clinically used collimator. The photons emitted form point "a" spread over a smaller area of the crystals as compared to photons emitted from point "b". The acceptable angle of photon rays are limited by the collimator (θ_1 for the point "a" and θ_2 for the point "b"). The shaded area illustrates the field of view for one bore. To a good approximation, only photons emitted from locations within this field of view can be detected.

PMT's are combined to a net signal. The height of the combined signal gives an estimate of energy of the detected photon since it is proportional to the deposited energy in the scintillation layer. However, there is an uncertainty in the estimate of energy of detected photon due to the uncertainty in numbers of optical photons generated in the scintillation layer and several stochastic processes for the transfer from optical photons to the combined current pulse. Also, imperfections in the detector will introduce extra uncertainties. Thus, only events within a certain energy range (corresponding to uncertainty in the energy estimation procedure) of known radionuclide energy result in a unit increment of a memory location specific to the quantized location of each hitting event. The array of resulting counts of gamma ray photons, displayed as 2D image, know as projection or planar image. The readout of each detector bin follows the independent Poisson distribution as we will describe in Chapter 8.

7.1.2 SPECT as Tomography

The goal of quantitative SPECT is to obtain an accurate 3D image of the radioactivity distribution in the region of interest in the human body. The emitted photons get collimated and only those whose direction is nearly perpendicular to the detector get accepted. From the Figure 7.2, we can see that any photon moving in the direction of line segment AB will be recorded by the detector at the point 'O'. Consequently all photons emitted for the 2D cross-section containing AB and moving along the direction of AB will be summed and recorded as a 1D projection profile in the camera face. Following the same scheme, a 3D source object stacked with several 2D cross-sections along *z*-axis will be imaged as a stack of 1D projection files on the camera face. Hence, an entire 3D radiotracer density can be projected onto the camera face as a 2D projection image. Since every point on the 2D projection image accumulates the radioactivity along an approximately normal line to the camera face, any information of depth through the 3D radiotracer distribution is lost. Hence the underling and overlying structures in a 3D object are compressed into a 2D planar image. In tomography, one acquires different projection views at different projection angles around the object [83]. By combining these 2D projection views mathematically, the 3D structure of the object can be estimated, or a 2D structure from many 1D projections. In clinical SPECT, the camera is rotated around the patient to get 2D planar images (projections) at various angles, e.g. 60 angle samples. The gamma detector is designed to rotate up to 360^o around the patient. These projection angles are equidistantly distributed over 360^o. For

each angle, the detector camera with the collimator will stop and collect photons. The total scan time is equal to data acquisition time multiplying the number of angles. Typical scan time is around 20 minutes for brain imaging [2] and 20-30 minutes for ventilation and perfusion studies [2]. Once these projection data is collected, a reconstruction will be applied to these data to estimate the radioactivity distribution through a computer system.

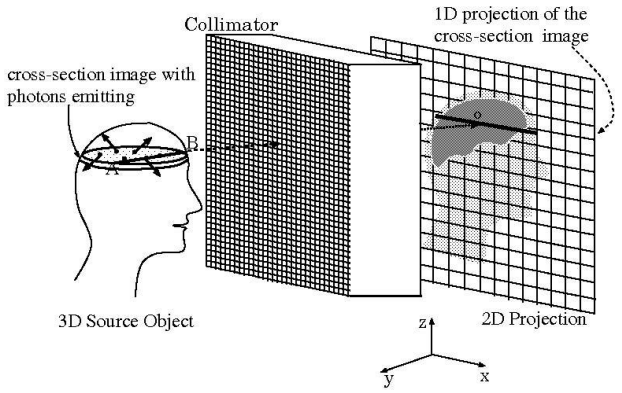

Figure 7.2: A 2D projection from a 3D object. The line AB on a cross-section (slice) is pictured to be a projection at point "o". A slice perpendicular to the detector plane forms an image along one line (1D projection profile). Stacking 1D projections of slices together forms a 2D projection of a 3D object.

Figure 7.3 illustrates the basic principle of operation of a 2D SPECT system, i.e., only one cross-section of an object is studied. The 1D camera is shown at many angular position θ_k. A 1D projection is measured at each position. As shown in Figure 7.3, initially, the camera is in position θ_1, photons are collected to bins and the resulting projection profile fills in the first line of the projection data with 1 being its index for angle. Then, the camera is rotated to the next position θ_2. Its projection profile is placed next to the line from θ_1, i.e., fills in the second line of the projection data with angle index 2. Then, camera goes to θ_3 for the third line of the projection. Extending this, the camera covers the full 360^o of the orbit, i.e. completes the collection of photons at K sampling angles in total as shown in the Figure 7.3. All of these projection profiles are thus sequentially stacked to a 2D image with the abscissa being the digitized detector coordinated "bin" and the ordinate being the index of the sample angle. This 2D digital image is referred to as the "sinogram".

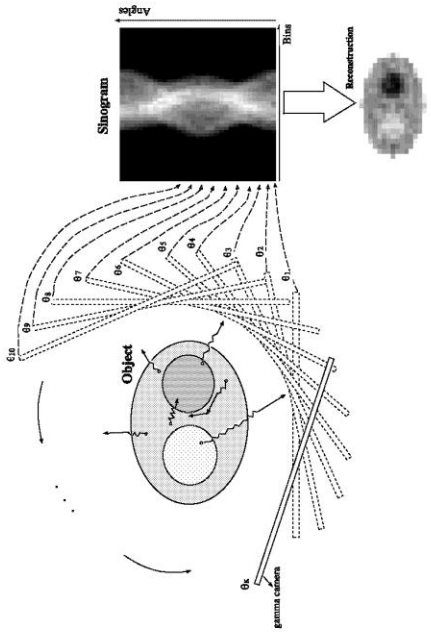

Figure 7.3: The basic principle of SPECT. A gamma camera rotates around the object and acquires many projection views at equidistant angles. These projection views together form a sinogram from which the object is mathematically reconstructed by a reconstruction algorithm.

A typical "sinogram" is shown in Figure 7.3. We can see that the sinogram is itself not visually interpretable by a radiologist. Therefore, before serving diagnostic purpose, another step needs to be proceeded. This step is called reconstruction. A reconstruction algorithm attempts to transform a sinogram to a meaningful estimate of the original radioactivity distribution. The digitized sinogram data is fed to a computer system on which the reconstruction algorithm is executed. The reconstructed digital images are what we present to physicians for diagnostic or therapeutic purposes. the upper right image in Figure 7.3 shows a reconstruction of the data in the upper left sinogram. The above illustration is for obtaining 1D projections from a 2D object, but is easily extended to 2D projections from a 3D object.

7.1.3 Tasks in Nuclear Imaging

Note: We will use the abbreviation "recon" to mean "reconstruction" or "reconstructed". Since the word comes up so often, this abbreviation is very convenient and is often used by others in the field.

Given a radionuclide, the final recon image quality decides if the 3D radiopharmaceutical distribution is estimated well or not. Such image quality is affected by the imaging system and the reconstruction method. In the SPECT imaging system, there is a crucial hardware part, the collimator, which is described by bore diameter, bore length and septal thickness. Given, a collimator material (e.g. lead), the collimator needs to be designed carefully from these three parameters since it will affect the quality of the projection data, thus affecting the recon image quality through a reconstruction method. For the reconstruction part, most algorithms have one or two free parameters that need to be tuned to give a best image according to a specific problem. In order to evaluate the recon image quality, we should be able to evaluate the image quality quantitatively based on a specific figure of merit, or called task based, to make a proper choice of the collimator and recon free parameter. In this thesis, we apply tasked based objective assessment to the recon image quality. The image quality is measured on basis of how well an imaging system including reconstruction method allows an observer to perform a specified task [105].

Tasks can be conveniently divided into quantification and classification. In quantification, one seeks to accurately estimate the value of some scalar parameter of interest e.g. a patient's cardiac ejection fraction (percentage of blood that is pumped out of a filled ventricle with each heartbeat) or the average radio tracer uptake in a particular organ of interest. Classification involves determining to which of two or more categories an image should belong. A decision task is special case in which one decides whether a signal (or a tumor in recon image) with a known location is present or not. Detection is not necessarily a binary decision problem. In reality, we usually search the image and try to find out the signal location if we decide there is a signal in the image. In detection theory, we call this process as detection and localization. Let's say that there is only one signal in the image and it could be located in L positions. Thus, we have L+1 hypothesis (L possible location cases + signal absent case) instead of a binary hypothesis (absent/present). The classifier has to decide whether the observed image contains a signal and if

so which of L signal classes the signal belongs to. In this thesis, we focus on the classification and apply detection and detection-localization tasks to evaluate the image quality.

To get an idea of what a SPECT image looks like and to get a feel for a detection task, examine Figure 7.4. Figure 7.4 (a) shows a "phantom", a mathematical ground truth object with a signal in the lung as indicated by the figure caption. After image simulation and reconstruction, we get the SPECT images in Figure 7.4 (b) and (c). Note how blurry and noisy they are, Figure 7.4 (b) shows the reconstruction without the signal and Figure 7.4 (c) with the signal.

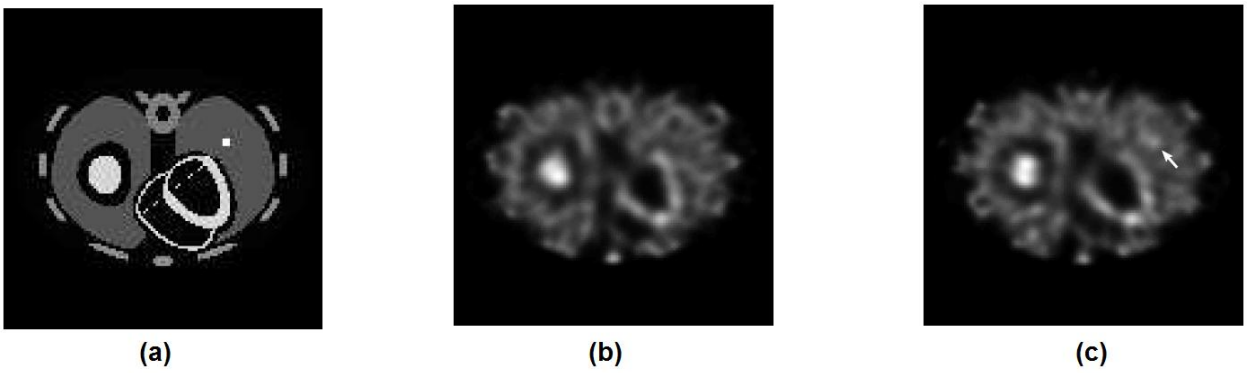

Figure 7.4: Anecdotal reconstruction of (a) a slice of a test object, (b) without lesion (c) with a lesion (marked by arrow). The lesion was a 3×3 lesion of contrast 2:1 with the background.

Image quality is based on performance of an observer with respect to the task. For a task in a clinic, the observer should be a physician. An observer could also be implemented as mathematical operator to save the labor work and evaluation time. As an example, the matched filter is a simple mathematical observer for the case of detection of a signal in uncorrelated Gaussian noise [106].

In this project, we try to optimize both of the imaging hardware (the collimator) and the reconstruction algorithm. The hardware system delivers the raw projection data and the reconstruction algorithm transforms this data into an image for the physician to examine. To quantify the image quality, we need an observer that works on the reconstructed image. Ideally, we would have a human (physician) view a bunch of recon images, typically about hundred images. But optimizing a reconstruction based on the performance of humans is extremely time-consuming. Thus mathematical model observers that emulate human performance [105, 107] are extremely useful. These human emulating model observer can deliver a scalar figure of merit (FOM) for the evaluation of a image quality [108-110]. The uncertainty (noise) in the images as

well as the observer performing the task play vital role in calculating a FOM as a measure of performance.

Chapter 8

SPECT Imaging Model

In this chapter we describe a mathematical model for the formation of projection data in SPECT. It is important to have such model for the SPECT data to address the ensuing inverse problem of image reconstruction.

8.1 Image Formation

First of all, we summarize the notation convention we use in this project. Lower-case letters are used to specify scalar variables and scalar valued functions. Vector and vector-valued functions are represented by lower-case bold letters. For example, $f_n,\ n = 0,1,...,N-1$ are the elements of a N-dimensional vector **f**. Whether a vector or scalar is random or non-random will be clarified from context. A matrix is denoted by an upper-case letter and square brackets with appropriate subscripts is used to denote its element. For example, $\mathcal{H}_{mn}$ or $[\boldsymbol{\mathcal{H}}]_{mn}$ is the mnth element of a $M \times N$ matrix, $\boldsymbol{\mathcal{H}}$. Thus, the mth element of a matrix-vector product $\boldsymbol{\mathcal{H}}\mathbf{f}$ is given by $[\boldsymbol{\mathcal{H}}\mathbf{f}]_m$, where $[\boldsymbol{\mathcal{H}}\mathbf{f}]_m = \sum_{n=1}^{N} \mathcal{H}_{mn} f_n$. We use the superscript T to denote a matrix or vector transpose, so $\mathbf{A}^T$ is the transpose of **A**. Then $\mathbf{a}^T\mathbf{b}$ is an inner product of two vectors **a** and **b**.

Because of the statistical feature of this work, the concepts of means and variances from random variables come up in later chapters. We denote means by the decoration of a bar. For a random variable a and its density function $p(a)$, its mean is defined as,

$$\bar{a} = \int a p(a) da \tag{8.1}$$

and its variance is defined as

$$\sigma_a^2 = \int (a - \bar{a})^2 p(a) da \tag{8.2}$$

Similarly, for a random vector **g** with its probability density, $p(\mathbf{g})$, its mean is denoted by $\bar{\mathbf{g}}$ with each element $\bar{g}_m$ computed as following:

$$\bar{g}_m = \int \cdots \int g_m p(g_1, \cdots g_M) dg_1 \cdots dg_M \tag{8.3}$$

Its covariance matrix denoted as $\mathbf{K}_\mathbf{g}$ with element $[K_\mathbf{g}]_{mn}$:

$$[\mathbf{K}_\mathbf{g}]_{mn} = \int\cdots\int (g_m - \bar{g}_m)(g_n - \bar{g}_n)\, p(g_1, \cdots g_M)\, dg_1 \cdots dg_M \tag{8.4}$$

If the random variable (vector) is discrete, the integration is replaced by summation. Another decoration used is the carat (^). We denote an estimate of a random vector $\mathbf{f}$ by $\hat{\mathbf{f}}$. We can use the angle bracket notation as shorthand, where <...> means take an average using the relevant pdf. Thus, $\bar{\mathbf{f}} = <\mathbf{f}>$, and Equation (8.4) can be written as $\mathbf{K}_\mathbf{g} = <(\mathbf{g}-\bar{\mathbf{g}})(\mathbf{g}-\bar{\mathbf{g}})^T>$.

In SPECT, the entity we want to know is the true 3D spatial density distribution of the radionuclide. It is proportional to the average number of radionuclide disintegrations into 4π steradians per unit volume per unit time of the radionuclide distribution. As we described in Chapter 5, we choose the voxel basis functions to discretize such 3D density distribution. By lexicographic index ordering, introduced in Chapter 5, we can present this multidimensional quantity as a 1D vector **f**. The number of photons emitted from the radionuclide in the *n*th voxel during a finite interval, f_n, is a random quantity and follows a Poisson distribution [57]. The mean number of emissions per unit time is f_n. Thus, the higher the concentration, the more gamma photons will be emitted on average per unit time. Thus, estimating the Poisson means of the 3D emission rates is equivalent to estimating the spatial density distribution of the radionuclide. We term **f** as the "object" and its estimate as the "recon", $\hat{\mathbf{f}}$. A 2D SPECT projection data acquired in the camera face from a 3D object are already in discrete form since each bin contains a positive integer number of photons counts. Similarly, with lexicographic index ordering, we can express the projection data as a vector including all 2D camera readouts over all projection angles. Due to the limited quantity of radiopharmaceutical that can be administered to the patient and the fact that only about1 in 10^4 photons emanating from the object gets collimated then detected, the typical bin counts g_m are of the order 1 to 10. For the camera data, g_m is the integer valued number of counts in a detection bin indexed by *m*. The index *m* runs over all camera bins at a given angle and over all angles. Thus the entire multidimensional camera data set is represented by a vector **g**. Since **f** is noisy, each g_m is noisy as will be described below.

Photons are emitted into 4π steradians. The probability that a photon emitted from the object would be detected is dependent on emitting location, the voxel f_n, relative to the detector bin *m* and other factors of the imaging system. One important geometric factor governing this acceptance probability is the geometry of the collimator. We denote this probability as $\mathcal{H}_{mn}$. The quantity $\mathcal{H}_{mn}$ is the Bernoulli probability that a photon emitted from a voxel *m* in the object is detected at bin *n*. The distribution of a Poisson random variable of mean $\bar{a}$ followed by a Bernoulli selection process with probability *p* is still Poisson with probability $\bar{a}p$ [111].Thus, we can describe the mean of the *n*th detector bin readout as the following:

$$\bar{g}_n = \sum_n \mathcal{H}_{mn} f_n \tag{8.5}$$

Since counts in each detector in are independent [111], the joint probability of the number of detected counts **g** conditioned on **f** is given by an independent Poisson distributed as

$$\Pr(\mathbf{g} \mid \mathbf{f}) = \prod_m \frac{e^{-[\boldsymbol{\mathcal{H}}\mathbf{f}]_m}}{g_m!} ([\boldsymbol{\mathcal{H}}\mathbf{f}]_m)^{g_m} \tag{8.6}$$

with mean, $\bar{\mathbf{g}} = <\mathbf{g}> = \boldsymbol{\mathcal{H}}\mathbf{f}$. Here, $\boldsymbol{\mathcal{H}}$ is the system matrix whose element represents the probability that a photon emitted from the *m*th object voxel would be detected by th *n*th detector bin. Due to the geometry of the collimator, the system matrix $\boldsymbol{\mathcal{H}}$ is a sparse matrix. Given Equation (8.6), we can express the forward projection model as a linear system equation:

$$\mathbf{g} = \boldsymbol{\mathcal{H}}\mathbf{f} + \mathbf{n} \tag{8.7}$$

where **g** is an instance of Poisson noise vector with mean $\boldsymbol{\mathcal{H}}\mathbf{f}$ and **n** is the noise component. Note that the Poisson noise is signal dependent, yet we are still able to express this noise as an additive term in Equation (8.7). The vectors **g** and **n** are random. In a later chapter, we will consider **f** to be a random vector.

In practice, $\mathcal{H}_{mn}$ will only need to be proportional to the probability of receiving a count in the *m*th detector bin emanating from the *n*th object voxel. For 3D SPECT with a $128 \times 128 \times 128$ object and data acquired over 128 angles using a 192-bin detector and 32-slices, the size of the system matrix stored in single -precision format is over 4TB. Storing and directly using such a

huge matrix, for example, in computing matrix vector products during reconstruction is impractical The matrix should be either computed on the fly or stored in some efficient way using specialized formats for this sparse matrix.

8.2 System Matrix $\mathcal{H}$

The system matrix $\mathcal{H}$ models the overall physical effects of the imaging system, such as geometrical response of the detector discussed earlier and interaction of the gamma photons with the human body. The matrix incorporates the object-dependent physical effects of attenuation and scatter. When a beam of photons passes through the human body, it will get absorbed as it interacts with the intervening tissue, similar to the X-ray photons we introduced before. This attenuation takes place mainly in two ways: Photoelectric effect and Compton effect [112], which are discussed in chapter 4. In this thesis, we do not consider the scatter effect, so our system matrix does not model the scatter.

8.2.1 Geometrical Response

Another important effect modeled in the system matrix is the detector response. In SPECT, "detector response" refers to the finite spatial resolution of the projection data due to the blur caused by the collimator geometry and intrinsic detector blur. The collimator geometry plays an important role in SPECT imaging system since it determines the acceptance angle, i.e., the directions of detectable projection rays. Thus, it will affect the quality acquired in the camera face and further affect the recon image quality. Collimator resolution, the blur caused by the collimator can be made better by using shorter/thicker or longer/thinner parallel holes. Figure 8.1 shows different detector response from a point source for different collimator.

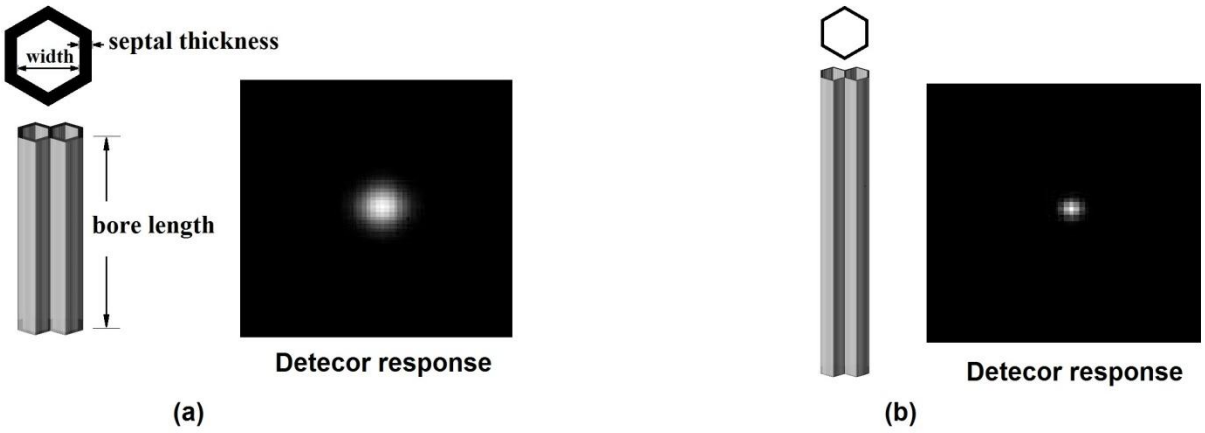

Figure 8.1: The noiseless detector response of point source from different collimators. (a) gives a detector response for a shorter and thicker collimator. (b) gives a detector response for a longer and thinner collimator.

However, collimator sensitivity is inversely related to collimator resolution [2], which means improving collimator resolution decreases collimator sensitivity (or efficiency), and vice versa. Reduced sensitivity means fewer counts, hence much higher Poisson noise level. Thus, there is a noise-resolution trade-off in the collimator design. High resolution and great sensitivity are two preeminent goals of SPECT. Different collimator designs have a different noise-resolution tradeoff. In this thesis, we focus on parallel-hole collimators with hexagonal hole shapes. Even with this constraint, the noise-resolution tradeoff for such collimator types still can vary a lot by their geometrical characteristics, hole width, length and septal thickness, which affect the geometric response of collimator in the camera face. Figure 8.2 gives a different noise-resolution tradeoff for different parallel hole collimator design in 2D example.

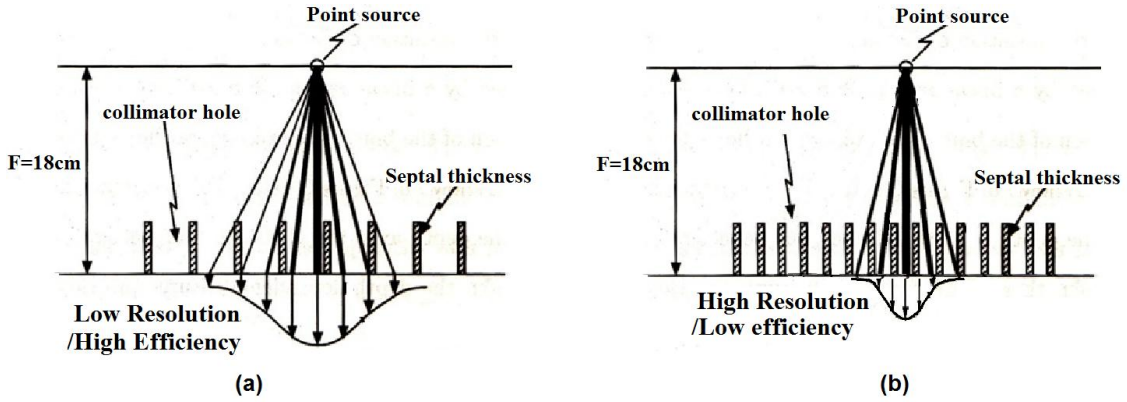

Figure 8.2: The different efficiency-resolution tradeoff for different collimators. (a) gives a low resolution/high efficiency tradeoff. (b) gives a high resolution/low efficiency tradeoff. Here (a) yields more counts but more blur and (b) less counts and less blur.

The detector response for the collimator geometry and intrinsic detector resolution can be modeled approximately by a depth-dependent Gaussian kernel [113]. We know that the intrinsic resolution of a detector is independent of the collimator blur. Usually the intrinsic detector blur is modeled as a Gaussian blur with a constant standard deviation (SD), σ_0 and typically on the order of 3 to 4mm. The collimator response is depth-dependent and is well modeled by a Gaussian function whose SD, $\sigma(d)$, grows approximately linearly with depth. The depth is the distance of a source point to the collimator. Thus the standard deviation of the geometric response blur can be modeled by,

$$\sigma(d) = \sqrt{\left(\frac{D}{2.35l}d\right)^2 + \sigma_0^2} \tag{8.8}$$

where *d*, the depth, is the distance between a point source and the camera surface (the crystal surface for the scintillator detector), *D* is the bore diameter *l* is the bore length. Usually, people are more familiar with Full Width at Half Maximum (FWHM). FWHM is equal to SD multiplying by a constant coefficient, 2.35. Thus, Equation (8.8) can be expressed in FWHM,

$$\mathrm{FWHM}(d) = \sqrt{\left(\frac{D}{l}d\right)^2 + (2.35\sigma_0)^2} \tag{8.9}$$

The efficiency is the percent photons accepted by the collimator, with these parameters, the average collimator efficiency is given by [2],

$$\text{Average Efficieny} = \frac{2}{\sqrt{3}} \frac{\pi D^4}{64l^2 \left[\frac{\sqrt{\pi}}{\sqrt[4]{12}} D + \text{SPT} \right]^2} \tag{8.10}$$

where SPT means the septal thickness. Thus, with Equation (8.9), the average efficiency can be approximated as,

$$\text{Average Efficieny} \sim \text{FWHM}^2 \tag{8.11}$$

In this thesis, we chose a family of 10 collimators to span a resolution-efficiency tradeoff. We seek that the collimator amongst the family that yields the best recon image quality.

For implementing this depth-dependent blur kernel, the entire object is divided into *L* zones parallel to the camera face at the *k*th angle with incrementally increasing distance from the camera face. The projection of all the voxels in the *l*th zone are convolved with the corresponding depth-dependent blur kernel, a Gaussian function with a SD in Equation (8.8). Each of these projection are then added to get the projection of the entire object on the camera face at the *k*th angle. The entire details of implementing the system matrix with only the geometrical effect is given in [114].

8.2.2 Other Collimator Features

In SPECT imaging, there are other collimators features that we need to worry about, the septal penetration, septal scatter and lead X-rays. As figure 8.3 shows, septal penetration means that incident photons supposed to be blocked by the collimator wall can pass through

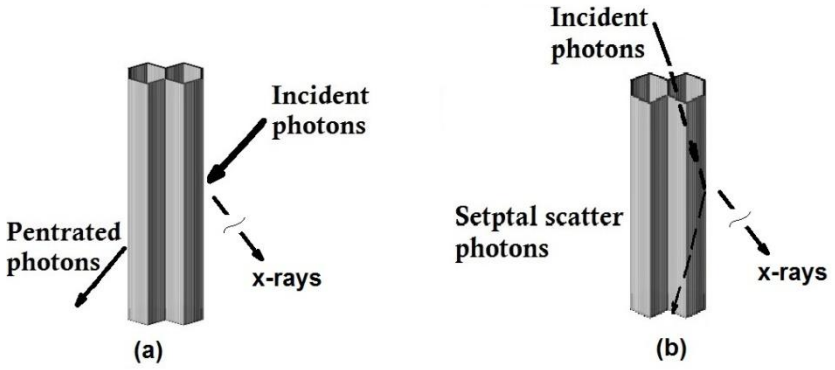

Figure 8.3: The other collimator features. (a) Septal penetration. (b) Septal scatter. During both interaction, the X-ray photons will be emitted.

the collimator with some probability and hit the detector. Septal scatter means that after the interaction between incident photons and the collimator wall, there is chance that these photons change direction and hit the detector. And last, during the interaction with collimator wall, e.g. collimator by lead, the lead X-rays might be emitted and included into the detector counts. These 3 effects also depend on the collimator geometry design and can provid extra photons that might affect the image quality. In our previous work, we studied these effects based on different collimator designs [115]. In this thesis, for the collimator, we just focus on the noise-resolution tradeoff due to the geometrical collimator design.

8.2.3 SPECT Image Reconstruction

The reconstruction method tries to estimate the object $\mathbf{f}$ by $\hat{\mathbf{f}}$ given the projection data $\mathbf{g}$ with knowledge of the statistics of $\mathbf{g}$ and the system matrix $\mathcal{H}$. We know the likelihood function given by Equation (8.6) stating that $\Pr(\mathbf{g}|\mathbf{f})$ is the independent Poisson distribution. Then we can get the log likelihood and use it as an objective function to compute the Maximum Likelihood (ML) estimate:

$$\hat{\mathbf{f}} = \arg\max_{\mathbf{f}} \left(\sum_m g_m [\mathcal{H}\mathbf{f}]_m - \sum_m [\mathcal{H}\mathbf{f}]_m \right) \tag{8.12}$$

where argmax is carried out by some optimization algorithm.

In practice, the ML solution is noisy due to the instability of problem, so a regularization term, also known as a penalty, is added into the objective function. The penalty used in this thesis is of the form:

$$\sum_n \sum_{p \in N(n)} w_{np} (f_n - f_p)^2 \tag{8.13}$$

where $N(n)$ is a neighborhood, the 26 NN (nearest neighbors) about n in 3D. This penalty encourages smooth solutions in the sense that if voxel f_n is close in values to its neighbors, it raises the objective function. The weights w_{np} are proportional to the inverse of the distance between the voxel n and voxel p. With the penalty term, we can write the penalized likelihood reconstruction problem as

$$\hat{\mathbf{f}} = \arg\max_{\mathbf{f}} \left(\sum_m g_m [\mathcal{H}\mathbf{f}]_m - \sum_m [\mathcal{H}\mathbf{f}]_m \right) - \beta \sum_i \sum_{j \in N(i)} w_{ij} (f_i - f_j)^2 \tag{8.14}$$

where $\beta > 0$ controls the overall influence of the penalty. In Equation (8.14), we note that $[\mathcal{H}\mathbf{f}]_m = \sum_n \mathcal{H}_{mn} f_n$. If β is low, the image has high resolution (little smoothing) but is noisy, as β increases, it encourages smoother, less noisy reconstruction images but they have less resolution (much smoothing). Figure 8.4 shows an example.

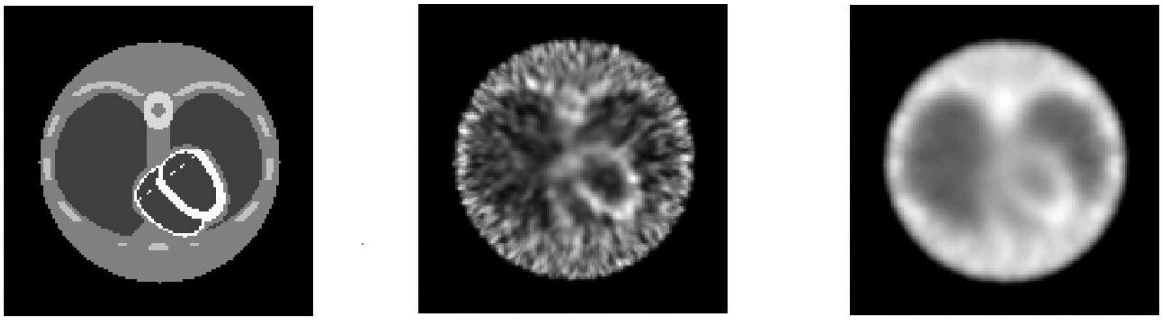

(a) Phantom (b) Recon with small β (c) Recon with large β

Figure 8.4: The recons with maximizing the objective function in Equation (8.14) with different β values. (a) is the phantom. (b) The recon with a small β. The recon image is shown as noisy but with high spatial resolution. (c) The recon with a large β. The recon image is shown as smooth but with low spatial resolution.

The choice of β is crucial since the purpose of the reconstruction is to allow us to see a lesion (signal). If the value of β is too large then a signal is smoothed out, and if β is too small, the signal is lost in the noise. Later, when talk about optimizing the SPECT system, β will play a crucial role.

We have not stated the actual algorithm used to optimize (i.e. carry out the argmax) the Equation (8.14). Reconstruction algorithms are a big topic and our lab has done much work on this topic. I will use a particular algorithm called COSEM-MAP (Complete Data Ordered Subset Expectation Maximization-Maximum a Posteriori) developed in [116]. The details are not important, We need only know that it maximizes the convex objective equation (8.14) to get the reconstruction while imposing the physical constraint that $f_n \geq 0$.

Chapter 9

Model Observers for Tasks

The most important criteria in measuring image quality is how well the image allows a human observer such as a radiologist to perform well on a relevant task. The task performance is measured by a scalar Figure of Merit (FOM). An image derived from system A with its particular hardware and reconstruction to considered "better" than an alternative system B if FOM(A) > FOM(B).

We consider two tasks. One is detection. For the detection task, we know where the signal is located and simply have to decide if it is present or not. Here, "signal implies a lesion or some clinically relevant signature that somewhat localized. The other task is detection-and-localization. Here, the radiologist (observer) is looking in a specific *region*, e.g. the left lung, and asking if a signal is present. If the signal is present, where is the signal located? An example of this is searching for a lung lesion. This type of detection + localization task is more clinically realistic than the simple detection task, but has received less attenuation in the past because the detection task is easier to analyze.

For convenience, we will use shorthand expressions "d-task" and "d+l task" to mean "detection task" and "detection and localization task", respectively. The FOM (Figure of Merit) acronym can apply to either task though we will explain specific FOM's for each task.

Ideally, the agent performing the task is a human observer, a radiologist viewing the image. There is a long tradition of procedures and mathematics involving such human studies [3] if applied to many systems are costly and extremely time consuming and are to impractical unless we are evaluating only one or two systems. Since d-task and d+l task are so laborious, there has been an extensive effect [105] to substitute mathematical "model" observers, derived from signal processing theory and psychophysics to emulate human observers. In this chapter, we describe the model observers for each task and their associated FOM's.

We note that a human observer has a 3D image to inspect but can only view a 2D "slice" at any moment. Therefore, we limit our analysis to 2D images.

Now the signal may be hard to see because it is blurred and masked by Poisson noise that is propagated into the reconstruction via the reconstruction algorithm. But there is another source of noise termed object variability we shall use "OV" to mean object variability. To see how OV can affect d-task or d+l task FOM, first consider breast imaging, where the parenchyma and other structures form a complex background that can mask a tumor even if there is no noise (Poisson noise) and blur in the reconstruction. Indeed, the OV is the main limitation in present-day conventional mammography. So even with an infinite dose (no Poisson noise) in breast imaging, mammography is "conspicuity limited" by OV.

For SPECT, OV takes the form of variability in the uptake **f**, so **f** could be considered random. It occurs on different spatial scales. Background variability found in real patient distribution includes anatomical variability [117], organ uptake variability and small scale local fluctuations [118] which can be referred as "texture". Since radionuclide tends to localize roughly uniformly in different anatomical organs, the shape/size variability of organs in patient population is a source of so-called anatomical variability. In addition, the average uptake level per organ can vary amongst populations, so that uptake variability is another source of object uncertainty. Perhaps most important are small scale "textural variations" due to small scale anatomical uptake variations in the object. This texture noise can easily mask detection of a lesion that would otherwise be easily seen against a uniform background. In the radar and remote-sensing literature this form of background variability is known as "clutter". Because small scale textural variability is such an important effect we shall henceforth imply this kind of variability when speaking of object variability.

A number of works have used models for texture variability based on random process from which the first and second moments can be derived analytically. One example of such analytic models is the "Lumpy" backgrounds [57, 119] derived by convolving a two-dimensional Poisson spatial point process with a "lump" profile. In another example [120], we modeled textural background variability as additive zero mean multivariate Gaussian noise. It was obtained by blurring iid Gaussian noise with a Gaussian kernel. In [108] variability was simulated using a stationary Gaussian process with a noise power spectrum which follows an inverse-power law over a range of spatial frequencies.

In sum, there are three things limiting task performance: noise blobs from the Poisson noise propagated from **g**, OV, and resolution, mostly due to the smoothing behavior of reconstructions.

9.1 Figure of Merit for Detection

We use standard statistical decision theory [57]. The model observer is applied to the image, a 2D slice of a reconstruction for which we will simply use $\hat{\mathbf{f}}$, to deliver a scalar observer response λ. the observer is a 2D template and act of observing to deliver a response can be summarized as an inner product,

$$\lambda = \mathbf{w}^T \hat{\mathbf{f}} \tag{8.1}$$

For human emulation, the inner product is a good model instead of the more general $\lambda = \mathbf{w}(\hat{\mathbf{f}})$. The template **w** is centered at the known location of the signal.

The response is compared to a threshold τ and if $\lambda \geq \tau$, the signal is deemed present; if $\lambda < \tau$ the signal is deemed absent, Now $\hat{\mathbf{f}}$ may actually have a signal or may not have a signal. So at a given τ, 4 possibilities exist: (1) True positive in which the observer decides signal present when it is present; (2) False positive where the observer decides signal present when it is absent; (3) True negative where the observer decides signal absent when it is truly absent; (4) False negative when the observer decides no signal when one is actually present. At a given τ,we can then define TPF = "True Positive Fraction", i.e. the probability that we decide true positive, FPF for "False Positive Fraction", TNF for "True Negative Fraction" and FNF for "False Negative Fraction". It is easy to see that TNF = 1-FPF and FNF = 1-TPF and FNF = 1-TPF. So we only need know TPF(τ) and FPF(τ), where we have included τ to emphasize the threshold dependence.

A plot of TPF(τ) vs. FPF(τ) as τ is varied is the well known ROC (Receiver Operating Characteristic) curve [3] used in detection theory analysis. Figure 9.1 shows three ROC curves. The area under the ROC curve is a natural Figure of Merit, FOM, for detection. For perfect performance, the ROC curve is the solid curve in Figure 9.1 and has area = 1 and the worst possible curve, tantamount to random guessing, is the dotted curve in Figure 9.1 and has area =

0.5. **For convenience, we use the acronym AROC (area under the ROC curve) as our FOM for detection.** AROC ultimately depends on the collimator and the reconstruction, so we shall use AROC to evaluate these components.

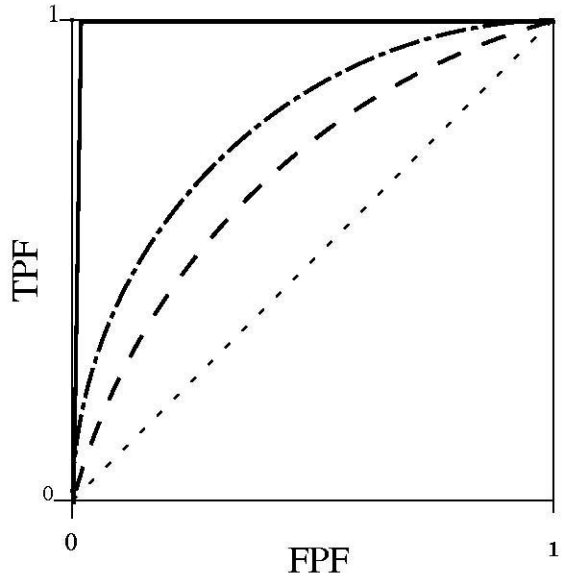

Figure 9.1: Plots of TPF vs. FPF showing a few ROC curves. The solid curve has a AUC=1, and is the best possible curve. The linear diagonal curve has an AUC=0.5 and is the worst. More realistic ROC curves are displayed as the dash-dot and dashed curves.

9.2 Channelized Hotelling Observer for Detection

So far we have not specified the observer **w**. The channelized Hotelling observer (CHO) [57] is found to be a good predictor of human performance in detecting lesions in correlated noisy background such as those in SPECT reconstruction [121-123]. Abbey and Barrett [121] found agreement in human and CHO performance in SKE tasks to investigate the effects of regularization in tomographic images. Gifford [122] *et al*. found correlation between CHO and human observers to evaluate the impact of detector-response compensation on tumor detection in SPECT.

For 2D monotone images as in SPECT, psychophysics have found that the human visual system extracts features from the image and then processes these features [57]. The human visual system processes an image through frequency-selective channels to extract features. In the CHO,

in order to model the human visual mechanism, each feature is obtained by applying a channel template at the lesion location. After reducing the input stimulus to a small set of channel responses, these responses are combined using an optimal linear combination rule (Hotelling). The loss of information due to channelization results in suboptimal performance. The suboptimal performance matches the naturally suboptimal performance of human observers.

To perform the feature extraction step the human visual system acts as if it operates on the Fourier transform of the retinal image. To extract each feature, the Fourier transform of the retinal image is integrated over the corresponding bandpass channel filter. This is mathematically equivalent to the inner product in the spatial domain of the image and the impulse response of the bandpass channel filter. The impulse response of the bandpass channel filter is the spatial domain representation of the channel.

The CHO observes a single 2D slice image extracted from the 3D reconstruction , as does a human observer. Let N_{2D} be the number of pixels in the extracted 2D image. The CHO applies anthropomorphic bandpass channels to reduce the N_{2D}-dim image into N_c channel responses (features). The feature reduction step is carried out by the dot product of the image with each of N_c channel templates, similar to the description above for the human visual system. Since N_c is usually around 3-6, the number features is far less than the number of pixels N_{2D}. If the vector $\mathbf{t}^i$ is the ith channel template centered at the lesion center, then the corresponding ith channel response is $\hat{u}_i = (\mathbf{t}^i)^T \hat{\mathbf{f}}$. The feature vector is given by $\hat{\mathbf{u}} = \mathcal{T}^T \hat{\mathbf{f}}$ where $\mathbf{t}^i$ is the ith column of $\mathcal{T}$, and $\mathcal{T}$ is an $N_{2D} \times N_c$ matrix.

We define $\mathbf{f}_1$ to be a signal absent object so that $\mathbf{f}_1 = \mathbf{b}$ where $\mathbf{b}$ is a background characterized by OV. Define $\mathbf{f}_2$ to be a signal-present object $\mathbf{f}_2 = \mathbf{s} + \mathbf{b}$ where $\mathbf{b}$ is again a random background and $\mathbf{s}$ is a N_{2D} component vector (not random) that is the signal. Then let $\hat{\mathbf{f}}_1, \hat{\mathbf{f}}_2$ be a reconstruction of $\mathbf{f}_1$ and $\mathbf{f}_2$, respectively. Let $\bar{\hat{\mathbf{f}}}_1, \bar{\hat{\mathbf{f}}}_2$ be the mean reconstructions averaged over OV and data noise (noise in $\mathbf{g}$). (Later we will comment on methods for obtaining such averages.) Let $\mathbf{K}_{\hat{\mathbf{f}}_1}$ and $\mathbf{K}_{\hat{\mathbf{f}}_2}$ be the covariance matrices of $\hat{\mathbf{f}}_1$ and $\hat{\mathbf{f}}_2$ respectively. These matrices are very large, $N_{2D} \times N_c$, but as we will see, this is not a problem. Note that

$$\mathbf{K}_{\hat{\mathbf{f}}_1} = (\hat{\mathbf{f}}_1 - \bar{\hat{\mathbf{f}}}_1)(\hat{\mathbf{f}}_1 - \bar{\hat{\mathbf{f}}}_1)^T \tag{8.2}$$

with a similar definition for $\mathbf{K}_{\hat{\mathbf{f}}_2}$. Finally, define the average covariance matrix as

$$\mathbf{K}_{\hat{\mathbf{f}}} = \frac{1}{2}(\mathbf{K}_{\hat{\mathbf{f}}_1} + \mathbf{K}_{\hat{\mathbf{f}}_2}) \tag{8.3}$$

We now consider the calculation of the first and second order moments of the feature vector. The quantities $\hat{\mathbf{f}}_1, \hat{\mathbf{f}}_2$ and $\mathbf{K}_{\hat{\mathbf{f}}}$ have been defined. The mean feature vectors $\bar{\hat{\mathbf{u}}}_1$ and $\bar{\hat{\mathbf{u}}}_2$ are obtained from $\hat{\mathbf{f}}_1$ and $\hat{\mathbf{f}}_2$, respectively.

$$\bar{\hat{\mathbf{u}}}_1 = \mathcal{T}^T \hat{\mathbf{f}}_1 \qquad \bar{\hat{\mathbf{u}}}_2 = \mathcal{T}^T \hat{\mathbf{f}}_2 \tag{8.4}$$

Let $\mathbf{K}_{\hat{\mathbf{u}}}$ be the average of the lesion-absent and -present channel response covariance matrices,

$$\mathbf{K}_{\hat{\mathbf{u}}_2} = \mathcal{T}^T \mathbf{K}_{\hat{\mathbf{f}}_2} \mathcal{T} \qquad \mathbf{K}_{\hat{\mathbf{u}}_1} = \mathcal{T}^T \mathbf{K}_{\hat{\mathbf{f}}_1} \mathcal{T} \tag{8.5}$$

Using Equation (8.3), we define channel covariance matrix $\mathbf{K}_{\hat{\mathbf{u}}}$ as

$$\mathbf{K}_{\hat{\mathbf{u}}} = \mathcal{T}^T \mathbf{K}_{\hat{\mathbf{f}}} \mathcal{T} \tag{8.6}$$

Note that $\mathbf{K}_{\hat{\mathbf{u}}}$ is a small matrix of dimension $N_c \times N_c$ so inversion is not a problem.

By combining all the steps just mentioned, we see that the CHO template is

$$\mathbf{w}_{CHO} = \mathbf{K}_{\hat{\mathbf{u}}}^{-1}(\bar{\hat{\mathbf{u}}}_2 - \bar{\hat{\mathbf{u}}}_1) \tag{8.7}$$

The effect of the CHO is to first extract features and then to apply an optimal (so called Hotelling) linear discriminant to the features. That is why $\mathbf{w}_{CHO}$ is linear.

For the bandpass channel feature extraction, we integrate the Fourier transform of $\hat{\mathbf{f}}$ over N_c bandpass regions in 2D Fourier space. This is equivalent to an inner product of $\hat{\mathbf{f}}$ with bandpass channel template in the 2D direct space. In previous work in our lab [120], we have extensively investigated the channel structure that yields performance that matches human behavior for SPECT images reconstructed with a penalized likelihood objective function.

To see what the CHO observer looks like, we plot in Figure 9.2 a profile of circularly symmetric annular bandpass regions in Fourier space. Note that there is a "gap" at low frequency. This is because the human eye responds poorly to low frequencies. Now integration of $\hat{\mathbf{f}}$ over the *i*th channel bandpass is equivalent to an inner product of the *i*th channel template $\mathbf{t}^i$ with the object, that is the operation $u_i = (\mathbf{t}^i)^T \hat{\mathbf{f}}$. The template $\mathbf{t}^i$ is is simply the inverse transform of the *i*th annular bandpass. Figure 9.2 (b) shows a grey scalar picture of $\mathbf{t}^1$, the first channel, and Figure 9.2 (c) is a central profile of the picture in Fig 9.2 (b)

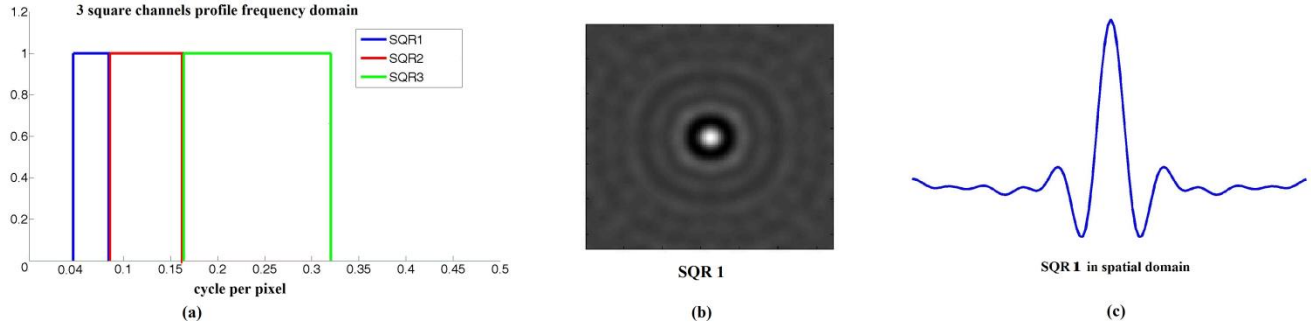

Figure 9.2: Details of CHO observer. (a) The 3 channels we used in this project. (b) The template in the spatial domain for the first channel. (c) The central profile of (b).

9.3 Evaluating AROC for Detection

For the binary (2 choices) detection task, there is a FOM called the signal-to-noise-ratio, SNR easier to calculate than AROC. However, the SNR is deterministically related to the AROC. We will define the SNR, show how to calculate it with sample methods, then show how to relate it to AROC.

In calculating our detection FOM, we present many $\hat{\mathbf{f}}_2$ images, in which we know the signal to be present and many $\hat{\mathbf{f}}_1$ images. The CHO observers "guess" whether signals are actually present. However, since we design the experiment and we know which images have the signal and which do not, we can take all $\lambda's$ associated with $\hat{\mathbf{f}}_2$ images and include them in a vector called $\boldsymbol{\lambda}_2$ and do the same for $\boldsymbol{\lambda}_1$. The FOM $\boldsymbol{SNR}^2$ is defined as

$$\mathrm{SNR}^2 = \frac{(\bar{\lambda}_2 - \bar{\lambda}_1)^2}{\frac{1}{2}[\mathrm{var}(\lambda_1) + \mathrm{var}(\lambda_2)]} \tag{8.8}$$

where the scalars $\bar{\lambda}_2$ and $\bar{\lambda}_2$ are the means of the components of $\boldsymbol{\lambda}_2$ and $\boldsymbol{\lambda}_1$, respectively. That is , we simply take the vectors $\boldsymbol{\lambda}_2$ and $\boldsymbol{\lambda}_1$ and average components. Similarly $\mathrm{var}(\boldsymbol{\lambda}_2)$ and $\mathrm{var}(\boldsymbol{\lambda}_1)$ are simply the variances of the components.

With some algebra [57], it is possible to show that for the CHO,

$$\mathrm{SNR}^2 = (\bar{\hat{\mathbf{u}}}_2 - \bar{\hat{\mathbf{u}}}_1)^T \mathbf{K}_u^{-1} (\bar{\hat{\mathbf{u}}}_2 - \bar{\hat{\mathbf{u}}}_1) \tag{8.9}$$

Surprisingly, if the observer response has a Gaussian distribution under each hypothesis then the SNR is related to AUC by [124]

$$\mathrm{SNR}^2 = 2\mathrm{erf}^{-1}(2AROC - 1) \tag{8.10}$$

We do not need equal variance for Equation (8.10) to hold. In practice, the λ_1 and λ_2 are Gaussian distributed due to a Central Limit Theorem argument so that Equation (8.10) holds.

Thus if we can get SNR, we can get AROC. The problem remains: How to get SNR?

9.4 Sample Methods for Obtaining SNR

We can calculate the CHO SNR with sample methods. First we reconstruct an ensemble of noisy reconstructions $\hat{\mathbf{f}}_1^k$ and $\hat{\mathbf{f}}_2^k$, where k=1,...N_{samp} indexes sample number. Projection data is obtained by adding Poisson noise to the projection of a random realization of the underlying background is used as the input for calculating each sample reconstruction. In Chapter 10, we give more computational details about forming $\hat{\mathbf{f}}_1^k$ and $\hat{\mathbf{f}}_2^k$. Then we obtain the channel response $\hat{\mathbf{u}}_1^k = \mathcal{T}\hat{\mathbf{f}}_1^k$ by applying the channel matrix at the lesion location on the extracted slice.

The sample means of the signal-present and -absent channel responses are given by

$$\hat{\mathbf{u}}_2^k = \frac{1}{N_{samp}} \sum_k \hat{\mathbf{u}}_2^k \quad \text{and} \quad \hat{\mathbf{u}}_1^k = \frac{1}{N_{samp}} \sum_k \hat{\mathbf{u}}_1^k \tag{8.11}$$

and the sample covariance of the channel responses is given by

$$\mathbf{K}_{\hat{\mathbf{u}}} = \frac{0.5}{N_{samp}-1}\sum_k (\hat{\mathbf{u}}_2^k - \hat{\mathbf{u}}_2^k)(\hat{\mathbf{u}}_2^k - \hat{\mathbf{u}}_2^k)^T + \frac{0.5}{N_{samp}-1}\sum_k (\hat{\mathbf{u}}_1^k - \hat{\mathbf{u}}_1^k)(\hat{\mathbf{u}}_1^k - \hat{\mathbf{u}}_1^k)^T \tag{8.12}$$

Since $\mathbf{K}_{\hat{\mathbf{u}}}$ is $N_c \times N_c$, calculating its inverse is trivial. To get a good estimate of $\mathbf{K}_{\hat{\mathbf{u}}}$ and its subsequent inverse, N_{samp} should be 10~ 1000 times N_c. We can then substitute Equation (8.11) and (8.12) to obtain the sample SNR. Note that N_c = 3 in our case and N_{samp} = 1024, so we have plenty of samples for calculating $\mathbf{K}_{\hat{\mathbf{u}}}^{-1}$. Once we have SNR, we can use Equation (8.10) to get our FOM, ARROC.

9.5 Introduction to the Detection and Localization Task

For the d+l task, the observer decides if one signal is present in a search region (e.g. lung) and if so, where? The "where" means localization. Localization is successful if the signal is present and the estimated location is within a tolerance radius of the true location. Figure 9.3 shows a cartoon slice of a chest object and examples of a search region, true location, estimated location and tolerance region.

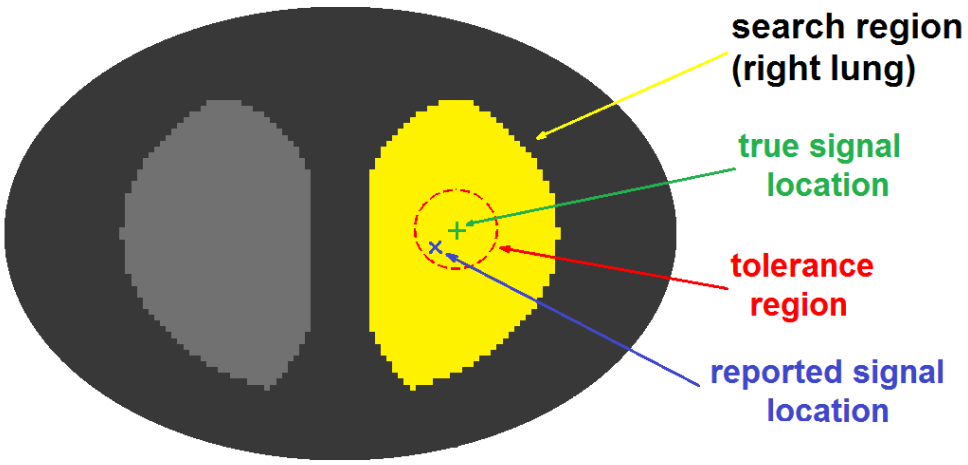

Figure 9.3: Components of detection and localization task: search region, signal location, estimated signal location and tolerance radius.

Since the signal may be present or absent, the detection correct or incorrect and the localization correct or not, four possibilities cases, shown in Figure 9.4, can occur.

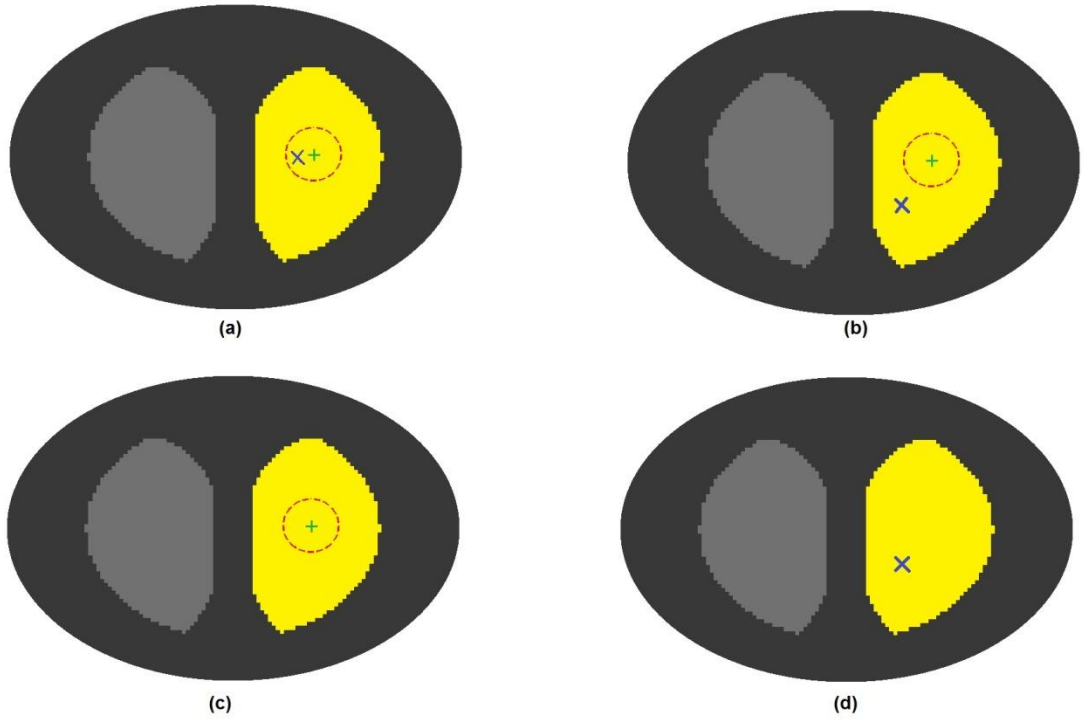

Figure 9.4: Possible outcomes of the detection and localization task. There are 4 possible outcomes labelled in (a) (b) (c) (d). In the figures, "+" is the location of the signal and "x" is its estimated location. The dotted circle is the tolerance region.

9.6 Model Observer for the Detection and Localization Task

This is a topic of ongoing research. Gifford [125] has proposed a model observer that emulates human performance well in SPECT and we use it here. The idea is that the observer template $\mathbf{w}_j$ *scans* over the search region. For convenience, we call the set of locations comprising the search region Ω and let j index locations in Ω. At each j, a local observer response λ_j is formed by a suitable inner product operation to be described below. Once all the $\lambda_j, j \in \Omega$ have been accumulated, one takes the final observer response to be the maximum of the λ_j's. The estimated location l is simply the j where the λ_j occurred. One still needs to decide whether a signal is present, so as in the detection task, λ is compared to a threshold τ

and "signal present" decided if $\lambda \geq \tau$, with "signal absent" decided otherwise. Now a present/absent decision may be incorrect, but if signal present is correctly chosen, one still needs to check whether *l*, the estimated location, lies within the tolerance region. If it does, the signal is said to be "correctly localized". Let us repeat this more formally and also define the observer.

Let $\mathbf{f}_2 = \mathbf{b} + \mathbf{s}_{loc}$ be a signal-present object with $\mathbf{b}$ a random, due to OV, background and $\mathbf{s}$ the signal located a true location "*loc*". Let $\mathbf{f}_1 = \mathbf{b}$ be a signal-absent object. Note that $loc \in \Omega$ the search region by definition. Let $\hat{\mathbf{f}}_1$ and $\hat{\mathbf{f}}_2$ be reconstruction of $\mathbf{f}_1$ and $\mathbf{f}_2$, respectively.

Let the scanning observer be, $\mathbf{w}_j, j \in \Omega$. Then

$$\lambda_j = \mathbf{w}_j^T (\hat{\mathbf{f}} - \bar{\hat{\mathbf{b}}}) \qquad j \in \Omega \tag{8.13}$$

where $\bar{\hat{\mathbf{b}}}$ is the reconstructed background averaged over OV and Poisson noise in the reconstruction and $\hat{\mathbf{f}}$ can be $\hat{\mathbf{f}}_1$ or $\hat{\mathbf{f}}_2$. Unlike the case for detection, Equation (8.13) includes a background subtraction step. This is necessary because of the max λ_j step to be performed. If the signal is in a region of low-value background, it will be ignored in favor of some other signal candidate that happens to lie atop a high background, so the background subtraction step is needed.

Gifford found that $\mathbf{w}_j$ can assume a surprisingly simple form. The $\mathbf{w}_j$ is a CNPW (Channelized Non Pre Whitening filter), essentially a CHO but without the covariance matrix. The form for $\mathbf{w}_j$ is given by

$$\mathbf{w}_j = \mathcal{T}\mathcal{T}^T \bar{\hat{\mathbf{s}}}_j \tag{8.14}$$

where $\mathcal{T}$ is the channel matrix as described earlier and $\bar{\hat{\mathbf{s}}}_j = \overline{\mathbf{b}+\mathbf{s}_{loc}} - \bar{\hat{\mathbf{b}}}$.

Given λ_j, take $\lambda = \max_j \lambda_j$ and estimated location $l = \arg\max_j \lambda_j$. Thus the observer response is the *pair* (λ, l). Compare λ to a threshold τ. If $\lambda < \tau$, decide signal absent and if $\lambda \geq \tau$ decide signal present at *l.*

To gauge performance we can supply N_{samp} signal-present and N_{samp} signal-absent objects $\mathbf{f}_1^k$ and $\mathbf{f}_2^k$, $k = 1,...,N_{samp}$. We can accumulate the $k = 1,...,N_{samp}$ positive responses (λ_+^k, l^k) and N_{samp} negative responses (λ_-^k) from the known objects. Unlike the detection case, there is no convenient SNR^2 expression so we need to compute our FOM by directly considering the appropriate ROC curve.

In this case, the appropriate case is the LROC curve (Localization ROC curve) [4]. Unlike the ROC curve, it measures, as τ is swept, the correct localization rate P_{CL} vs. the false positive rate P_{FP}. The false positive rate is the same as used in the ROC curve, but P_{CL} is the probability that if a signal is present, we decide that it is present and we also correctly localize it within a tolerance. Thus for all (λ_+^k, l^k) responses, we retain only these where l^k is within the tolerance and eliminate all other positive responses. Finally we end up with a histogram of λ_+ and λ_- responses from which an LROC curve can be calculated. Figure 9.5 shows a typical LROC curve. Note that the LROC curve needs not pass through the point (1,1). Its max value can be less than 1.

The final FOM is ALROC, the area under the LROC curve. ALROC can depend on the collimator, the reconstruction algorithm and other factors. Details of a numerical integration

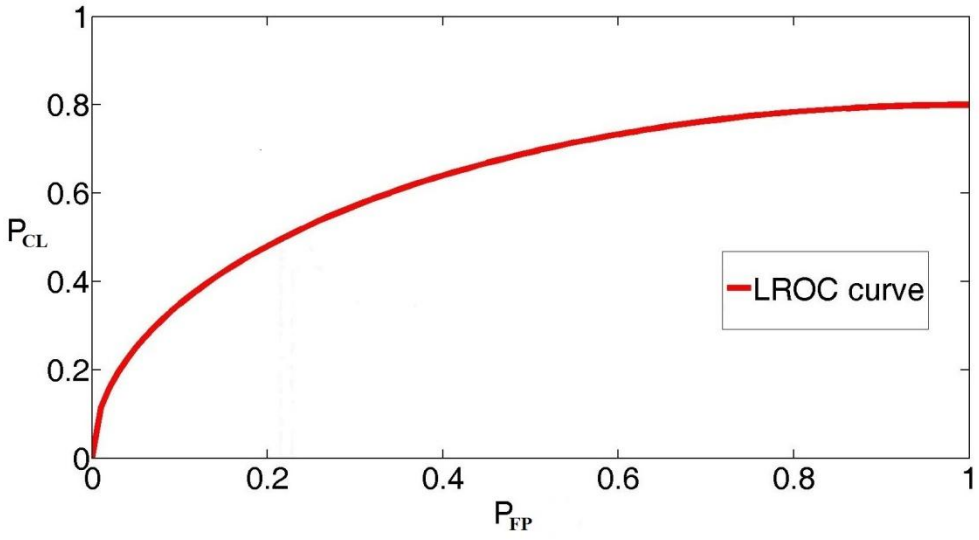

Figure 9.5: LROC curve measures probability of correct localization vs. false positive rate

procedure for converting the λ_+ and λ_- values to an LROC curve and integrating the curve to obtain ALROC can be found in [126].

Chapter 10

System Optimization for SPECT

In this chapter I describe simulation experiments used to optimize a SPECT system in terms of task performance. The items we optimize are the collimator choice and the crucial factor β that controls the noise/resolution tradeoff in the reconstruction as I showed in Figure 8.4. We make use of sample methods and the model observers of Chapter 9 in computing the task performance FOMs.

10.1 Collimator Family

In Chapter 9, we described how the efficiency and resolution of a collimator can be traded off by adjusting the collimator bore geometry. For our experiment, we chose a family of 10 collimators, labeled as, c1, c2,..., c10 as a family over which to optimize.

The notion was adjust the bore geometries so that c1, c2, ..., c10 spanned an efficiency-resolution tradeoff. We used Equation (8.9) and (8.10) to calculate resolution in terms of FWHM of a point source placed 18 cm form the face of the detector. During the design of the collimator, we kept a constant ratio between the septal thickness and bore width, so that each collimator had a roughly equal amount of septal penetration. Table 10.1 shows the numerical results.

Table 10.1: Details of the collimator family design for different Efficiency/Resolution tradeoff.

Collimator name	System resolution at point source at F=180mm	Collimator sensitivity (x1000)	Hole size h (mm)	Septal thickness SPT (mm)	Relative sensitivity to LEHR
c1	7.92921	0.0719	0.89	0.13	0.6414
C2 (LEHR)	9.88932	0.1121	1.11	0.16	1.0000
C3	11.8493	0.1614	1.33	0.19	1.4398
C4	13.7202	0.2139	1.54	0.23	1.9081
C5	15.6803	0.2830	1.76	0.25	2.5245
C6	17.6403	0.3585	1.98	0.28	3.1980
C7	19.5113	0.4385	2.19	0.31	3.9117
C8	21.4713	0.5315	2.41	0.34	4.7413
C9	23.4314	0.6292	2.63	0.38	5.6128
C10	25.3914	0.7397	2.85	0.41	6.5986

It is more insightful to ignore the specific bore parameters and simply plot resolution vs. efficiency for the collimator family as shown in Figure 10.1. This clearly shows the efficiency/resolution tradeoff. Recall that more efficiency means more photons collected on the camera face and less relative Poisson noise, but this comes at the expense of poorer resolution (larger FWHM). So Figure 10.1 shows the noise/resolution tradeoff.

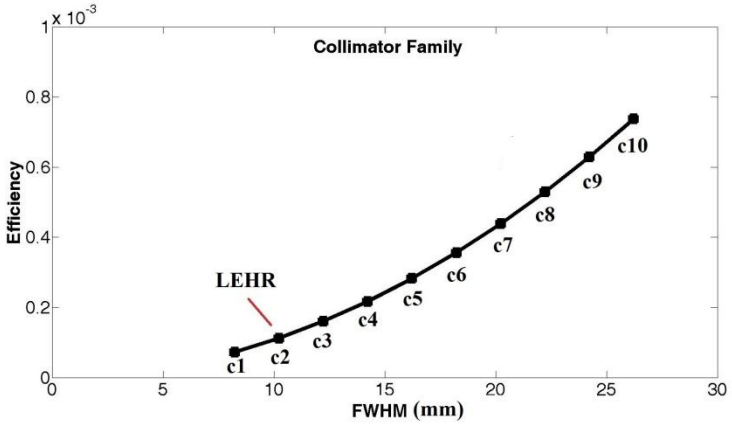

Figure 10.1: The collimator family curve showing the Efficiency/Resolution tradeoff. In this figure, the FWHM is measured at 180mm between the point source and collimator surface.

Note that one collimator, c2, is labeled LEHR (Low Efficiency High Resolution). For our simulations, which approximate clinical conditions, the LEHR would be the collimator used in the clinic. Hence we are interested in seeing if a collimator other than the conventional one yields the best performance.

We can use the FWHM as a collimator index. For example, given the FWHM, one can use Figure 10.1 to look up the efficiency or use Table 10.1 to look up all details on the collimator.

10.2 Range of Smoothing Parameters

The value of β in the objective function Equation (8.14) ranges over about 4 orders of magnitude as the reconstructed images goes from very smooth to very noisy. We simply use the value of β as an index in the FOM evaluation.

As explained in Chapter 9, our FOMs are AROC and ALROC. Thus we will evaluate AROC(FWHM, β) and ALROC(FWHM, β) for the d-task and d+l task, respectively.

10.3 Joint Optimization Approach

To obtain the optimal values of β and collimator choice we evaluated AROC(FWHM, β) for detection and ALROC(FWHM, β) for detection-localization and picked the best collimator, indicated by FWHM* and best smoothing β indicated by β^* that maximizes FOM. So for detection,

$$(\text{FWHM}^*, \beta^*) = \underset{\text{FWHM}, \beta}{\text{argmax}} \ \text{AROC}(\text{FWHM}, \beta) \tag{10.1}$$

with a similar equation holding for ALROC. Figure 10.2 indicates the strategy for the detection task. Simply replace AROC by ALROC in Figure 10.2 to get the strategy for the detection-localization task

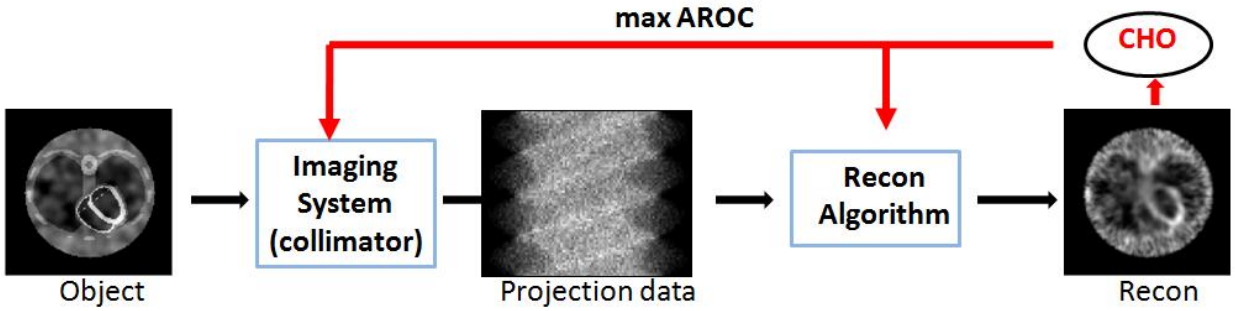

Figure 10.2: The figure shows the strategy of the joint system optimization, using the detection task as one example.

There are 10 collimators and 10 values of β so the search space has a size of 100 values. We use sample methods to evaluate each of the 100 FOMs and simply choose the maximum. There is no optimization algorithm that we can apply since we do not know if AROC(FWHM, β) or ALROC(FWHM, β) is convex.

One alternative strategy is "Sequential Optimization" in which the FWHM for the collimator is first optimized to obtain FWHM*, and with the collimator fixed, β is then optimized to obtain β^*. While the β -optimization uses the CHO to obtain AROC, the FWHM optimization uses an "ideal observer", one that is designed to yield the maximum possible performance (AROC or ALROC) over all observers. The ideal observer is described in [57] and was used by us previously [127] for collimator optimization.

The notion behind the ideal observer is that the projection data is the best possible, i.e. has max AROC (for detection) for any observer applied to the projection data. With such high quality projection data, the thought is that the FOM for the CHO applied to the subsequent reconstruction will somehow be optimal. The sequential strategy is outlined in the Figure 10.3 for AROC case.

Yet despite the elegance of the ideal observer approach, the joint optimization approach will yield a higher FOM **by construction**, so we stick with the joint optimization approach.

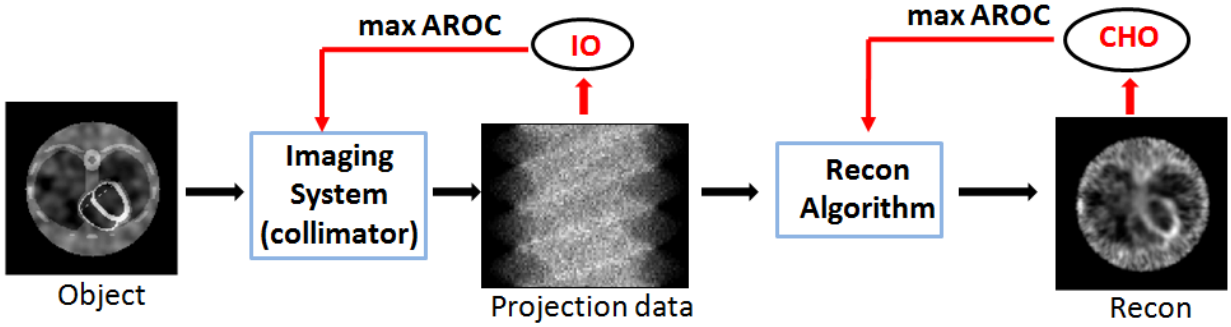

Figure 10.3: The figure shows the strategy of the sequential system optimization, using the detection task as one example. Here, IO means "Ideal Observer".

10.4 Simulation Experimental Details: Phantoms

We simulated two cylindrical phantoms of diameter 31.2 cm and length 47.42 cm and filled them with the radionuclide Tc^{99m}. The background **b** had an OV characterization by a 3D Gaussian power spectrum with correlation width 1.2 cm and standard deviation at each pixel of 20% of the background value. The object is 128×128 pixels per slice with 152 slices, with each voxel cubic and 0.312 cm on a side. We simulate the radionuclide sitting in water whose attenuation coefficient for the 140 keV Tc^{99m} is known to be 0.15 cm^{-1}. We did not simulate patient scatter.

With all these parameters, the number of counts received for an LEHR collimator is 10^6, consistent with a typical clinical scenario. The geometry of the detector and the circular orbit was designed to emulate a typical clinical scanner.

Because of the computational complexity of image formation and reconstruction, we placed multiple signals per object. For the detection task, we placed one spherical "hot spot" every 13 slices, alternating a "+" with an "×" pattern as shown in Figure 10.4. This led to 52 signals per object. The signal locations were chosen to not interact. That is, we verified that the presence of a signal did not affect performance on an adjacent signal. The Figure 10.4 shows the cylinder and two slices with OV background and signals. We tried signal sizes of various diameters and contrasts. Here is the list of signal diameters with contrasts, signal : background: 8mm with 5:1, 16mm with 1.2, 18mm with 0.75:1, 22mm with 0.6:1.

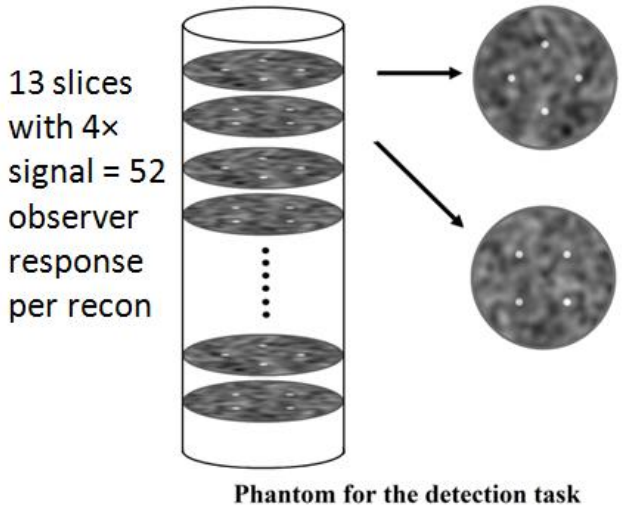

Figure 10.4: Phantom for the detection task: The cylindrical object containing Tc^{99m} in H_2O is shown. Every 13th slice has 4 spherical signals. Two slices illustrate the signal placement and Gaussian OV.

For the detection-localization task, we also used the same Tc^{99m} cylindrical phantom with the same Gaussian OV and with H_2O attenuator as for the detection task. Here only 37 equispaced slices contain signals as shown in Figure 10.5. Each signal is inside an "L" shaped search region with the orientation of "L's" staggered as shown in Figure 10.5. This guarantees that the presence of a signal in one slice did not affect the performance on an adjacent signal. The signals were spheres of (diameter, contrast) = (8mm,16:1) and (16mm, 2.7).

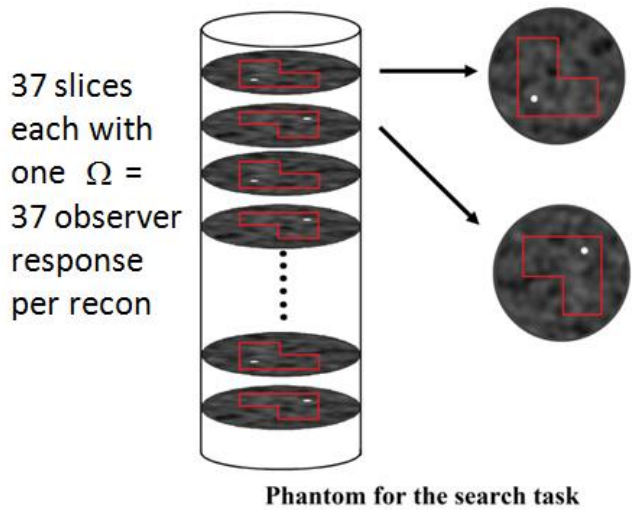

Figure 10.5: Phantom for the detection/localization task: 37 slices contain one signal. The "L" shape search region Ω is shown.

We have shown signal present images for each task. For signal absent images, we simply eliminated the signals.

10.5 Simulation Experimental Details: Sample Methods and Computational Complexity

We describe details for the detection experiment first. In the ensuing description, we assume N_{samp} = 1024 for the sample size, but then show tricks that allow us to reduce N_{samp}. For a given signal size and contrast, we assumed N_{samp} = 1024 signal present phantoms, $\mathbf{f}_+^k$, k=1,...1024, each with a different OV noise realization. We also assume N_{samp} = 1024 signal absent phantoms, $\mathbf{f}_-^k$, k=1,...1024, each with a different OV noise realization.

For each $\mathbf{f}_+^k$ and each $\mathbf{f}_-^k$, we created projection data, including Poisson noise, $\mathbf{g}_+^k$ and each $\mathbf{g}_-^k$. To do this we used our legacy code MIPLsim which, given the object, attenuation map and collimator parameters, simulates the physics of image formation $\mathbf{g} = \mathcal{H}\mathbf{f} + \mathbf{n}$. This program has been developed over many years and my contribution to it was to speed up the depth-dependent collimator response module by using GPU acceleration. Since each $\mathbf{g}$ depends on the collimator chosen, the net output of this stage can be listed as $\mathbf{g}_+^k(\text{FWHM})$ and $\mathbf{g}_-^k(\text{FWHM})$, k=1,...,1024.

Each of the **g**'s needs to be reconstructed using a particular β. We use the COSEM-MAP module of MIPLsim to create reconstructions $\hat{\mathbf{f}}_+^k(\text{FWHM}, \beta)$ and $\hat{\mathbf{f}}_-^k(\text{FWHM}, \beta)$, k=1,...,1024 . Thus, for each of the 100 combinations of collimator and β, we would have 1024 signal present and 1024 signal-absent reconstructions.

If each $\hat{\mathbf{f}}_+^k$ had one signal, then for each point AROC(FWHM, β), we would need $2 \times N_{samp}$ = $2048 \sim 2 \times 10^3$ reconstructions (1024 for $\hat{\mathbf{f}}_+^k$ and 1024 for $\hat{\mathbf{f}}_-^k$). The surface AROC(FWHM, β) has $100 \sim 10^2$ combinations of (FWHM, β) values. We try a few (4) signal sizes and 2 tasks ($\sim 10^1$). Therefore, the number of recons for a complete joint optimization study is $2 \times 4 \times 2 \times 10^3 \times 10^1 \approx 2$ million 3D iterative recons! A CPU based iterative recon takes many minutes so clearly this is quite impractical.

We can reduce computational complexity in several ways. The GPU acceleration yields a speedup of 30. For the detection task, we multiplex 52 signals per $\mathbf{f}_+^k$ so that the multiplex speedup is 50. The total speedup due to multiplex and due to GPU is then $30 \times 50 \approx 10^3$. Hence instead of 2 million recons, we need only 2000 recons. While 2000 recons requires several days of computation on our machines, it is feasible to do. With the 2000 recons, we are ready for the FOM evaluation stage. The situation for the detection-localization stage is quite similar: using one signal per $\hat{\mathbf{f}}_+^k$ would require about 2 million recons, but multiplex (37 signals per $\hat{\mathbf{f}}_+^k$) and GPU yield a requirement of only about 2000 recons. Given these reconstructions, we are then ready for the FOM evaluation stage. The multiplexing allows us to reduce N_{samp} to 1024/52 for detection and 1024/27 for detection-localization task.

We have already described in Chapter 9 on how to compute AROC and ALROC given N_{samp} images. For AROC, we apply the CHO, compute SNR^2 and convert to AROC. We do this for each combination of collimator and β, thus obtaining a surface AROC(FWHM, β). For ALROC, we apply the scanning CNPW observer to obtain the observer responses and locations, and evaluate ALROC as described previously. This yields a surface ALROC(FWHM, β).

For the AROC(FWHM, β) and ALROC(FWHM, β) surfaces, we locate the best collimator FWHM^* and regularizer β^* using Equation (10.1) and then draw our conclusions. We have

described the experimental procedures for SPECT system optimization. In the next section we show the results.

10.6 Results of Joint Optimization Study

We use the previously described data pipeline for obtaining surfaces (i.e. surface plots) AROC(FWHM, β) and ALROC(FWHM, β) for the two tasks and a variety of signal sizes and contrasts.

We first show the AROC surface for the 16mm diameter signal in some detail since this figure will be useful in understanding the other surface plots. In Figure 10.6, the axis labeled FWHM indexes the c1, ..., c10 collimators according to the indexing scheme previously in Table 10.1 while the axis labeled β indexes the 10 values of β that we used: 10^{-3}, 5^{-3}, 10^{-2}, 5^{-2}, 10^{-1}, 5^{-1}, 1, 5, 10, 50. The ordinate for this detection task is the AROC value at each of 100 pairs of (FWHM, β) values. As can be seen, the optimal combination is FWHM* = 11.85 mm and β^* = 0.1 and at the value AROC = 0.8572.

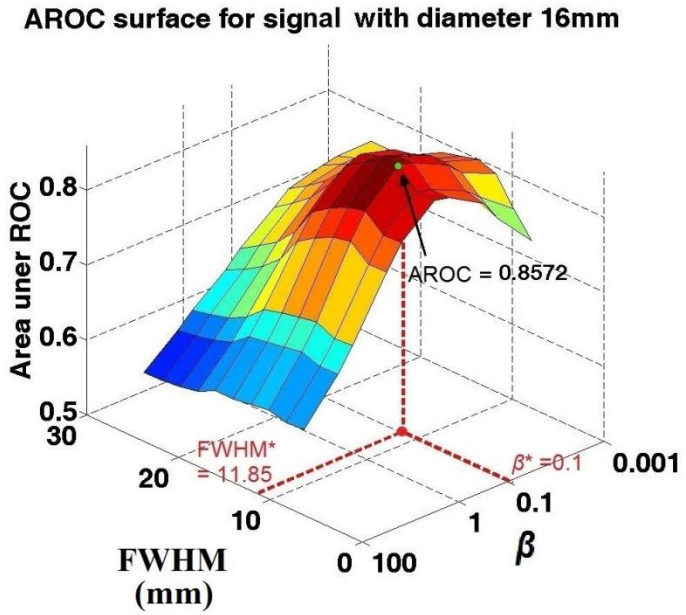

Figure 10.6: AROC surface for 16mm diameter signal. The optimal collimator FWHM* and smoothing parameter β^* are shown

In Figure 10.7, we show the surfaces for all our detection experiments. Table 10.2 lists the results for the optimal collimator and smoothing in each case for detection task. As we can see that, for the detection task, the optimal collimator gets wider as the signal size increases. At the same time, the best smoothing term β stays the same.

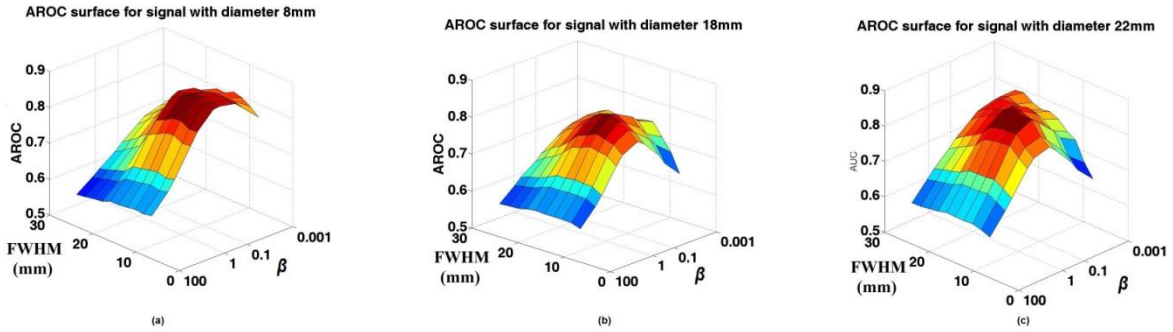

Figure 10.7: Performance surfaces for detection task, (a) signal size = 8mm, contrast = 5:1; (b) signal size = 18mm, contrast = 0.75:1; (c) signal size = 22mm, contrast = 0.6:1.

Table 10.2: The optimal collimator and β for different signal sizes in detection task.

Signal size in diameter	Optimal Collimator	Optimal β
8mm	c3	0.1
16mm	c3	0.1
18mm	c4	0.1
22mm	c5	0.1

In Figure 10.8, we show the surface for all of our detection and localization experiments for 2 different signal sizes, 8 mm and 16 mm diameters. Table 10.3 lists the results for the optimal collimator and smoothing in each case for the detection-localization task.

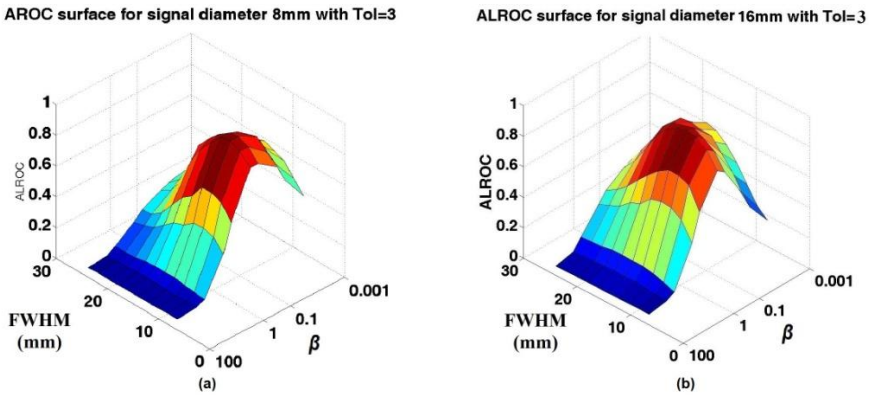

Figure 10.8: Performance surfaces for detection-localization task, (a) signal size = 8 mm, contrast = 16:1; (b) signal size =16 mm, contrast = 2.7:1.

Table 10.3: The optimal collimator and β for different signal sizes in detection-localization task.

Signal size in diameter	Optimal Collimator	Optimal β
8mm	c3	0.05
16mm	c4	0.1

By inspection of the AROC and ALROC surfaces, we see that only a few (typically 5) points are sufficiently close to the maximum point for differences to be tested for p-value significance. Table 10.4 includes this information. Inspection of Table 10.4 shows that the peak (FWHM*, β^*) values are generally significantly ($p < 0.05$) greater than this neighbors except for several instances circled in the table.

Table 10.4: Tables for p-value test for statistical significance between two AROC/ ALROC values. The circled entries indicate the pairwise comparisons where $p > 0.05$.

(a) P-value test for AROC surface with signal size 8 mm in diameter.

AROC pairs & peak is ***(c3,0.1)***	P value
(c3,0.1) vs. (c2, 0.1)	**0.0459**
(c3, 0.1) vs. (c4, 0.1)	**0.0035**
(c3, 0.1) vs. (c3, 0.05)	**0.2369**
(c3, 0.1) vs. (c2, 0.05)	**0.0721**
(c3, 0.1) vs. (c4, 0.05)	**0.0021**

(b) P-value test for AROC surface with signal size 16 mm in diameter.

AROC pairs & peak is ***(c3,0.1)***	P value
(c3,0.1) vs. (c2, 0.1)	**6.1275e-06**
(c3, 0.1) vs. (c4, 0.1)	**0.0870**
(c3, 0.1) vs. (c3, 0.05)	**2.3490e-04**
(c3, 0.1) vs. (c2, 0.05)	**1.6436e-07**
(c3, 0.1) vs. (c4, 0.05)	**0.0020**

(c) P-value test for ALROC surface with signal size 8 mm in diameter.

ALROC pairs & peak is ***(c3,0.05)***	P value
(c3,0.05) vs. (c2, 0.05)	**2.5979e-05**
(c3, 0.05) vs. (c4, 0.05)	**0.0973**
(c3, 0.05) vs. (c3, 0.1)	**0.0021**
(c3, 0.05) vs. (c2, 0.1)	**5.4896e-07**
(c3, 0.05) vs. (c4, 0.1)	**0.0064**

(d) P-value test for ALROC surface with signal size 16 mm in diameter.

ALROC pairs & peak is ***(c4,0.1)***	P value
(c4,0.1) vs. (c3, 0.1)	**0.0228**
(c4, 0.1) vs. (c5, 0.1)	**2.7456e-05**
(c4, 0.1) vs. (c4, 0.05)	**0.0121**
(c4, 0.1) vs. (c3, 0.05)	**9.0084e-06**
(c4, 0.1) vs. (c5, 0.05)	**2.6497e-04**

By checking Tables 10.2 and 10.3, we can see that the optimal collimator, FWHM* for the detection task or the detection-localization task is wider than our reference collimator, the LEHR collimator, which is widely used in the clinic. The optimal smoothing parameter, β, is stable with different signal sizes for the detection task or the detection-localization task.

10.7 Comparison of AROC and ALROC Task Performance

Examination of our results shows that the detection-localization task is more sensitive than the more conventionally used simple detection task. This can be seen in Figure 10.9, which shows AROC and ALROC surfaces superposed. The ordinate of Figure 10.9 plots both AROC and ALROC, though the absolute values of these are incommensurate since each applies to a different task.

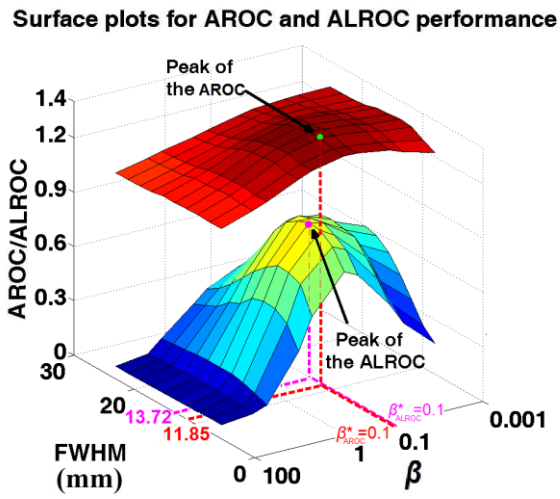

Figure 10.9: ALROC vs. AROC performance surface for the case of a signal of 16mm diameter and 1.2:1 contrast for detection task and 2.7:1 for the detection and localization task

Nevertheless, it is easy to observe that the relatively flat AROC surface is much flatter than the highly peaked ALROC surface. This means that a slight change in collimator choice or smoothness can affect the detection-localization task greatly while not affecting the detection task AROC. Since the detection-localization task is more clinically realistic, the fact that it is more sensitive than the simple detection task is an important conclusion. It tells us that the collimator and smoothing should be chosen carefully if we decide to use the detection-localization task as our metric.

It is instructive to look at recon slices containing the center of the signal for various choices of FWHM and β for each task. Figure 10.10 shows reconstructions for each task with the leftmost image being the phantom. For the detection task, the optimal setting of collimator c3 and $\beta^* = 0.1$ indeed shows the 4 signals most clearly. For the detection-localization task, the reconstruction at optimal collimator c4 and $\beta^* = 0.1$ shows the signal most clearly. There are anecdotal reconstructions but are typical.

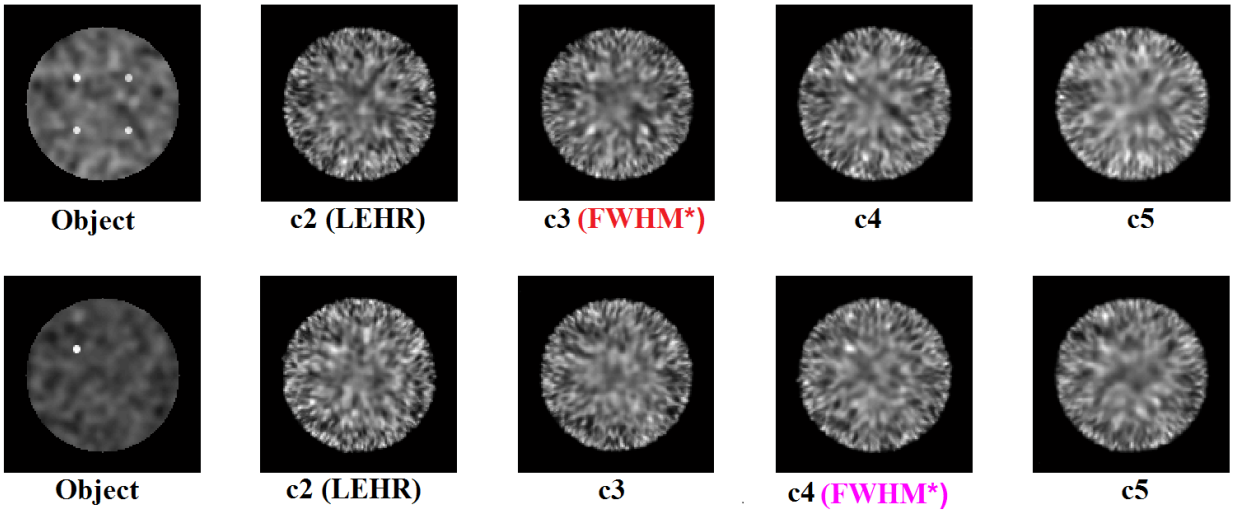

Figure 10.10: Anecdotal reconstructions for various parameter settings. Top row for detection task shows phantom then 4 reconstructions. The optimal (FWHM*, β^*) indeed shows the signals most clearly. For top row, with $\beta^* = 0.1$ in cases. Bottom row shows the same situation for the detection-localization task with $\beta^* = 0.1$. The c4 collimator shows the signal most clearly.

10.8 Overall Conclusions

For my SPECT study, I reach several conclusions: (a) Use joint optimization to optimize the collimator/smoothing parameters; (b) Use wider bore, more efficient collimators than commercial versions; (c) Task sensitivity is much greater for the detection-localization task and it is worth optimizing ALROC instead of AROC since the detection-localization task is more clinically relevant.

Chapter 11

Summary and Future Work

In this thesis, I have addressed the problem of improving image quality in two medical modalities, contrast-enhanced-dual-energy digital breast tomosynthesis and SPECT. For tomosynthesis, I showed that interleaved acquisition and reconstruction followed by weighted subtraction yields improved result in terms of SDNR. As part of this work, I adapted the filtered backprojection for a limited angle stationary geometry used in tomosynthesis. For SPECT, I used model observers and statistical decision theory to optimize the data acquisition (collimators) and data processing (regularization in tomographic reconstruction) to maximize performance on the detection and detection-localization tasks.

If this work were to be continued, here are some future directions. For SPECT, we should model effects of patient scatter. Scatter generally reduces signal detectability in the reconstruction and so could affect our conclusions on optimal systems. Unfortunately, scatter is computationally difficult to simulate since it requires a Monte Carlo photon tracking package. Also, one should consider septal penetration and septal scatter effects for the collimator since these can be significant [115].

To get closer to using this work for real medical use, one should alter the simulation to focus on a specific medical problem instead of a simple problem such as detecting spheres in a background. For example, in cardiac SPECT, a significant application in SPECT, one could replace our cylindrical phantoms with an elaborate digital phantom designed to reflect the human anatomy along with the spatial pattern of the radiopharmaceutical uptake. Such phantoms are available and have been developed in the medical community. In cardiac SPECT , clinicians have the task of detecting "cold spots" (areas of decreased activity) in the myocardial wall [2].

We have considered an important form of object variability, namely "textural" variability characterized by small spatial scale fluctuations. That is important in affecting lesion detection which was demonstrated by the work in our group [128]. We chose, for convenience, a stationary 3D random process with an underlying Gaussian pdf and a Gaussian power spectrum of appropriate correlation width and amplitude. (This is easy to generate using i.i.d random number generators followed by filtering.)

However, a second form of OV, the overall variation of patient size and organ size and uptake, also affects lesion detectability. To capture this form of OV, we need access to a database of patient scans processed by techniques such as those in [117].

The use of model observers is not intended to yield conclusions immediately useful in changing imaging system design or reconstruction algorithm. However, it is a rapid way to narrow the search to a few candidates. For our SPECT work, our search space was collimator c1, ...c10 and 10 values of β. The final choice from the fewer candidates delivered by the model observers must be made by human observer testing using ROC [129, 130] or alternative forced choice techniques [131]. We have used human observer testing in our lab for SPECT [120] and for breast tomosynthesis [132] but this was beyond the scope of the present thesis.

References:

[1] J. Hsieh, *Computed Tomography: Principles, Design, Artifacts, and Recent Advances*: SPIE Press, 2009.

[2] M. N. Wernick and J. N. Aarsvold, "Emission Tomography: The Funcamentals of PET and SPECT," *Elsevier Adademic Press*, 2004.

[3] C. Metz, "Some Practical Issue of Experimental Design and Data Analysis in Radiological ROC Studies," *Invest. Radiol.,*, vol. 24, pp. 234-245, 1989.

[4] R. G. Swensson, "Unified Measurement of Observer Performance in Detecting and Localizing Target Objects on Images," *Med Phys*, pp. 1709-1725, 1996.

[5] *American Cancer Society , "Cancer Facts and Figures 2012"*

[6] E. D. Pisano, C. Gatsonis, and E. Hendrick, "Diagnostic performance of digital versus film mammography for breat-cancer screening," *N Engl J Med* vol. 353, p. 1773, 2005.

[7] *U. S. Preventive Services Task Force. Screenging for breast cancer. Accessed February 8, 2007 at: www.ahrq.gov/clinic/uspstf/uspsbrca.htm.*

[8] D. A. Berry, K. A. Cronin, S. K. Plevritis, D. G.Fryback, L. Clarke, M. Zelen, J. S. Mandelblatt, A. Y. Yakovlev, J. D. F. Habbema, and E.J.Feuer, "Effect of screening and adjuvant therapy on mortality from breast cancer," *N Engl J Med*, vol. 353, p. 1784, 2005.

[9] T. M. Kolb, J. Lichy, and J. H. Newhouse, "Comparison of the performance of screening mammography, physical examination and breast US and evaluation of factors that influence them: an analysis of 27,825 patient evaluations," *Radiology*, vol. 225, p. 165, 2002.

[10] P. A. Carney, D. L. Migloretti, and B. C. Yankaskas, "Individual and combined effects of age, breast density, and hormone replacement therapy use on the accuracy of screening mammography," *Ann Intern Med*, vol. 138, p. 168, 2003.

[11] D. G. Grant, "Tomosynthesis: a three-dimensional radiographic imaging technique," *IEEE Trans Biomed Eng*, vol. 19, p. 20, 1972.

[12] X. Gong, S. J. Glick, and B. Liu, "A computer simulation study comparing lesion detection accuracy with digital mammography, breast tomosynthesis, and cone-beam CT breast imaging," *Med Phys*, vol. 33, p. 1041, 2006.

[13] D. Gur, G. S. Abrams, D. M. Chough, G. M. A, and A. I. Bandos, "Digital Breast Tomosynthesis: Observer Performance Study," *American Journal Of Roentgenlolgy*, vol. 193, p. 586, 2009.

[14] J. M. Lewin, P. K. Isaacs, V. Vance, and F. J. Larke, "Dual-Energy Contrast-enhanced Digital Subtraction Mammography: Feasibility," *Radiology*, vol. 229, p. 261, 2003.

[15] E. Y. Sidky, X. Pan, I. S. Reiser, and R. M. Nishikawa, "Enhanced imaging of microcalcifications in digital Breast tomosynthesis through improved image-reconstruction algorithms," *Med. Phys.*, vol. 33, pp. 4920-4932, 2009.

[16] M. Das, H. C. Gifford, J. M. O'Connor, and S. J. Glick, "Penalized Maximum Likelihood Reconstruction for Improved Microcalcification Detection in Breast Tomosynthesis," *IEEE Trans. Med. Imaging.*, vol. 30, pp. 904-914, 2011.

[17] J. Hsieh, *Computed Tomography Principles, Design, Artifacts, and Recent Advances*: SPIE PRESS, 2002.

[18] D. McMorrow and J. Als-Nielsen, *Elements of Modern X-ray Physics*: John Wiley & Sons Ltd, 2011.

[19] P. P. Denny and B. Heaton, *Physics for Diagnostic Radiology*: CRC press, 1999.

[20] J. M. Boone, "X-ray production, interaction, and detection in diagnostic imaging. ," *In: J. Beutel, H.L Kundel, R.L. Van Metter, eds. Handbook of Medical Imaging: volume 1. Physics and Psychophysics, Bellingham, WA: SPIE Press,* 2000.
[21] J. Bushburg, A. Seibert, E. Leidholdt, and J. Boone, *The essential physics of medical imaging*: Lippincott Williams & Wikins, 2002.
[22] D. E. Grider, A. Wright, and P. K. Ausburn, "Electron beam melting in microfocus X-ray tubes," *J. Phys. D: Appl. Phys,* vol. 19, pp. 2281-2292, 1986.
[23] D. J. David and E. J. Hall, "Computed tomography-An increasing source of radiatoin exposure," *N Engl J Med,* 2007.
[24] J. G. Stears, J. P. Felmlee, and J. E. Gray, "Half value layer increase owing to Tungsten buildup in the X-ray tube: fact or fiction," *Radiology,* vol. 160, pp. 837-838, 1986.
[25] H. H. Barrett and W. Swindell, *The Theory of Image Formation, Detection, and Processing* vol. volume 1: Academic Press, 1981.
[26] NEMA, "Measurement of dimensions and properties of focal spots of diagnostic X-ray tubes," *Document XR5-92* vol. Rosslyn, VA: National electrical manufacturers association, 1992.
[27] J. D. Jackson, *Classical Electrodynamics* Third edition ed.: Wiley, 1998.
[28] J. A. Seibert, "X-ray imaging physics for nuclear medicine technologists. Part 1: Basic principles of X-ray production," *J.Nucl. Med Technol,* vol. 32, pp. 139-147, 2004.
[29] R. N. Cahn, B. Cederstrom, M.Danielsson, A. Hall, M. Lundqvist, and D. Nygren, "Detective quantum efficiency dependence on X-ray energy weighting in mammography," *Med Phys,* vol. 26, p. 2680, 1999.
[30] D. R. Dance, A. K. Thilander, M. Sandborg, C. L. Skinner, I. A. Castellano, and G. A. Carlsson, "Influence of anode/filter material and tube potential on contrast, signal-to-noise ratio and average absorbed dose in mammography: a Monte Carlo study.," *British Journal of Radiology,* vol. 73, 2000.
[31] E. L. Gingold, X. Wu, and G. T. Barnes, "Contrast and dose with Mo-Mo, Mo-Rh, and Rh-Rh target-filter combinations in mammography," *Radiology,* vol. 195, 1995.
[32] R. J. Jennings, R. J. Eastgate, M. P. Siedband, and D. L. Ergun, "Optimal X-ray spectra for screen-film mammography," *Med Phys,* vol. 8, p. 629, 1980.
[33] J. A. Seibert, "X-ray imaging physics for nuclear medicine technologists. Part 2: X-ray interactions and image formation," *J. Nucl Med Technol,* vol. 33, pp. 3-18, 2005.
[34] J. M. Boone, *"X-ray production, interaction, and detection in diagnostic imaging" in Handbook of Medical Imaging* vol. 1. SPIE The International Society for Optical Engineering, 2000.
[35] J. M. .Boone, K. K. Lindfors, I. V. N. Copper, and J. A. Seibert, "Scatter/primary in mammography: comprehensive result," *Med Phys,* vol. 27, p. 2408, 2000.
[36] G. T. Barnes and I. A. Berzovich, "The intensity of scattered radiation in mammography," *Radiology,* pp. 126-243, 1978.
[37] J. A. Rowlands, "The physics of computed radiography," *Phys Med Biol,* vol. 47, pp. 123-166, 2002.
[38] D. B. Kopans, *Breast Imaging*: Lippioncott-Raven, 1998.
[39] G. Cardenosa, *Breast Imaging*: Lippincoot Williams&Wilkins, 2004.
[40] E.Shaw and D. Paredes, "Atlas of film-screen mammography," *Urban and Schwarzenberg, Baltimore, MD,* 1989.

[41] A. F. Morera, M. P. Esteve, J. M. T. Soteras, and A. T. Cros, "Breast Tumors: Composition of Microcalcifications," *Radiology,* vol. 169, p. 325, 1988.
[42] A. L. Filho, J. M. Lopes, and F.C.Schmitt, "Angiogenesis and Breast Cancer," *Journal of Oncology,* vol. 2010, p. 7, 2010.
[43] R. D. Rosenberg, B. C. Yankaskas, and L. A. Abraham, "Performance benchmarks for screening mammography," *Radiology,* vol. 241, pp. 55-66, 2006.
[44] M. J. Yaffe, *"Digital Mammography", In: J. Beutel, H.L. Kundel, and R.L. V. Metter, Eds, Handbook of Medical Imaging: volume 1. Physics and Psychophysics, Bellingham, WA:SPIE Press*, 2000.
[45] A. Smith, "Fundamentals of Digtial Mammography: Physics, Technology and Practical Considerations," *Hoogic, Inc.,* 2005.
[46] C. J. Kotre, "The effect of Background structure on the detection of low contrast objects in mammography," *British Journal of Radiology,* vol. 71, pp. 1162-1167, 1998.
[47] E. A. Rafferty, "Digital mammography: novel applicatoins," *Radiol Clin N Am,* pp. 831-843, 2007.
[48] J. A. Rowlands and J. Yorkston, *"Flat panel detectors for digital radiography", In: J.Beutel, H.L. Kundel, and R.L. V. Metter, Eds. Handbook of Medical Imaging: volume 1. Physics and Psychophsics, Bellingham, WA: SPIE Press*, 2000.
[49] J. T. Dobbins and D. J. Godfrey, "Digital X-ray Tomosynthesis: current State of Art and Clinical potential " *Phys Med Biol,* vol. 48, pp. R65-R106, 2003
[50] J. Hsieh, *Computed tomography: principles, Design, Artifacts, adn Recent Advances*: SPIE Press, 2009.
[51] F. Diekmann and U. Bick, "Breast Tomosynthesis," *Seminars in ULTRA Sound CT and MRI,* 2010.
[52] T. Wu, A. Stewart, M. Stanton, T. McCauley, W. Philips, D. B. Kopans, R. H. Moore, J. W. Eberhard, B. Opsahl-Ong, L. Niklason, and M. B. Williams, "Tomographic mammography using a limited number of low-dose cone-beam projection images," *Med. Phys.,* vol. 30, pp. 365-380, 2003.
[53] Y. Chen, J. Lo, and J. Dobbins, "Noise Power Spectrum Analysis for Several Digital Breast Tomosynthesis Reconstruction Algorithms," *In Proc. SPIE Med Imaging,* vol. 6142, pp. 91-98, 2006.
[54] B. Ren, C. Ruth, J.Stein, A. Smith, I. Shaw, and Z. Jing, "Design and performance of prototype full field breast tomosynthesis system with selenium based flat panel detector," *In Proc. SPIE Med Imaging,* vol. 5745, pp. 550-561, 2005.
[55] W. Zhao, R. Deych, and E. Dolazza, "Optimization of operational conditions for direct digital mammography detectors for digital tomosynthesis," *In Proc. SPIE Med Imaging,* vol. 5745, pp. 1272-1281, 2005.
[56] S. Glick and X. Gong, "Optimal spectra for indirect detector breast tomosynthesis " *In Proc. SPIE Med Imaging,* vol. 6142, 2006.
[57] H. Barrett and K. J. Myers, *Foundations of Image Science*: Wiley Series in Pure and Applied Optics, 2003.
[58] A. E. Burgess, F. L. Jacobson, and P. F. Judy, "Human observer detection experiments with mammograms and power-law noise," *Med Phys,* vol. 28, pp. 419-437, 2001.
[59] F. O. Bochud, F. R. Verdun, and J. F. Valley, "The importance of anatomical noise in mammography," *In Proc. SPIE Med Imaging,* vol. 3026, pp. 74-80, 1997.

[60] A. E. Burgess, F. L. Jacobson, and P. F. Judy, "Human observer detection experiments with mammograms and power-law noise," *Med Phys*, vol. 27, 2001.
[61] W. Zhao, W. G. Ji, A. Debrie, and J. A. Rowlands, "Imaging performance of amorphous selenium based flat-panel detectors for digital mammography: characterization of a small area prototype detector," *Med Phys*, vol. 30, pp. 254-263, 2003.
[62] W. Zhao and J. Rowlands, "Digital radiology using active matrix readout of amorphous selenium: theoretical analysis of detective quantum efficiency," *Med Phys*, vol. 24, pp. 1819-1833, 1997.
[63] I. A. Cunningham, *Applied "linear system theory", in J. Beutel, H.L. Kundel, and R.L. V. Metter, Eds, Handbook of edical Imaging: volume 1. Physics and Psychophysics, SPIE* 2000.
[64] I. Sechopoulos, S. Suryanarayanan, S. Vedantham, C. J. D'Orsi, and A. Karellas, "Scatter radiation in digital tomosynthesis of the breast," *Med. Phys.*, vol. 34, pp. 564-576, 2007.
[65] B. Liu, T. Wu, R. Moore, and D. Kopans, "Monte Carlo simulation of X-ray scatter based on patient model from digital breast tomosynthesis," *In Proc. SPIE Med Imaging*, vol. 6142, pp. 61421N1-61421N9, 2006.
[66] S. S. J. Feng and I. Sechopoulos, "A software-based X-ray scatter correction method for breast tomosynthesis," *Med. Phys.*, vol. 38, pp. 6643-6653, 2010.
[67] K. Nykanen and S. Siltanen, "X-ray scattering in full-field digital mammography," *Med Phys*, vol. 30, pp. 1864-1873, 2002.
[68] J. L. Ducote and S. Molloi, "Scatter Correction in Digital Mammography Based on Image Deconvolution," *Phys Med Biol*, vol. 55, pp. 1295-1309, 2009.
[69] A. Smith, "Full field breast tomosynthesis," *Radiology Management*, vol. 27, pp. 25-31, Sep-Oct 2005.
[70] S. C. Chen, A.-K. Carton, M. Albert, E. F. Conant, M. D. Schnall, and A. D. A. Maidment, "Initial clinical experience with contrast-enhanced digital breast tomosynthesis," *Acad Radiol*, vol. 14, 2007.
[71] S. Puong, F. Patoureaux, R. Iordache, X.Bouchevreau, and S. Muller, "Dual-energy contrast enhanced digital breast tomosynthesis: concept, method and evaluation on phantoms," *In Proc. SPIE Med Imaging*, vol. 6510, pp. 65100U-1-65100U-12, 2007.
[72] F. Diekmann and U. Blick, "Tomosynthesis and contrast-enhanced digital mammography: recent advances in digital mammography," *Eur Radiol*, vol. 17, p. 3086, 2007.
[73] S. Gavenonis, K. Lau, R. Karunamuni, Y. Zhang, B. Ren, C. Ruth, and A. Maidment, "Initial Experience with Dual-Energy Contrast-Enhanced Digital Breast Tomosynthesis in the Characterization of Breast Cancer," *IWDM 2012*, *LNCS* vol. **7361**, pp. 32-39, 2012.
[74] M. L. Hill, J. G. Mainprize, S. Puong, A. K. Carton, R. Iordache, S. Muller, and M. J. Yaffe, "Impact of image acquisition timing on image quality for dual-energy contrast-enhanced breast tomosynthesis," *In Proc. SPIE Med Imaging*, vol. 8313, p. 831308, 2012.
[75] C. Dromain, C. Balleyguier, S. Muller, M. C. Mathieu, F. Rochard, P. Opolon, and R. Sigal, "Evaluation of tumor angiogenesis of breast carcinoma using contrast enhanced digital mammography," *AJR* vol. 187, pp. W528-W537, 2006.
[76] A.-K. Carton, C. Ullberg, K. Lindman, R. Acciavatti, T. Francke, and A. D. A. Maidment, "Optimization of a dual-energy contrast-enhanced technique for a photon-counting digital breast tomosynthesis system: I. A theoretical model," *Med. Phys.*, vol. 37, p. 5896, 2010.
[77] R. Saunders, E. Samei, C. Badea, H. Yuan, D. Ghaghada, Y. Qi, L. W. Hedlund, and S. Mukundan, "Optimization of dual energy contrast enhanced breast tomosynthesis for

improved mammographic lesion detection and diagnosis," *In Proc. SPIE Med Imaging,* vol. 6913, pp. 0Y-1-0Y-10, 2008.
[78] E. Samei and R. S. Saunders, "Dual energy contrast enhanced breast tomosynthesis: optimization of beam quality for dose and image quality," *Phys Med Biol,* vol. 56, pp. 6359-6378, 2011.
[79] A. K. Carton, S. C. Gavenonis, J. A. Currivan, E. F. Conant, M. D. Schnall, and A. D. A. Maidment, "Dual-energy contrast-enhanced digital breast tomosynthesis a feasibility study," *The British Journal of Radiology,* vol. 83, pp. 344-350, 2010.
[80] Y. H. Hu and W. Zhao, "A 3D system model for the optimization of dual energy contrast enhanced digital breast tomosynthesis," *In Proc. SPIE Med Imaging,* vol. 7961, p. 79611C, 2011.
[81] Y. H. Hu and W. Zhao, "Experimental quantification of lesion detectability in contrast enhanced dual energy digital breast tomosynthesis," *In Proc. SPIE Med Imaging,* vol. 8313, p. 83130A, 2012.
[82] J. A. Fessler, "Iterative Methods for Image Reconstrucion," *ISBI tutorial* 2008.
[83] A. Rosenfeld and A. C. Kak, *Digital Picture Processing*: volume 1, Academic Press. New York, 1982.
[84] R. Siddon, "Fast Calculation of the Exact Radiological Path for a 3D CT Array," *Med Phys,* vol. 12, pp. 252-255, 1985.
[85] B. Chan, M. Bergstorm, M. R. Palmer, C. Sayre, and B. D. Pate, "Scatter Distributionin Transmission Measurements with Positron Emission Tomography," *J. Comp. Assisted Tomo,* vol. 10, pp. 296-301, 1986.
[86] J. A. Fessler, *Statistical Image Reconstruction Methods for Transmission Tomography*: Handbook of Medical Imaging: vol 2. Medical Images Processing and Analysis, SPIE-The INternational Society for Optical Engineering, 2000.
[87] A. C. Kak and M. Slaney, *Principles of computerized tomographic imaging*: IEEE Press, 1988.
[88] G. T. Herman, *Fundamentals of computerized tomography: Image reconstruction from projections (2nd ed.)*: Springer, 2009.
[89] T. Wu, R. H. Moore, E. A. Rafferty, and D. B. Kopans, "A comparison of reconstruction algorithms for breast tomosynthesis," *Med Phys,* vol. 31, p. 2636, 2003.
[90] T. Mertelmeier, J. Orman, W. Haerer, and M. K. Dudam, "Optimizing filtered backprojection reconstruction for a breast tomosynthesis prototype device," *Proc. SPIE,* vol. 6142, p. 61420F, 2006.
[91] J. Zhou, B. Zhao, and W. Zhao, "A computer simulation platform for the optimization of a breast tomosynthesis system," *Med Phys,* vol. 34, pp. 1098-1109, 2007.
[92] Y.-H. Hu and W. Zhao, "The effect of angular dose distribution on the detection of microcalcifications in digital breast tomosynthesis," *Med. Phys.,* vol. 38, pp. 2455-2466, 2011.
[93] J. T. Dobbins, A. O. Powell, and Y. K. Weaver, "Matrix Inversion Tomosynthesis," *RSNA 73rd Scientic Assembly,* 1987.
[94] L. Zeng, *Medical Image Reconstruction: A Conceptual Tutorial*: Springer, 2010.
[95] Y. Zhang, H. Chan, B. Sahiner, J. Wei, M. Goodsitt, L. M. Hadjiiski, J. Ge, and C. Zhou, "A Comparative Study of Limited-Angle Cone0Beam Reconstrucition Methods for Breast Tomosynthesis," *Med Phys,* vol. 33, pp. 3718-3785, 2006.

[96] A. H. Andersen and A. C. Kak, "Simultaneous Algebraic Reconstruction Techniuqe: A Superior Implementation of the ART algorithm," *Ultrasonic Imaging,* vol. 6, pp. 81-94, 1984.

[97] G. Wang and M. Jiang, "Ordered-Subset Simulatneous Algebraic Reconstruction Technique (OS-SART)," *Journal of X-ray Science and Technolog,* vol. 12, pp. 169-177, 2004.

[98] M. Jiang and G. Wang, "Convergence Studies on Iterative Algorithm for Image Reconstruction," *IEEE Transactions on Medical Imaging,* vol. 22, pp. 569-579, 2003.

[99] L. Chen, Y. Lu, Y.-H. Hu, W. Zhao, and G. Gindi, "Impact of subtraction and reconstruction strategies on dual-energy contrast enhanced breast tomosynthesis with interleaved acquisition," *Proc. of the SPIE,* vol. 8668, pp. 86685O-1, 2013.

[100] G. Wang and M. Jiang, "Ordered-subset simultaneous algebraic reconstruction techniques (OS-SART)," *J. of X-ray Science and Technology, ,* vol. 12, pp. 169-177, 2004.

[101] G. Wu, J. G. Mainprize, J. M. Boone, and M. J. Yaffe, "Evaluation of scatter effects on image quality for breast tomosynthesis," *Med. Phys.,* vol. 36, pp. 4425-4432, 2009.

[102] J. D. Bronzino, "The Biomedical Engineering Handbook," *CRC press and IEEE press,* 1995.

[103] J. P. Jones, Z. Cho, and and M. Singh, "Fundamentals of Medical Imaging," *John Wiley & Sons,* 1992.

[104] H. O. Anger, "Scintillation Camera," *Rev. Sci. Instrum,* vol. 29, pp. 27-33, 1958.

[105] H. H. Barrett, J. Yao, J.P. Rolland, and a. K. J. Myers, "Model Observers for Assessment of Image Quality," *Proc. Nat. Acad. Sci. ,* vol. 90, pp. 9758-9765, 1993.

[106] S. M. Kay, "Fundamentals of Statistical Signal Processing: Vol 1 Estimation Theory," *Prenticd Hall PTR,* 1993.

[107] P. Khurd and G. Gindi, "Decision Strategies that Maximize the Area Under the LROC curve," *Trans. Med. Imaging,* vol. 24, pp. 1626-1636, 2005.

[108] C. K. Abbey, "Assessment of Reconstructed Images," *University of Arizona, PhD thesis,* 1998.

[109] H. H. Barrett, "Objective Assessment of Image Quality Effects of Quantum Noise and Objective Variability," *J. Opt. Soc. Am. A,* vol. 7, pp. 1266-1278, 1990.

[110] H. H. Barrett, C. K. Abbey, and E. Clarkson, "Objective Assessment of Image Quality III: ROC Metrics, Ideal Observers and Likelihood-Generating Functions," *J. Opt. Soc. Am. A,* vol. 15, pp. 1520-1534, 1998.

[111] W. Wang, "Noise Analysis of Bayesian Reconstruction Algorithms in Emission Tomography," *Ph.D Thesis, Stony Brook University,* 1997.

[112] P. J. Early and a. D.B.Sodee, "Principles and Practice of Nuclear Medicine," *Mosby Year Book, Inc, 1995,* 1995.

[113] L. Zeng, G. T. Gullberg, C. Bai, P. E. Christian, F. Trisjono, E. V. R. D. Bella, J. W. A. Tanner, and H. T. Morgan, "Iterative Reconstruction of Fluorine-18 SPECT Using Geometric Point Response Correction," *The Journal of Nuclear Medicine,* vol. 39, 1998.

[114] Y. Xing, "Rapid Calculation of Image Quality for Maximum a Posteriori Reconstructions in SPECT," *Ph.D Thesis, Stony Brook University,* 2003.

[115] Y. Lu, L. Chen, and G. Gindi, "Collimator performance evaluation for In-111 SPECT using a dtection/localization task," *Phys Med Biol,* vol. 59, pp. 679-696, 2013.

[116] I. T. Hsiao, A. Rangarajan, P. Khurd, and G. Gindi, "An accelerated convergent ordered subsets algorithm for emission tomography," *Phys Med Biol,* vol. 49, pp. 2145-2156, 2003.

[117] X. He, E. C. Frey, J. M. Links, K. L. Gilland, W. P. Segars, and B. M. W. Tsui, "A Mathematical Obsever Study for the Evaluation and Optimization of Compensation Methods for Myocardical SPECT Using a Phantom Population that Realistically Models Patient Variability," *IEEE Trans. Nuc. Sci,* vol. 51(1), pp. 218-224, 2004.

[118] S. L. Faris, D. W. Wilson, H.H.Barrett, D. Dougherty, G. Gindi, and I. T. Hsiao, "Using a Digital Anatomical Phantom to Optimize an Imaging System " *SPIE-Physcis of Medical Imaging,* vol. 3659, 1999.

[119] J. P. Rolland and H. H. Barrett, "Effect of Random Background Inhomogeneity on Observer Detection Performance," *J. Opt. Soc. Am. A,* vol. 9, pp. 649-658, 1992.

[120] J. Oldan, S. Kulkarni, Y. Xing, P. Khurd, and G. Gindi, "Channelized Hotelling and Human Observer Study of Optimal Smoothing in SPECT MAP Reconstruction," *IEEE Trans. Nuc. Sci,* vol. 52, pp. 733-741, 2004.

[121] C. Abbey and H. H. Barrett, "Human- and Model Observer Performance in Ramp-spectrum Noise: Effects of Regularization and Object Variability," *J. Opt. Soc. Am. A,* vol. 18(3), pp. 473-488, 2001.

[122] H. C. Gifford, M. A. King, D. J. deVries, and E. J. Soares, "Channelized Hotelling and Human Observer Correlation for Lesion Detection in Hepatic SPECT Imaging " *Journal of Nuclear Medicine,* pp. 514-521, 2000.

[123] M. V. Narayanan, H. C. Gifford, M. A. King, P. H. Pretorius, T. H. Farncombe, P. Bruyant, and M. N. Wernick, "Optimization of Iterative Reconstructions of Tc Cardiac SPECT Studies Using Numerical Observer," *IEEE Trans . Nuc. Sci,* vol. 49(5), pp. 2355-2360, 2002.

[124] E. J. Soares, "Attenuation, Noise and Image Quality in Single Photon Emission Computed Tomography " *Phd Thesis, University of Arizona* 1994.

[125] H. Gifford, M. King, P. Pretorius, and R. Wells, "A comparisons of Human and Model Observers in Multislice LROC Studies," *IEEE Trans. Med. Imaging.,* vol. 24, pp. 160-169, 2005.

[126] L. Zhou, P. Khurd, S. Kulkarni, A. Rangarajan, and G. Gindi, "Aperture optimization in emission imaging using ideal observers for joint detection and localization," *Phys Med Biol,* vol. 53, pp. 2019-2034, 2008.

[127] L. Zhou and G. Gindi, "Collimator Optimization in SPECT Based on a Joint Detection and Localization task," *Physics in Medicine and Biology,* vol. 54, p. 4423, 2009.

[128] D. Dougherty, "Autoradiographic Phantoms for SPECT Reconstruction," *Ph.D Thesis, Stony Brook University,* 1999.

[129] C. Metz, "Basic Principles of ROC Analysis," *Seminars in Nuclear Medicine,* vol. 4, pp. 283-298, 1978.

[130] D. Dorfman and E. Alf, "Maximum-Likelihood Estimation of Parameters of Signal-Detection Theory and Determination of Confidence Intervals-Rating Method Data," *Journal of Mathematical Psychology,* vol. 6, pp. 487-496, 1969.

[131] B. Liu, L. Zhou, S. Kulkarni, and G. Gindi, "The Efficiency of the Human Observer for Lesion Detection and Localization in Emission Tomography," *Phys Med Biol,* vol. 54, pp. 2651-2666, 2009.

[132] L. Zhou, J. Oldan, P. Fisher, and G. Gindi, "Low Contrast Lesion Detection in Tomosynthesis Breast Imaging Using a Realistic Breast Phantom," *Proc. SPIE Med. Imag.*, vol. 6142, pp. 61425A-1-61425A-12, 2006.